Microfluidic System for Biochemical Applications

by

Yufeng Zhao

A thesis submitted in partial fulfillment of the requirements for the degree of

Doctor of Philosophy

Department of Chemistry
University of Alberta

Abstract

The last decades witnessed the rapid growth and advancement of research on microfluidic systems for chemical and biological analysis. There remain many important biochemical challenges that need to be solved with novel technologies. This thesis looks at how to apply several microfluidic techniques to several different biochemical problems. For example, one of the key biological problems in directed evolution of biomolecules is that large numbers of cells need to be processed with many repeated steps. A microfluidic cell sorter offers a simple and automated system for cell-based directed evolution. A key challenge in clinical diagnosis especially for point of care analysis is the need to clean up and prepare samples so the matrix does not cause problems in the analysis. Creating a generic clean up system requires we be able to put sample into a device and obtain a cleaned up sample solution as an output. Centrifugal microfluidic system provide this possibility. As a vehicle for development of microfluidic applications, we selected directed evolution of fluorescent proteins (FP) as a target for improvement by a microfluidic cell sorter, and metabolite assays in serum for a test of centrifugal microfluidic sample preparation devices for a "dirty sample in-clean sample out" system.

To explore microfluidic fluorescent-activated cell sorting (μFACS) system, we first present characterization of such a system with a single point detector, which was developed for screening FPs on the basis of the brightness. The sorting performance is studied for optimal collection efficiency. The expression level of single cells and its effect on directed evolution by the μFACS are evaluated. Since the μFACS was designed to only screen for the brightness of FPs, other critical parameters of FPs can hardly be improved in the process of directed evolution. We thus introduce a second-generation microfluidic cell sorter with two-point detection system to improve the

performance of directed evolution. The new system employs two detectors at two different places to examine the analyte-induced fluorescence change of a FP-based Ca^{2+} sensor. Both the brightness and fluorescence change are screened in the new system, which demonstrates superior performance in directed evolution compared to the system with single-point detector. Two rounds of directed evolution lead to a variant with improved brightness and g Ca^{2+}-dependent fluorescence change. The Ca^{2+} sensor is further engineered by rational design and a series of sensors with various Ca^{2+} affinities are developed for intracellular Ca^{2+} imaging.

In the second segment of the thesis, we develop a centrifugal microfluidic device to clean small volume (5 μL) human serum sample for metabolomics analysis. Sample filtration, drying and mixing are realized on a centrifugal disc. Protein precipitation by methanol and solid phase extraction by C18 beads and silica nanoparticles are utilized to remove proteins and lipids from the sample. The prepared samples are transferred to a solid-matrix laser desorption ionization (SMALDI)-chip which segregates salts from electrolyte background by crystallization during sample drying and then serves as substrate for mass spectrometry analysis. The on-chip assays are optimized to obtain high signal to noise ratio of analyte signals with low background peaks. The reproducibility of the on-chip preparation is evaluated and potential influential factors are discussed. Three ionic metabolites, glutamic acid, aspartic acid and citric acid, are quantitatively analyzed by standard addition method and the results are consistent with samples prepared by ultrafiltration method.

Preface

A version of Chapter 2 has been published as part of the supplementary information for the paper Y. Zhao, A. S.Abdelfattah, **Y. Zhao**, A. Ruangkittisakul, A., K. Ballanyi, R. E. Campbell, & D. J. Harrison, "Microfluidic cell sorter-aided directed evolution of a protein-based calcium ion indicator with an inverted fluorescent response", *Integrative Biology*, 2014, *6*(7), 714-725. I was a co-author in the publication and performed characterization of the microfluidic cell sorter to evaluate its sorting performance and the effect of cellular expression level on directed evolution. Yongxin Zhao designed the microfluidic cell sorter and performed directed evolution and most characterizations of Y-GECO sensors. A. S. Abdelfattah and A. Ruangkittisakul conducted brain slices experiments, which were supervised by K. Ballanyi. R. E. Campbell and D. J. Harrison directed the whole project and edited the manuscript draft which Yongxin prepared.

Part of Chapter 3 has been published as **Y. Zhao**, R.E. Campbell and D.J. Harrison. "Microfluidic cell sorter with two point detection system for directed evolution of fluorescent protein-based calcium sensor", *Proceeding of MicroTAS*, 2015, Gyeongju, South Korea, 410-412. A version of Chapter 3 will be submitted as **Y. Zhao**, W. Zhang, Robert E. Campbell and D. J. Harrison, "Microfluidic cell sorter for multiparameter screening in directed evolution". I was responsible for the experiment designs and data collection of the microfluidic system set-up, directed evolution, *in vitro* characterization of Y-GECO sensors. W. Zhang helped to conduct *ex vivo* characterization in Hela cells and dissociated neurons. R. E. Campbell and D. J. Harrison directed the whole project and edited the manuscript draft which was prepared by Yufeng.

The work described in Chapter 4 is in collaboration with Dr. Allan Wong at Janelia Research Campus. A version of Chapter 4 will be submitted as **Y. Zhao**, D. Bushey, Y. Zhao, D. J. Harrison, A. M. Wong, and R. E. Campbell, "Inverse-response Ca2+ indicators for optogenetic visualization of inhibitory synapse activity". I was responsible for the experiment designs and data collection of ration designs and *in vitro* characterization of Y-GECO sensors as well as Hela cell experiments. D. Bushey and A. Wong designed and performed fruit fly experiments. D. J. Harrison, A. Wong and R. E. Campbell supervised aspects of the project and edited the manuscript draft.

Part of Chapter 5 has been published as **Y. Zhao**, Y. Zhou and D. J. Harrison. "Centrifugal microfluidic sample preparation for metabolites analysis in human serum by mass spectrometry." *Proceeding of MicroTAS*, 2016, Dublin, Ireland, 701-702. I was responsible for the experiment designs and data collection. Ya Zhou developed a SMALDI-chip for metabolite detection which was used in the experiment. D. J. Harrison directed the whole project and edited the manuscript.

Acknowledgement

Foremost, I would like to express my gratitude to my PhD supervisor Professor Jed Harrison for his great support and guidance to my PhD study. Over the past five years, I was deeply impressed and influenced by his sharp mind, critical thinking and broad knowledge. He consistently inspires me to think in my research, encourages me when I feel depressed and patiently gives suggestions and explanations whenever I need help. I also appreciate the opportunities which he provided to attend international conferences where I learned a lot. Everything he teaches me with or without words is valuable for my future career and life.

I would also like to thank Professor Robert Campbell who offered unreserved support to me like to anyone of his students when I worked in his lab. I benefited a lot from his inspiration, encouragement and insightful guidance as well as his passion for scientific research, attitude towards career, trust and consideration for students.

I would like to express my appreciation to my supervisory committee Professors Steven Bergens and Robert Campbell for their guidance and suggestions to my graduate study in the annual meetings. I am grateful to Professors Mark McDermott and Jie Chen for their attendance and helpful comments in my candidacy exam. I thank my thesis committee Professors Albert Folch, Steven Bergens, Robert Campbell and Mark McDermott.

I thank the former and current members in Harrison's group, especially those who helped and trained me when I first joined the group and started my research project: Yongxin Zhao, Wenmin Ye, Huiying Sheng, Chen Peng, Mohammad Azim, Narges Shabaani, Le Zhang, Ya Zhou. I also

thank all the group members for their discussion about research and the enjoyable time working together. Many thanks to the members from Campbell's group: Wei Zhang, Jiahui Wu, Yi Shen, Yan Li, Mattew Wiens, Landon Zarowny, Tiffany Lai, Yong Qian and Jhon Ralph Enterina for their technical assistance and suggestions on protein engineering and molecular biology.

I am grateful to the staffs in both Department of Chemistry and other department, especially Gareth Lambkin, Jeff Johnston, Tyler Peterson, Anita Weiler, Karen McKinley and Lin Ferguson for their kind help and technical support to my research and study. I thank Department of Chemistry for offering teaching and research assistantships and Alberta Innovates Technology Future for providing PhD scholarship for my study.

Finally, I must express my profound gratitude to my parents, wife, grandparents and all the other family members for their great love, accompaniment, support, encouragement and understanding throughout my life. Thanks to all my friends in Edmonton and all other places for making my life enjoyable.

Table of Contents

List of Tables

List of Figures

List of Abbreviations

BiFC	Bimolecular fluorescence complementation
CaM	Calmodulin
CCD	Charge-coupled device
CI	Chemical ionization
DIOS	Desorption ionization mass spectrometry on porous silicon
DPI	Dots per inch
EI	Electron ionization
ELISA	Enzyme-linked immunosorbent assay
ESI	Electrospray ionization
EGTA	Ethylene glycol-bis(β-aminoethyl ether)-N,N,N',N'-tetraacetic acid
FACS	Fluorescence activated cell sorter
FP	Fluorescent protein
FPGA	Field-programmable gate array
FRET	Förster resonance energy transfer
GFP	Green fluorescent protein
GLAD	Glancing angle deposition
IVTT	*In vitro* transcription and translation
LDI	Laser desorption ionization
MALDI	Matrix assisted laser desorption ionization
MS	Mass spectrometry
NIMS	Nanostructure-initiator mass spectrometry

NMR	Nuclear magnetic resonance
PCR	Polymerase chain reaction
PCL	Print, cut and laminate
PDMS	Polydimethylsiloxane
PMMA	Poly(methyl methacrylate)
PMT	Photomultiplier tube
PSA	Pressure sensitive adhesive
RFP	Red fluorescent protein
RSD	Relative standard deviation
RPM	Revolutions per minute
R-GECO1	Red genetically encoded Ca^{2+} indicators for optical imaging
SELEX	Systematic evolution of ligands by exponential enrichment
SMALDI	Solid-matrix laser desorption ionization
SNP	Silica nanoparticles
SNR	Signal-to-noise ratio
TBS	Tris-buffered saline
TOF	Time of flight
YC	Yellow cameleon
Y-GECO	Yellow genetically encoded Ca^{2+} indicators for optical imaging
μFACS	Microfluidic fluorescent-activated cell sorting

Chapter 1. Introduction

The last decades witnessed the rapid growth and advancement of research on microfluidic systems for chemical and biological analysis. There remain many important biochemical challenges that need to be solved with novel technologies. This thesis looks at how to apply several microfluidic techniques to several different biochemical problems. For example, one of the key biological problems in directed evolution of biomolecules is that large numbers of cells need to be processed with many repeated steps. A microfluidic cell sorter offers a simple and automated system for cell-based directed evolution. A key challenge in clinical diagnosis especially for point of care analysis is the need to clean up and prepare samples so the matrix does not cause problems in the analysis. Creating a generic clean up system requires we be able to put sample into a device and obtain a cleaned up sample solution as an output. Centrifugal microfluidic system provide this possibility. As a vehicle for development of microfluidic applications, we selected directed evolution of fluorescent proteins as a target for improvement by a microfluidic cell sorter, and metabolite assays in serum for a test of centrifugal microfluidic sample preparation devices for a "dirty sample in-clean sample out" system. In this chapter, we presents a brief introduction and background review of the two general topics, microfluidic cell sorters for directed evolution of fluorescent proteins and centrifugal microfluidic devices for sample preparation.

1.1.Microfluidic cell sorting

Herzenberg and coworkers invented the first fluorescence activated cell sorter (FACS) in 1969[1]. Commercial FACS was developed in the early 1970s by Becton Dickinson Immunocytometry

Systems. Over the decades, FACS has been improved to analyze cells with increasing throughput[2,3], multiple color detection[4,5] and additional information from light scattering[6,7]. One application of the FACS that is receiving increasing attention is single cell analysis. Measuring features from large populations of single cells in a biological system provides information for deeper understanding of the cellular heterogeneity and complexity of the biological systems. The advancement of microfluidic systems provides advantages in low cost, small sample consumption and rapid analysis. Compared to commercially available FACS, which are typically used for large scale single cell analysis, microfluidic platforms feature no cross-contamination, lower cost on multi-use disposable sample analysis devices and higher versatility on sample processing and detection techniques. For example, microfluidic cell sorters allow sequential reagent loading[8–10], cell culture[11–14] and lysis[8,10,15], and biochemical reactions such PCR in the microchannels[16,17].

In an effort to explore low cost cell sorting system, Quake and his colleagues introduced a microfabricated FACS (μFACS) for sorting cells and beads by electro-osmotic flow with a throughput of 20 cells/s[18]. Other groups also reported a similar cell sorter based on electro-kinetic sorting[19,20]. In those studies, the throughput was restricted by the highest voltage that could be applied while maintaining cell viability. The Quake group then reported a pressure-driven μFACS with a 2-fold improvement of the throughput, which was still considerably lower than commercial FACS[21]. In 2003, Wolff and coworkers demonstrated a μFACS device with a valve that could give hydrodynamic switching for cell sorting[22]. Their system achieved a throughput of 12000 cells/s and integrated a cell culturing step after cell sorting. However, the relatively long time of sorting action and large volume of displaced flow led to co-sorting of undesired cells and limited the purity of the rare cells. Over the years, extensive effort has been made in developing high performance microfluidic cell sorters based on electro-kinetic[23–28] and hydrodynamic sorting[29–32]. Some other

sorting mechanisms were also demonstrated with satisfactory performance. Marchand's group utilized a noncontact sorter based on optical force switching by a near-infrared laser with reduced impurities from undesired cells[33]. Di Carlo's group devised cell sorters based on a pulsed laser that could generate bubbles for flow switching with a throughput up to 20,000 mammalian cells/s[34]. Cell sorting based on acoustic force has also been explored because of the precise spatial control by acoustic force and no effect on cell viability[35–38].

Despite improvement in throughput, purity and cell viability, on-chip sample processing and biochemical reactions were not readily realized with one-phase flow. In 2009, Griffiths' group demonstrated a fluorescence-activated droplet sorter based on a droplet microfluidic technique[12]. Cells were separated in small compartments and each droplet was an independent reactor for biochemical reaction. The throughput of this system was up to 2000 cells/s. In recent years many droplet based cell sorting systems have been established, with various applications such as DNA analysis[39–41], RNA barcoding[8], directed evolution of enzymes[10,15,42–44] and drug screening[45,46].

1.1.1 Types of microfluidic cell sorting platform

1.1.1.1 One-phase continuous flow based cell sorting

A one-phase continuous flow system is the most commonly used in microfluidic cell sorters. Such devices are often fabricated by conventional photolithography combined with a PDMS molding method. In this system, aqueous solutions serve as both the carrier fluid for cell delivery and the buffer reagents needed to keep cells alive. Sheath flow is often employed for cell focusing in the microchannels. Since the Reynolds number is very small and the flow is laminar, mass transfer in the microchannels is mainly achieved by diffusion. A sorter usually has two or more outlet channels

to separate desired and undesired cells, by using a flow switch to deflect the cells to the designated channel. One-phase continuous flow is relatively simple, requiring no additional step for liquid manipulation compared to two phase droplet based systems. However, as cells are randomly distributed in the suspension, the cell to cell distance cannot be controlled. Further processing steps such as single cell culturing within the microchannels are rarely realized with the single phase approach, since the purity of isolated cells is of mixed quality.

1.1.1.2 Two-phase droplet based cell sorting

Two-phase droplet based systems have been introduced for high throughput cell analysis. Aqueous droplets are highly monodispersed in an inert oil phase which serves as a carrier. During the formation of a droplet, cells are delivered and trapped inside them so that each droplet can function as a separate microreactor (Figure 1.1a). Reagents can be added to a droplet by merging two droplets together so that the cells are treated for culture (Figure 1.1b), lysis or signal activation. By restricting cells in such small volume droplets, which ranges from picoliter to nanoliter, the reaction and mass transfer in each compartment are rapid compared to those in bulk solution. Also, the concentration of the molecules released from the cells either by excretion or lysis are much higher in those micro droplets than bulk solution, which can improve the sensitivity and limit of detection in the analysis. As for the detection, each droplet is interrogated and a huge number (up to 10^8) of droplets can be screened in a couple of hours[47]. Droplets moving at a frequency > 1000 drops/sec can be actively sorted to a separate channel by dielectrophoresis, for example, as shown in Figure 1.1c.

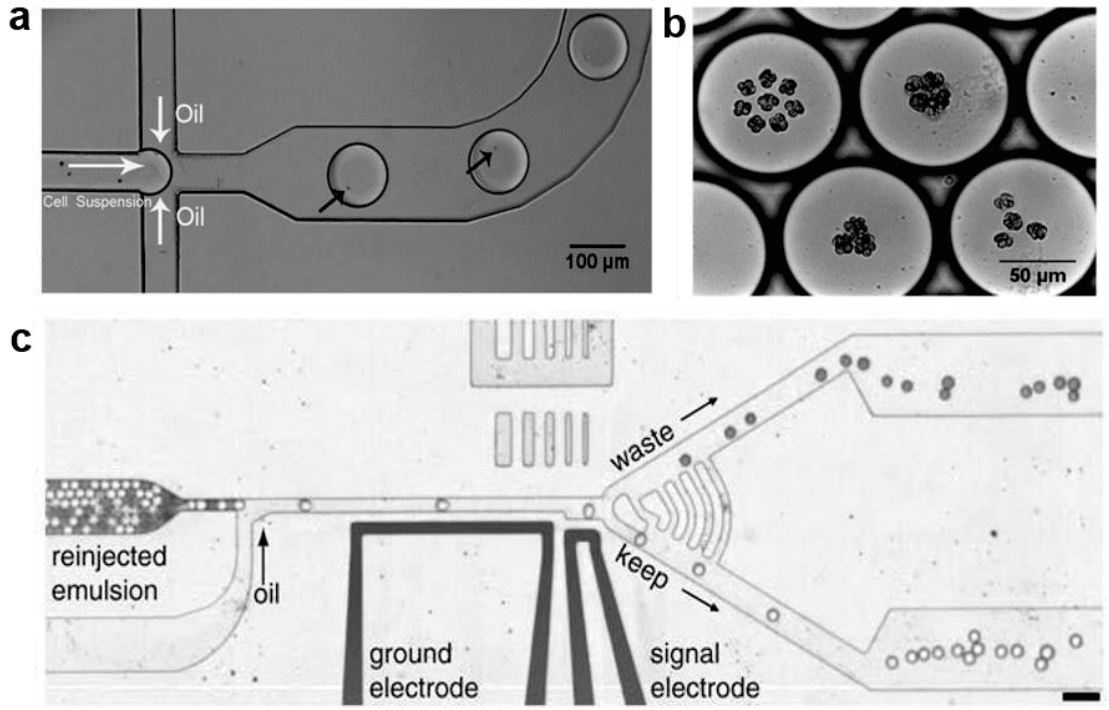

Figure 1.1 (a) Formation of micro droplets inside a microfluidic device. (b) Cell culture in microdroplets. (c) Active sorting of micro droplets by dielectrophoresis. Reprinted with permission from (a)(b) Pan *et al*[14]. © The Royal Society of Chemistry 2011. (c) Agresti *et al*[47]. © National Academy of Sciences 2009.

1.1.1.3 Microarrays

Like a droplet based cell sorting platform, microwell arrays provide a similarly independent microreactor to study cells. Such devices can be fabricated by photolithography[48–51], and some commercial microarray products are available for research[52]. Instead of using flow, the liquid in a microwell is static and a micropipette can be used to deliver assay reagents. Each cell can be treated individually and cultured in a single microarray. To recover the cells from microwells, magnetic beads are often added to disrupt the surface tension of the liquid and the recovery process can be

precisely controlled without affecting adjacent wells. Although the throughput is not as high as for droplet based methods, microarrays can be compatible with imaging using commercial fluorescence microscopy and superior for long term monitoring of the cells.

1.1.2 Microfluidic platform for directed evolution

Directed evolution is an effective approach for researchers to develop functional biomolecules like nucleic acids and proteins by mimicking natural evolution to select mutants of biomolecules with desired characteristics. As many rounds of selection and large size libraries for screening are necessary to discover a mutant with superior properties, extensive efforts and extended time are always required. Therefore, high throughput and automated screening by microfluidic systems can significantly speed up the selection process, enlarge the library size for screening and reduce the workload.

To screen for high-affinity binding of biomolecules, it is not necessary to examine each member from the library. Instead, ligands for binding are fixed on a stationary phase like the surface of beads and exposed to biomolecules in a flow[53]. Biomolecules with low binding affinity will be carried away from the ligands, whereas high affinity members stay bound and thus immobile. Phage display has been used to achieve high throughput up to a library containing 10^{12} protein variants[54–56]. The method to screen nucleic acid aptamers with high binding affinity *in vitro* is called systematic evolution of ligands by exponential enrichment (SELEX) and more than 10^{14} molecular variants can be examined[57–59].

Droplet based microfluidic platforms are widely used for directed evolution when some manipulations are not easily realized or well controlled in one-phase flow. For example, by

generating droplets as small and highly-uniform reactors, researchers screened enzymes to develop variants demonstrating better catalytic performance with reaction volume and time being well-controlled[10,15,44,60–62]. Enzymes expressed by cells for screening could be either displayed on the surface of cells or released from cells by lysis in droplets. Also, directed evolution of enzymes was realized using cell-free droplet based platforms, in which single genes were segregated in droplets for PCR amplification and each droplet was then fused with another droplet containing *in vitro* transcription and translation (IVTT) systems for enzyme expressions[44,63,64]. Advantages of this cell-free platform include the capability to evolve proteins toxic to host cells, a simple expression system, and a reduced workload by removing cell transformation and culture steps.

Cell culturing can be achieved in micro droplets and integrated for on-chip screening, making relatively long-term monitoring possible[13]. Moreover, measuring micro colonies formed in droplets leads to overall information from a subpopulation and diminishes the impact of cell heterogeneity, which may be unfavorable in directed evolution. With cell growth, the abundance of targets increases and signals for detection can be amplified. In most studies performed with a droplet platform, fluorescence microscopy is utilized for detection due to many advantages, such as high sensitivity, compatibility with the platform and multicolor detection. Absorption microscopy detection was also successfully realized for directed evolution platform[62]. However, droplet-based microfluidic platform require a complex design for droplet generation and sample mixing. Additional processing steps to separate the two phases, recover the sorted cells and extract DNA, which is essential to directed evolution, have not been integrated on chip. Although many enzymes and antibodies have been evolved in droplet-based platforms, directed evolution of other functional proteins such as fluorescent proteins has not been reported.

A one-phase continuous flow cell sorter is often selected with fluorescence microscopy for detection, an example of which is screening fluorescent protein (FP) based sensors towards improved photophysical and biochemical properties. Cells expressing libraries are prepared off chip with no effort required in exploring and optimizing on-chip cell transfection, culturing and expression procedures. From 2011 to 2016, the Palmer group and the Harrison/Campbell group developed a series of microfluidic flow cytometer and cell sorting systems to measure and enhance multiple properties of FP[65–71]. Chapter 2 and 3 of this thesis present characterizations of the previous system developed by our group and introduce a new system with two-factor screening to accelerate directed evolution strategy for FP. In section 1.2, we will first provide a background review of FP and then discuss the development of microfluidic flow cytometer and cell sorters from both groups for measurement and directed evolution of FP.

1.2 Fluorescent proteins

As a powerful technology for research on life science, fluorescence microscopy enables researchers to visualize the biological reaction and processes inside cells with the presence of fluorescent molecules. The discovery and development of fluorescent proteins (FP) has revolutionized such research by using fluorescence microscopy to monitor the biomolecule activity and interactions, physiological changes, and small molecule dynamics inside living cells, tissue and organisms. As a class of genetically encoded fluorescent probes, FP can be easily delivered into cells by introducing the gene which encodes the FP and inducing the expression of the FP, which is considered to be a relatively non-invasive process. The expressed FP can also be targeted to subcellular structures to study specific regions. Furthermore, with the technique of protein

engineering, FP have been engineered into indicators for some specific molecules or ions by fusing sensing domains to study the chemicals of interest.

1.2.1 The crystal structure and fluorophore of FP

A typical FP contains a fluorophore surrounded and protected by a protein β-barrel which consists of eleven β-strands[72], as illustrated in Figure 1.2a. The fluorophore is autonomously formed from a tripeptide sequence and located at the center of the β-barrel and connects to an α-helix which runs through the axis of the barrel. With proper folding, and some post-translational modifications of the fluorophore centre the FP can emit fluorescence when excited with the right wavelengths of light[73].

Green fluorescent protein (GFP) from jellyfish was the first discovered FP[74]and the formation of its fluorophore has been reasonably understood after extensive study. Within the current proposed mechanism, it is believed when the tripeptide sequence Ser65-Tyr66-Gly67 is in a folded β-barrel, it can undergo a post-translational modification including three steps: cyclization, dehydration and oxidation[75–80]. Besides GFP, many other types of FP with different hues have been discovered and engineered[81–86]. Compared to GFP, the formation of the fluorophores of other FPs is less understood.

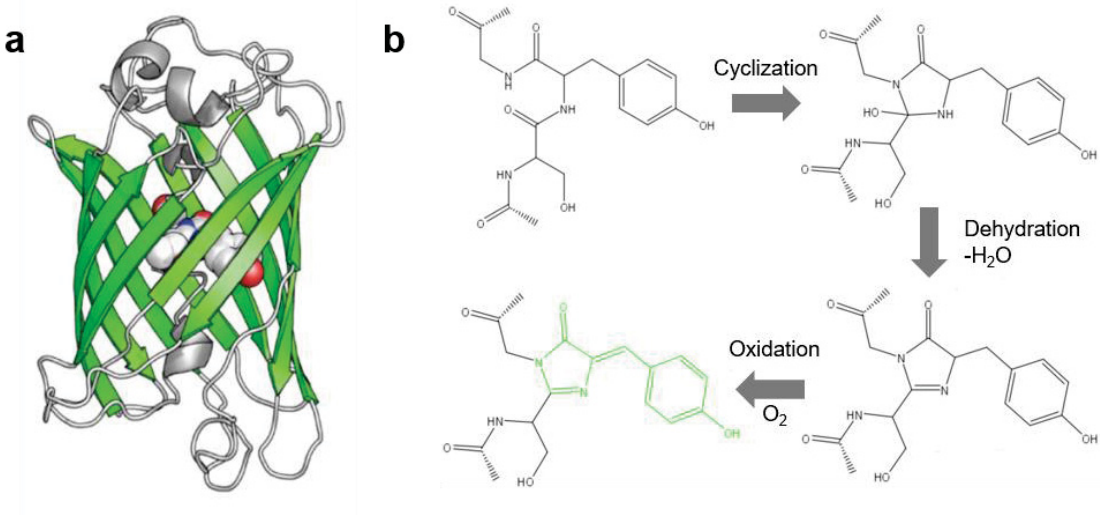

Figure 1.2 (a) Crystal structure of GFP. (Protein Data Bank ID: 1EMA[65]) (b) Proposed reaction scheme of GFP fluorophore formation.

1.2.2 FP-based sensors

FPs function as a versatile tool for bioanalytical applications and have been engineered into a variety of biosensors for cellular study, by fusing specific molecular-recognition domains into the original FP. Generally, FP-based sensors can be categorized into three classes according to their design and sensing mechanisms (Figure 1.3): single FP-based sensors, Förster resonance energy transfer (FRET) based sensors, and bimolecular fluorescence complementation (BiFC) based sensors.

Single FP-based sensors (Figure 1.3a) only possess one FP for reporting. Some single FP-based sensors utilize the sensing nature of the FP itself instead of introducing a new sensing domain. For example, some ions such as protons[87], metal ions[88] and chloride ions[89] can disrupt the environment of the fluorophore, resulting in a fluorescence change. Other single FP-based sensors are engineered by introducing a new sensing domain whose conformation will change upon binding

with the analyte, causing changes of the fluorophore environment and the fluorescence. A successful prototype of such biosensors is a genetically encoded Ca^{2+} sensor developed by the Nakai[90]and Nagai[91] groups. In their design, a Ca^{2+} sensing domain, called calmodulin (CaM), and a M13 domain are fused to the N- terminal and C- terminal of a circularly permutated FP, respectively. The binding of Ca^{2+} to CaM can significantly change the confirmation of the CaM and M13, and subsequently the environment of the fluorophore[92,93]. Single FP-based sensors demonstrate larger signal change than FRET based sensors upon binding of target molecules.

FRET based sensors (Figure 1.3b) are designed based on FRET, a phenomenon of energy transfer without radiation between two fluorophores. The energy transfer happens from the excited state, in the form of non-radiative dipole-dipole coupling when the emission spectra of the donor overlaps with the absorption spectra of the acceptor. The efficiency of FRET is very sensitive to the distance between two fluorophores because it is inversely proportional to the sixth power of the distance. Such sensors utilize a pair of FPs as donor and acceptor, which are fused with a molecular recognition domain. The conformational change of the recognition domain will change the distance between the donor and acceptor and the FRET efficiency. Since the ratio of the fluorescence signals from the donor and acceptor are used for measuring, FRET based sensors offer the advantage that the ratio signal is independent of the expression level of the sensors in individual cells.

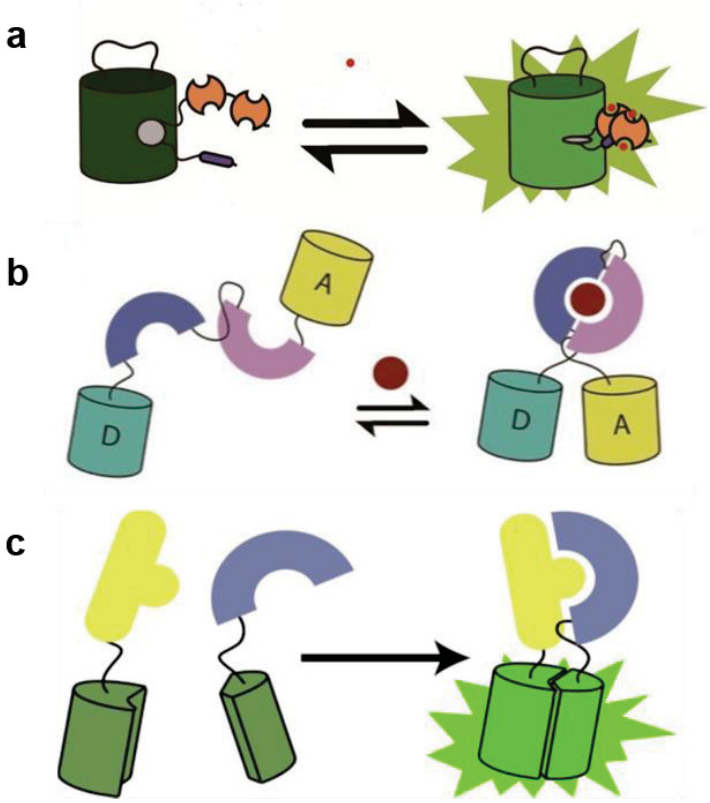

Figure 1.3 Schematic representation of the structures and sensing mechanism of different types of FP sensors. (a) Single FP-based sensor. (b) FRET based sensor. D represents donor and A represents acceptor. (c) BiFC based sensor. Reprinted with permission from Alford *et al*[87]. © John Wiley and Sons 2012.

The design of BiFC based sensors (Figure 1.3c) is different from the two types of sensors mentioned above. By genetically splitting an FP into two parts, the fragments lose the fluorescence because they lack the required interactions. When brought close enough to each other the two fragments can combine, interacting to form an FP and emit fluorescence[95]. Such phenomenon can be used to design BiFC based sensors to investigate protein-protein interactions[96]. However, BiFC based sensors have the drawbacks of slow kinetics and an irreversible process of

complementation[95]. The recently developed dimerization-dependent FP sensors provide new solutions to those problems[97,98].

1.2.3 FP-based Ca^{2+} sensors

Ca^{2+} ion plays a significant role for cellular signaling[99–101]. Ca^{2+} can bind to many functional proteins and enzymes for their activation or deactivation, and transduce signals in direct or indirect pathways. Normally, the concentration of cytoplasmic Ca^{2+} is maintained around 100 nM and strictly regulated. Excess cytoplasmic Ca^{2+} can be pumped outside of the cell or into the endoplasmic reticulum and the mitochondria. However, the concentration of Ca^{2+} can increase from either extracellular Ca^{2+} entering through ion channels in the plasma membrane, or through intracellular Ca^{2+} stores when the cell is stimulated by a specific signal for Ca^{2+} release. Thus, developing intracellular Ca^{2+} sensors can help researchers study and understand signaling in cells and other related physiological processes.

To monitor intracellular changes of Ca^{2+}, a number of synthetic organic molecules have been developed as Ca^{2+} sensors, for which the fluorescence changes upon Ca^{2+} binding[102–104]. These synthetic dyes demonstrate great selectivity for Ca^{2+}, fast association and dissociation kinetics, good photostability and pH resistance. However, there are also some disadvantages that limit the application of synthetic sensors. For example, the dyes may leak out of cells or compartmentalize into organelles during long-term imaging. There is also no specificity for different cell types or subcellular labeling, which makes Ca^{2+} imaging of complicated tissues or subcellular signaling difficult.

To overcome the restrictions mentioned above, genetically encoded Ca^{2+} sensors based on FP have been created by fusing FP with Ca^{2+} recognition domains followed by protein engineering techniques to adapt their performance since 1997[105]. Generally, FP-based Ca^{2+} sensors are categorized into two classes according to their construction, FRET based and single FP-based sensors (Figure 1.4). A FRET based Ca^{2+} sensor employs two FPs with either Calmodulin[105–109] or TnC[110–113] for Ca^{2+} recognition. Sensors that utilize Calmodulin also contain a short peptide for Calmodulin binding such as M13 from myosin light chain kinase. Upon binding Ca^{2+} Calmodulin interacts with M13, inducing a conformational change and increases the FRET efficiency. TnC is another Ca^{2+} recognition domain used to construct Ca^{2+} sensors, and no binding peptide is required for a large conformational change when binding with Ca^{2+}. Many FRET based Ca^{2+} sensors have been reported that demonstrate good performance for intracellular imaging, such as yellow cameleon (YC) 3.6[108], YC-Nano[109], TN-XXL[110] and 'Twitch' sensors[111].

A single FP-based Ca^{2+} sensor normally utilizes a circularly permutated FP with a Ca^{2+} binding domain. Extensive efforts on such sensors have led to a series of single FP-based Ca^{2+} sensors with different colors, Ca^{2+} affinities and kinetics for various applications[90,91,114–124]. For neuron imaging, fast kinetics and high sensitivity are critical functions of Ca^{2+} sensors, needed to resolve multiple action potentials within a short time. The GCaMP6 family was developed using neuron-based screening and first demonstrated higher sensitivity than synthetic dyes for Ca^{2+} sensing, as well as fast kinetics. To reduce the effect of autofluorescence from the biological samples and realize deeper tissue imaging, Dr. Campbell's group engineered red genetically encoded Ca^{2+} indicators for optical imaging (R-GECO1), showing red color fluorescence[120]. Masatoshi Inoue *et al* further improved R-GECO1 and developed R-CaMP2 with higher sensitivity and faster kinetics then R-GECO1 by replacing the M13 domain with CaMKK-a and CaMKK-b[124].

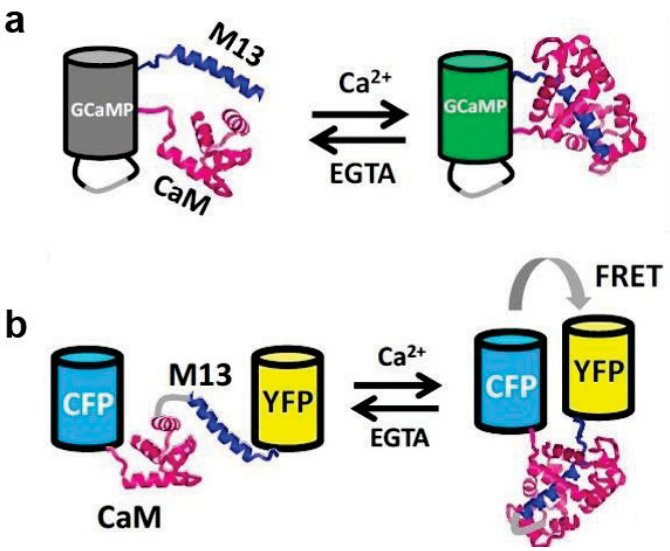

Figure 1.4 Schematic representation of the sensing mechanism of FP-based Ca^{2+} sensors. (a) Single FP-based Ca^{2+} sensors GCaMP. (b) FRET based Ca^{2+} sensors using CFP and YFP. Reprinted with permission from Lindenburg *et al*[118]. © 2014 by the authors; licensee MDPI, Basel, Switzerland.

1.2.4 Protein engineering strategies

To generate proteins with new functions and superior characteristics, two protein engineering strategies are used, rational design and directed evolution. Rational design is usually based on the crystal structures of the proteins or computational simulation of the relation of sequence, structure and function[126–130]. The environment and potential interactions of a specific amino acid can be investigated to help predict the results of introducing mutations to improve a specific function.

Directed evolution provides a different way for protein engineering. To mimic evolution in nature, random mutations are introduced into the original proteins and libraries of variants of the proteins are screened for a specific function and then selected. Based on selected variants, new libraries can

be generated for the next round of selection so that beneficial mutations are retained in the evolution[131,132]. Directed evolution offers a practical pathway towards proteins with improved capabilities that requires less knowledge of the relationship between structure and function. Despite the effectiveness of directed evolution, this technique is time-consuming and labor-intensive. Developing high throughput and automated screening systems is thus desired to increase the chance of identification and selection of improved variants with less time and effort.

Automated microtiter plates system were introduced to develop proteins with a throughput of $> 10^4$ variants a day. For example, the thermostability of two enzymes, laccase and peroxidase, was enhanced by plate reader based directed evolution[133]. However, the power of such systems is limited by the long measurement time for each variant and the relatively small library screened. FACS offers more advantages for directed evolution, due to its capability of high-throughput screening (up to 10^8 variants per day[134]). Stephen Withers and coworkers demonstrated directed evolution of glycosyltransferases by FACS, screening a library of $> 10^6$ variants within two hours[135]. David Liu's group evolved sortase A with 140-fold increased catalytic activity after eight rounds of screening by FACS[136]. The development of microfluidic technologies has enabled researchers to build up advanced cell sorting systems with high throughput and additional sample processing that is not easily realized on conventional FACS. Utilizing the droplet-based microfluidic system, the Griffiths and the Weitz groups performed directed evolution of proteins (a library of $\sim 10^8$ in ten hours) expressed in either cells[47] or a cell-free system called *in vitro* transcription and translation (IVTT) encapsulated in droplets[63,64]. However, most of the existing microfluidic FACS can only screen for one parameter of the proteins, restricting the power of directed evolution since other important characteristics of the proteins are ignored in the screening. Therefore, a multi-

factor screening system is desired to improve many useful properties of a protein in the same round of screening and increase the efficacy of directed evolution.

1.2.5 Microfluidic system for developing FPs

Since 2011, the research groups of Palmer and that of Harrison/Campbell, have been developing a microfluidic flow cytometer to improve the manual processes employed in cell-based screening to develop new fluorescent protein (FP) variants by directed evolution. Several performance elements have been important in developing these systems. A key factor is the throughput, or number of cells per second that can be evaluated, while another is the ability to then sort and collect cells. The ability to enhance rapid evaluation of the FP products is a goal pursued by the Palmer team, while applying the devices within a directed evolution screen to produce enhanced variants has been a target of both research teams. The nature and complexity of the screen being performed is also important, with the development of systems capable of multi-parameter screens being a key goal for more efficient directed evolution. The development of real-time pair matching strategies for multi-parameter screens within the μ-FACS devices has been a subtext within this work, which has had significant impact on efficacy and throughput of the μFACS devices. A detailed review of Palmer's work on photobleaching and photophysics is presented below, followed by a discussion of their work and then Harrison and Campbell's on metal ion sensitive FP's.

In 2011, Lubbeck *et al* introduced a microfluidic flow cytometer with multiple fluorescence detection beams to quantify photobleaching of red fluorescent proteins (RFPs) expressed in mammalian cells at a thoughput of 20 cells/s. To fabricate the device, a silicon wafer was etched

to generate microfluidic patterns and then bonded to a glass slide. Cells were focused by two dimensional sheath flow. Three laser beams were linearly expanded to reduce the spatial intensity variation of each beam and focused on the microchannel. The three beams included a high-intensity beam to photobleach RFPs, with the other two low-intensity beams to probe fluorescence signals before and after photobleaching. Data processing was conducted after experiments to determine the photobleaching rate of each cell. Four known RFPs mixed in samples were partially resolved optically according to the extent of photobleaching in the platform. The throughput was limited by pair-matching of the pre- and post-photobleaching signals from the same cell. Since all the signals were collected by one photomultiplier tube (PMT), multiple cells entering the detection region led to difficulties in pair-matching with high accuracy. The average passage time, Δt, from beam 1 to beam 3 was ~ 0.05 s and so the throughput was held to 20 cells/s, such that one cell left the three-beam region before the next cell entered.

The above microfluidic flow cytometer was then modified with an increased number of laser beams and optical tweezers for cell sorting. A microfluidic design was etched in borosilicate glass. Up to eight beams were employed to measure fluorescence from RFPs after photobleaching, to better distinguish RFPs with a low photobleaching rate. The optical tweezer was a focused 1064 nm laser spot, used for optical gradient force switching. The collection efficiency was optimized (>90%) by placing an additional laser beam at the collection channel for verification. Exposure to the optical tweezer resulted in a decrease in cell viability to 80% after 24 hours. The throughput of the cell sorting system, limited by the pair-matching, ranged from 6-46 cells/s, depending upon the number of beams, which ranged from 4 to 8. A known mixture of two RFPs, mCherry and mOrange with a ratio of 1:3, was screened to sort for mCherry, which showed higher photostability than mOrange.

When collecting 10% of the cells in the mixture based upon photostability, the resulting purity of mCherry containing cells was greater than 99%.

In 2015, Dean *et al* applied the established cell sorting system to screening libraries of mCherry variants to improve its photostability through directed evolution. The system employed four beams to characterize photobleaching and the throughput of screening was 5-8 cells/s. Two rounds screening a total of 56000 cells (42000 cells in the first round and 14000 cells in the second round) for photobleaching were performed to sort variants within the top 1/3 for photostability in each round. A two-factor screening based on both photostability and fluorescence brightness was conducted in parallel on the 14000 cells after the first round screening. Both the one-factor and two-factor screening led to beneficial mutants with increased photostability, but decreased brightness.

The microfluidic cell sorter was further enhanced to enable high throughput two-parameter real-time measurement of fluorescence lifetime and photostability with nine laser beams. The first beam was a high-frequency sinusoidally modulated laser beam which functioned as an excitation source to measure frequency-domain fluorescence lifetime. The following eight beams measured the photostability of RFPs, similarly to the work above. The reported throughput was up to 180 cells/s and 10^4-10^5 cells could be measured in < 10 min. The great improvement of throughput was attributed to better pair-matching when using two separate PMT channels for pre- and post-photobleaching signals. In this design the time window in which a mismatch of cells is likely is reduced to a small value, δ, determined by the variance in flow velocity during the transit time, Δt,

rather than the transit time itself. This reduced error window allows for a greater cell concentration. Practically, the system was operated at a more conservative throughput, 20 cells/s, to allow for sufficient photobleaching. The manuscript demonstrated the ability to distinguish three different RFPs in a mixture and identify cells with rare mutants in libraries of RFP with gene variations, but cell sorting was not applied in the system.

In 2012, the Palmer group devised another glass microfluidic flow cytometer using two beams to evaluate analyte-induced fluorescence change of FP-based sensors at a throughput up to 15 cells/s. They measured the cell to cell variance of specific FP variants, and the kinetics of the fluorescence-changing reaction. The two beams were placed at the upstream and downstream of a 60 mm long serpentine channel, allowing for a reaction period to induce fluorescence change. The reaction time can be tuned from 1 ms to 10 s by adjusting the flow rate and the designed length of reaction channel. The concentration change of the analyte was realized by diffusion of a metal ion from a sheath flow stream, inducing fluorescence change of the sensors. Pair-matching was achieved according to the average travel time from detector 1 to detector 2, Δt, again using post-experiment data processing program. As signals excited by both beams were collected by only one PMT, throughput was determined by the need to have a low enough concentration of cells that the probability of multiple cells appearing to overlap at one detector when being matched to a signal at the other is low. With one PMT for both detectors the upstream and downstream signals needed to be further identified. The authors used a change in peak shape induced by increasing the volume and velocity of sheath flow between the detectors to accomplish this. Using the flow cytometer, the researchers measured the single cell variation of fluorescence change of single variants of FP-based Ca^{2+} and Zn^{2+} sensors and the kinetics of fluorescence changes in the cells.

The Palmer group developed an alternate approach to controlling pair matching using a droplet-based microfluidic cell sorter, described in 2016, following the work of others, discussed above, on droplet based μFACS. This system allowed real-time data processing program for measuring and then sorting Zn^{2+} FP sensors. In a PDMS-glass device, single cells were encapsulated in droplets together with buffers containing Zn^{2+} to induce signal change. Droplets were actively sorted by dielectrophoresis. The system screened up to 7 cells/s, limited by the minimum droplet spacing required to prevent collision of the droplets, and the low 9 % cell occupation of droplets used to minimize multiple cell occupation in one droplet. Droplet formation provided less variable linear velocity, δ, within the travel time, Δt, giving for example 5.6 s ± 3 ms at a velocity of 25 mm/s. Pair-matching efficiency was thus enhanced, as observing multiple cells within the time window 2δ rarely happened at the given throughput. A mixture of two known Zn^{2+} sensors, NES-ZapCV2 and NES-ZapCV5, (ratio 1:9 or 2:8) were screened to sort ~ 8% of 40,000 cells for enrichment of NES-ZapCV2 over 2 hours. The enriched sample contained > 90% purity of the target. This microfluidic cell sorter was not utilized for screening libraries of variants in a course of directed evolution of FP-based sensors.

In 2014, Dr. Harrison and Campbell's group demonstrated a one-phase flow, cell sorting system to select sensors expressed in *E. coli* cells showing higher brightness, with 100-fold increased throughput (> 150 cells/s and 10^6 cells/round) compared to conventional manual screening on agar plates. This was the first directed evolution of FP performed with a uFACS system, and was the first using single phase flow rather than droplets for directed evolution studies. The PDMS-based

microchip with an integrated piezoelectric actuator for cell sorting served as the first step in screening to enrich for the top 0.1% improved variants from a library. This stage was followed by a second manual screen to accurately identify and verify the best of the μFACS-selected variants. The two step process could be repeated multiple times. Based on this established microfluidic cell sorter, we conducted detailed characterization of the cell sorter in Chapter 2 to optimize the sorting system and evaluate the effect of the protein expression level on directed evolution.

The performance of our microfluidic cell sorter with single point detection is limited, since only the brightness of the sensor can be screened and other useful properties of the sensor may be diminished. To improve upon the previous microfluidic cell sorter, in this thesis we introduce a two-point detection system capable of a two-parameter screen, to perform directed evolution of an FP-based Ca^{2+} sensor in Chapter 3. The new cell sorting system utilizes two fluorescence microscopes to obtain signals at two different points along a flow path in which a change in concentration of the analyte, Ca^{2+}, is induced. The two detectors thus determine the magnitude of fluorescence change of the sensor following reaction, along with the overall brightness of the sensor. A design for 3D focusing flow was configured to enhance the spatial control of cells and signal pair-matching. The cell sorter screens both the brightness and Ca^{2+}-dependent fluorescence change of the sensor at a moderate throughput (10 cells/sec and 10^5 cells/round) and selects for the top 1% variants for the second-step manual screening. This microfluidic-based platform greatly improves the selectivity of directed evolution compared to the microfluidic FACS with a single point detection, leading to variants of a Ca^{2+} sensor with increased brightness and greater Ca^{2+}-dependent fluorescence change after two rounds of directed evolution.

1.3 Centrifugal microfluidics

1.3.1 Overview

Centrifugal microfluidic systems can offer advantages compared to other existing microfluidic technologies, even though only limited success has been achieved in commercialization of centrifugal microfluidic devices. The integration of related techniques to create a system on a disc has contributed tremendously to the rapid advancement of biomedical and bioanalytical research tools for inexpensive, automated and user-friendly diagnostic systems[137,138]. Compared to many other microfluidic platforms, centrifugal microfluidics features simple and low-cost instrumentation because of the simple rotational means of actuating flow. The core component is a disc fabricated with microchannel patterns that is mounted on a spinning motor, as illustrated in Figure 1.5. Fluid propulsion is realized by centrifugal force generated by the motor, requiring no additional pumps. The sample processing device is fabricated on inexpensive plastic material like polycarbonate or PMMA. With customized device design and relatively large processing volume (up to sub-milliliter), a wide range of real samples have been tested and successfully processed in these devices[137].

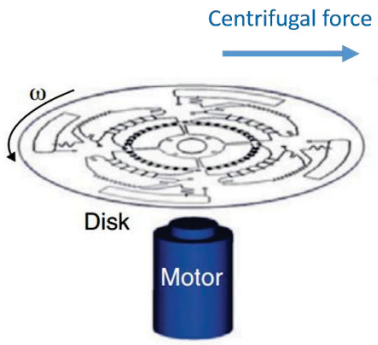

Figure 1.5 Schematic demonstration of a centrifugal microfluidic system.

Liquid in centrifugal microfluidic platform is mainly pumped by centrifugal force which originated from the centripetal acceleration of the spinning motor. At an angular rotational frequency of ω, the centrifugal force on an object (mass is m) at a point with distance of r to the centrifugal center is expressed as the equation (1.1).

$$F_c = -m\omega \times (\omega \times r) \tag{1.1}$$

For liquid (density ρ) in this platform, differential pressure Δp is often used to describe the centrifugal pressure on a liquid by equation (1.2), where r_1 and r_2 are the radial distance of inner and outer points of the liquid.

$$\Delta p_c = \frac{1}{2}\rho\omega^2\left(r_2^2 - r_1^2\right) \tag{1.2}$$

When a particle (with cross section A) in a liquid is moving relative to the liquid at a velocity u, it suffers from a drag force as presented in equation (1.3), where C_d is the drag coefficient.

$$F_d = C_d \frac{\rho_{fluid}}{2} u^2 A_{particle} \tag{1.3}$$

Aside from centrifugal force, fluid in centrifugal microfluidic systems can also be manipulated by using other forces such as capillary force, pneumatic force and magnetic force[138]. Using these additional forces may require special chip design and additional instrumentation.

The first centrifugal analytical device was developed by Anderson from Oak Ridge National Labs in the late 1960s, which is called a centrifugal analyzer[139]. The analyzer consisted of a rotating disc where channels and other features were fabricated, and used a fixed optical detector for absorbance measurement. Based on the centrifugal analyzer, Abaxis, Inc introduced an improved centrifugal analyzer for blood analysis in 1989[140] and then an integrated analyzer called Piccolo rotor system in 1995 which included sample processing steps[141]. However, the operation was complicated and

required highly-trained operator. Madou and Kellogg demonstrated a new centrifugal microfluidic system in 1998 called the LabCD for various on-chip liquid manipulations required for diagnosis, which overcame the limitations in a macro-scale analyzer[142]. LabCD led to rapid development of centrifugal microfluidic systems and their applications on biochemical and clinical analysis.

Nucleic acid analysis has been successfully realized in centrifugal microfluidic devices by many groups. For example, DNA from lysed blood cells can be purified by using solid phase extraction with integrated silica membrane in the disc[143]. On-chip PCR amplification of DNA was developed for detection and quantification with high sensitivity[144–147]. Jung and coworker introduced reverse transcriptase PCR to analyze RNA in virus[148]. Researchers also performed immunoassays in a centrifugal disk since immunoassays requires many processing steps which are easily conducted in an automated centrifugal microfluidic platforms. The reaction time of on-chip immunoassays is also reduced because of the fast diffusion in smaller volumes of reagents. Lai *et al* reported enzyme-linked immunosorbent assay (ELISA) in centrifugal microfluidic system to analyze rat IgG[149]. Their work demonstrated the same detection range as conventional methods, and advantages with regard to reaction time and regent consumption. A fully automated disc-based ELISA system was realized by Lee *et al* for the analysis of HBsAg and Anti-HBs, an antibody and an antigen, from whole blood[150]. Although large amounts of work have been reported for biochemical analysis, only a few studies on metabolite analysis have been demonstrated as we will discuss below.

The integrated detectors for centrifugal microfluidic systems are typically optical and electrochemical sensors which are not easily applied to the detection of various small molecules. The analysis of glucose[151] and alcohol[152] in whole blood with absorbance-based detection was demonstrated. In the studies, enzymatic reaction-based colormetric assays were used. The assays

included the oxidase for glucose or alcohol, horseradish peroxidase, and a dye as indicator. Reagents were mixed with 100 times diluted whole blood samples for reaction, followed by the removal of the blood cells, the main interference for detection in the sample, by centrifuge. Another disc-based system with an electrochemical detector was devised for quantification of three metabolites, glucose, lactate and uric acids, from a whole blood sample[153]. The platform also employed centrifugal force to separate blood cells and then quantified the analytes by enzymatic reaction-based assay and chronoamperometry. In those studies, the biomolecules and small molecules dissolved in blood samples like proteins, lipids and salts did not cause interference for the detection, so additional sample preparation steps were not needed.

1.3.2 Device fabrication and packaging

Differing from PDMS based microfluidic devices, which is fabricated by soft lithography[154,155], centrifugal microfluidic devices are generally based on thermoplastics like polycarbonate and PMMA. Devices can be fabricated by milling machine[146,156] and CO_2 laser cutter[157,158] when high resolution fabrication is not needed. Using these simple fabrication methods, researchers can easily modify and optimize the design of the microfluidic device for testing, as the design is directly fabricated on the plastic substrate and multiple steps involving photolithography are not required. Problems can arise due to the low resolution and rough surface generated during fabrication, which may lead to unexpected flow behaviour. Those problems can be resolved with fabrication by hot embossing, where a master mold is needed to transfer the design to thermoplastic substrates[159,160]. Like soft photolithography, design-to-device time is relatively long due to the generation of a master before prototyping on plastic devices, making design optimization inconvenient. For thermoplastic based centrifugal microfluidics, device sealing and packaging are often realized using pressure sensitive adhesive (PSA) film. PSA film is first cut by a programmable cutter plotter

and then sandwiched between two pieces of fabricated thermoplastic layers for lamination. Strong bonding forms between PSA and thermoplastic layers when pressure is applied during lamination. The thermoplastic layers can be patterned with channels for large volume microfluidic storage and processing, as the depth of features like reservoirs and channels can be > 1 mm. The PSA layer with a thickness of ~100 μm, can be patterned and so offer features with low aspect ratio (shallow and wide) for fluid manipulation.

Recently, a new fabrication method was introduced by the Landers group called the print, cut and laminate (PCL) approach[161]. This method utilizes commercial polyester transparencies for printing as substrates and a laser cutter with no other complex instrumentation for fabrication. In this method, transparencies are first printed with toner by an office printer, cut by a CO_2 laser cutter and then assembled into a multilayer device by hot lamination. The toner serves for bonding between two layers as it melts and cools down during hot lamination. One limitation of this fabrication technique is the less precise control of the depth of features because the depth is primarily determined by the numbers of layers and the reproducibility of the acetate film thickness. Thus, the depth is controlled by an increment of ~ 100 μm, which is the thickness of one layer. Also, a typical device with up to 9 layers (7 internal layers) can only have features up to 700 μm in depth, restricting the volume of the sample processed on chip. To increase the capacities of micro channels and chambers, a hybrid device was successfully generated using polyester and PMMA bonded with toner[162]. Using this PCL approach for rapid prototyping with cost-effective materials and instruments, many centrifugal microfluidic devices for bioanalytical applications have been reported, such as DNA extraction and amplification[163,164], white blood cell enumeration[165] and illicit drug analysis[166].

1.3.3 Detection

1.3.3.1 Optical detection

On-chip optical detection is widely used in centrifugal microfluidics as with other microfluidic systems, since precise position control of the disc and optical alignment are not difficult to realize. For example, researchers conducted fluorescence spectroscopy with high sensitivity for DNA analysis and immunoassays[146,147,167–170]. On-chip absorption spectroscopy was achieved by a total internal reflectance scheme for light beam guidance[151]. For simple visual detection, colorimetric assays were utilized to give qualitative signals by color change[171,172]. Recently, it has been shown that a mobile phone can function as a detector instead of a conventional CCD or PMT detector[163,173]. Signals are acquired by taking photos of the assays and processed by software for color analysis. In an effort to optimize and simplify the instrumentation for a Lab-on-a-CD, a standard CD or DVD drive has been used for on-chip detection[174–177]. Without modification to the drive, biomolecules attached to the surface of a disc can block the laser beam and report error signals which reflect the location on the disc.

1.3.3.2 Electrochemical detection

Several centrifugal microfluidics with electrochemical detection have been demonstrated by integrating electrode on chip, typically as a three-electrode setup[153,178,179]. In one example, target antigen was captured by a bead based ELISA and quantified by amperometric analysis, with a 17-fold improvement on limit of detection by optical methods on analysis of C-reactive protein[178]. Electrochemical detection of small molecules in whole blood such as glucose, lactose and uric acid was reported by utilizing working electrodes immobilized with enzymes and measuring H_2O_2 generated from enzymatic reactions[153]. In addition, researchers also used on-chip impedance detection to analyze cancer cells from whole blood in centrifugal microfluidic platform[180].

1.3.3.3 Detection using standard analytical instruments

Despite the success of on-chip detection in a centrifugal microfluidic system, its bioanalytical applications are still hindered by inherit limitations of the integrated detection techniques, such as poor specificity, or too narrow a range of compounds that can be analyzed. Standard analytical instruments such as mass spectrometry provide far better resolving power for measuring a broad range of analytes, but may never be integrated for on-chip detection. Moreover, integration of all detection components in a disc may make it very expensive, and so not suitable for a low-cost single use device. Regenerating the centrifugal disc for repeated usage requires additional effort and may not be successful at all with biofluids. Thus, developing a sample preparation device for detection by commercial analytical instruments could help to make centrifugal microfluidic platforms with better versatility.

A high-throughput sample preparation device was created to study protein digestion by MALDI mass spectrometry analysis[181]. The disc could process 96 samples at one time and a multi-step preparation using a chromatography column including pre-concentration, desalting and elution was developed. Prepared samples were then crystallized with a MALDI matrix on chip in the detection areas and were analyzed by inserting the CD into a mass spectrometer. This commercial effort collapsed when sales did not meet expectations. Another prototype of a centrifugal sample preparation platform was developed by taking advantage of a solid phase extraction column to preconcentrate the target molecules, followed by laser ablation inductively coupled plasma mass spectrometry to analyze trace metals in water samples[182].

Centrifugal microfluidic technology has demonstrated great sample preparation ability for the analysis of several metabolites such as glucose, alcohol, lactate, and uric acids with electrochemical[153] or optical detection[151,152], as we discussed in 1.3.1. However, sample preparation using centrifugal microfluidic devices for metabolomics has not been reported. Metabolomics typically utilizes mass spectrometry or NMR to profile and study a relatively large set of metabolites in a biological sample at one time[183,184]. Electrochemical and optical detectors are not easily applied to metabolomics since they are not powerful as mass spectrometer or NMR in distinguishing and identifying many molecules within a complex system, due to their lower specificity and resolution. Since the analysis of metabolomics by mass spectrometry or NMR requires sample pretreatment to reduce the effect of the sample matrix in biofluids, creating a generic centrifugal disc with the function of sample clean-up is desired. In Chapter 5, we describe the first centrifugal microfluidic device to prepare samples for metabolomics analysis by mass spectrometry. Low molecular weight ionic metabolites from human serum samples were selected as analytes. Proteins and lipids were removed from the sample on chip. The sample was then spotted on a silicon nanostructured film with perfluoro-coating[185] to segregate salts from the metabolites. The film then served as the substrate for metabolite analysis by solid matrix laser desorption ionization mass spectrometry.

1.4 Laser desorption ionization (LDI) mass spectrometry

1.4.1 Mass spectrometry

Mass spectrometry (MS) has been used as a powerful tool in analytical chemistry over decades. In mass spectrometry, positive or negative ions are produced and resolved electrically according to their mass-to-charge ratio. Traditional ionization techniques include electron ionization (EI) and

chemical ionization (CI)[186,187]. EI utilizes beams of accelerated electrons to collide with analytes, whereas CI ionizes analytes using charged ions of a reagent gas such as methane. The high energy of electrons in EI can generate amounts of fragments of molecules, providing more structural information of analytes but complicated spectra. CI produces more molecular ions instead of fragment ions because of its lower energy. Neither method can volatize macromolecules without destroying them, due to the high energy which they impart.

The advancement of two soft ionization techniques, matrix assisted laser desorption ionization (MALDI)[188,189] and electrospray ionization (ESI)[190,191], has facilitated the application of MS in qualitative and quantitative analysis of biomolecules such as proteins and peptides. Compare to EI and CI, those two soft ionization methods generate fewer fragments due to the much lower energy transmission to the analytes in the process of ionization. ESI-MS offers the advantage of direct connection with liquid separation techniques in that molecules are ionized from the liquid phase, whereas MALDI produces ions from a solid phase and is typically coupled offline to separation techniques. However, MALDI has demonstrated higher tolerance to contaminants and less complex spectra due to generation of singly charged ions compared to the multiply charged ions produced by ESI[186].

1.4.2 Matrix assisted laser desorption ionization (MALDI) mass spectrometry

MALDI has been successfully used by researchers to study various types of biomolecules such as proteins[188,192], lipids[193–195] and DNA[196–198]. To prepare samples for analysis, the analyte is first dissolved in solution together with excessive matrix molecules and then spotted on a metal plate for drying where the sample and matrix are cocrystallized. Desorption and ionization of the sample and matrix is induced by a laser beam (typically a 337 nm nitrogen laser) that hits the sample spot.

The matrix molecules transit to gas phase along with the analytes once the matrix absorb the energy from the laser. To facilitate ionizations, acidic or basic molecules are selected as the matrix to provide or accept protons for the analytes after desorption[199].

Although MALDI has demonstrated its capability in analytical chemistry, there are some limitations to its applications. Firstly, the detection of analytes in low mass range (<1000) is difficult as the matrix molecule which is also in this range causes significant interference in the spectra. Secondly, signals vary at different points in a sample spot due to heterogeneous cocrystallization, resulting in large variation and poor reproducibility of the results. Thirdly, matrix selection for different target analytes is critical to the quality of the results and requires additional effort[200].

1.4.3 Matrix-free laser desorption ionization mass spectrometry

To overcome the limitation of MALDI, researchers successfully developed matrix-free laser desorption ionization mass spectrometry on porous silicon (DIOS)[201]. Instead of using matrix to assist desorption and ionization, the semiconductor property of porous silicon allows it to absorb laser irradiation which will be converted to heat for desorption and ionization (Figure 1.6). Moreover, the porous surface increases the surface area of the silicon for both photon absorption and analyte trapping. In 2007, an improved LDI mass spectrometry called nanostructure-initiator mass spectrometry (NIMS) was introduced by the Siuzdak group[202]. In this technique, desorption/ionization of the analyte was achieved with the help of the liquid "initiator" such as perfluorinated molecules. Trapped in a nanostructured surface, the "initiator" molecules are vaporized but not ionized upon heat generation caused by absorption of laser by silicon surface. The vaporization of the "initiator" facilitates desorption and ionization of analyte molecules

adsorbed on the surface. The application of NIMS includes small molecule detection in biofluids[202,203], enzyme activity study[204,205] and tissue imaging[206–208].

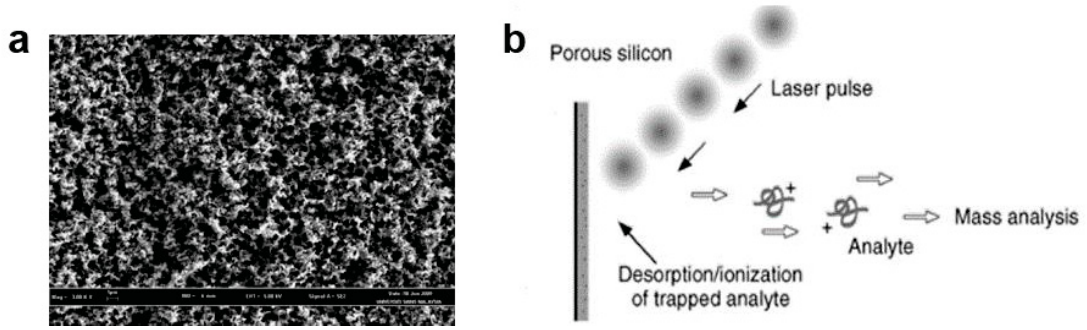

Figure 1.6 (a) SEM image of electrochemical etched nanoporous silicon. (b) Matrix free LDI-MS on nanoporous silicon. Reprinted with permission from (a) Ramizy *et al*[209]. © Emerald Group Publishing Limited 2010. (b) Wei *et al*[201]. © Nature Publishing Group 1999.

Despite the successful application of DIOS and NIMS in analytical chemistry, those two techniques suffer from some problems attributed to their fabrication method. The nanostructured porous silicon is generated by electrochemical etching which requires strict experimental conditions and materials such as etching time, current, solutions and silicon substrate, making it difficult to precisely control the porosity of the nanostructured silicon as well as to get reproducible mass spectrometry results[199,210,211]. Furthermore, electrochemical etching produces reactive porous surface that can adsorb contaminants from the atmosphere, resulting in high background peaks in the spectrum[210].

1.4.4 Glancing angle deposition for nanostructured silicon

Physical vapor deposition is often utilized for nanostructured material production with better reproducibility because the fabrication parameters are well controlled by computer and the deposition process occurs in a vacuum chamber. One physical vapor deposition technique, glancing

angle deposition (GLAD), has been developed mainly by Dr. Michael Brett's group to fabricate thin films of inorganic nanostructured materials with controllable properties[212–216]. In the GLAD technique, the vapor flux of the materials is controlled to deposit on a substrate at an oblique angle (Figure 1.7a). Films of nanostructures with different morphologies are generated by adjusting operation conditions such as the glancing angle and the rotation of the substrate, which can influence the nucleation and crystal growth on the substrate. The GLAD technique has been successfully applied to fabricate different inorganic materials like semiconductor[217–219], metals[220–222] and oxides[223–225].

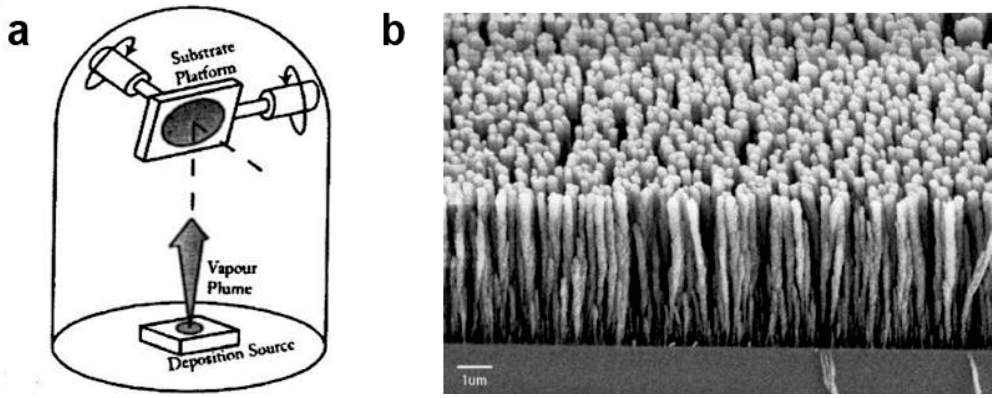

Figure 1.7 (a) Instrumentation of GLAD technique. (b) Silicon nanostructure fabricated by GLAD. Reprinted with permission from Hawkeye *et al*[214]. © American Institute of Physics 2007.

In collaboration with Michael Brett's group on GLAD, Dr. Harrison's group successfully realized matrix-free LDI-MS on silicon GLAD films with highly reproducible morphologies[226]. A variety of molecules with mass ranging from 150 to 2500 Da were detected including metabolites, peptides and drugs, showing lower chemical backgrounds, better reproducibility and lower detection limits than electrochemically etched nanoporous silicon. Other researchers have also found various types of GLAD films are useful for many other biological and chemical applications. For example, the

photo-electrochemical properties of GLAD fabricated nanomaterials have been studied for water oxidation and photovoltaics[227–229]. Ag GLAD films can be utilized for surface plasmon resonance sensing[221] and surface-enhanced Raman scattering[220]. A colormetric humidity sensor was demonstrated based on TiO_2 GLAD film[230]. Moreover, chemical and biological separation techniques such as ultrathin layer chromatography[231–235] and DNA separation[236] were realized based on the nanostructures fabricated by GLAD.

Our group has recently introduced a perfluoro-coated silicon GLAD film for solid matrix laser desorption ionization mass spectrometry (SMALDI-MS)[185]. The SMALDI film has the function of background electrolyte segregation from small ionic molecules, utilizing a salt crystallization step on its surface, before MS detection. Combined with ultrafiltration to eliminate macromolecules from serum, the SMALDI film was able to analyze metabolites in a clean background. Although protein removal by ultrafiltration is fast and robust, a large sample volume (>200 μL) and an expensive high-speed lab centrifuge are usually required, along with several other laboratory based steps. Here, we develop an inexpensive centrifugal microfluidic device to prepare small volume samples (~ 5 μL) for metabolite analysis by SMALDI-MS, with the various laboratory steps required integrated into a single fluidic device, as described in Chapter 5.

1.5 Scope of the thesis

The general background of the topics related to the thesis has been discussed in this chapter, including microfluidic cell sorting, fluorescent proteins, centrifugal microfluidics and matrix free laser desorption ionization mass spectrometry. The applications of those microfluidic technologies to solve biochemical problems will be provided in the rest of the thesis.

In Chapter 2, we describe characterization of a microfluidic cell sorting system that is used to screen fluorescent proteins to produce a higher brightness. The sorting performance of the system is examined and optimized to improve the efficacy of the screening. The effect of heterogeneous single cell expression level on the directed evolution is also discussed.

Chapter 3 introduces a new microfluidic cell sorting platform with an enhanced two-point detection system to simultaneously screen two factors, brightness and fluorescence change upon reaction with a target analyte for fluorescent protein based sensors. Compared to the platform presented in Chapter 2, the system described in Chapter 3 utilizes a simple 3D focusing flow for better cell handling, and the flow rate is studied to obtain maximal fluorescence change on chip. The throughput of the system is investigated and optimized according to pair-matching performance seen for the two detectors. Directed evolution of a fluorescent protein based Ca^{2+} sensor named Y-GECO1f, which may be used to measure Ca^{2+} change in different parts of a cell is performed. A microfluidic cell sorter with a two-point detection system is compared to that of our previous cell sorter presented in Chapter 2, which can only screen for brightness. The product of the directed evolution is further engineered by rational design to achieve different affinities to Ca^{2+}, which is described in Chapter 4. The Ca^{2+} sensor variants are characterized *in vitro*, in mammalian cells and in *Drosophila* visual system for performance evaluation.

Chapter 5 introduces a centrifugal microfluidic platform to prepare serum samples for metabolite analysis. The design of the centrifugal disc is described and an on-chip sample preparation assay is developed for protein and lipid removal. The prepared sample is tested with an offline solid matrix laser desorption ionization mass spectrometry for salt segregation and metabolite detection.

Quantification of several metabolites is conducted using the standard addition method. The performance of the sample preparation disc is assessed and compared to commercial ultrafiltration tubes.

Finally, a summary of the work is presented in Chapter 6 and some potential directions of future work on microfluidics for cell sorting and point of care analysis is discussed.

Chapter 2. Characterization of a microfluidic cell sorter by screening for higher brightness of fluorescent protein-based Ca^{2+} sensors

2.1. Introduction

Directed evolution is an effective approach for engineering fluorescent protein (FP)-based sensors with improved brightness and sensitivity, but it requires screening large libraries of variants[47,237]. Colony-based screening on agar plates has been widely used for directed evolution, successfully leading to many FP-based sensors with satisfactory properties[71,120–122]. However, colony screening is labor-intensive and only a smaller sized library can be screened in each round (10^4 variants every few days) when done manually, which restricts the opportunity to identify rare variants with exceptional function. To accelerate the process of directed evolution, an automated screening system with a high throughput is highly desired. Microfluidic systems provide a new approach for researchers to build up a high throughput screening platform for single cell analysis[9,12,238–240]. Compared to commercial flow cytometry, microfluidic systems offer several advantages, such as low cost, simple instrumentation, multi-use disposable devices for sample analysis, and versatility based on customized design.

To explore new instrumentation to support directed evolution for FP-based sensors, our group established a microfluidic cell sorting system with a throughput of > 150 cells/s[71]. The throughput was increased ~100 times compared to manual screening, screening and sorting up to 10^6 *E. coli* cells expressing FP-based sensors in 2 hours for cells with high fluorescence intensity. A following colony-based screening of the sorted cells was performed to eliminate false positive variants and

identify the variants with the most improved properties, enhancing the reliability of the process as a whole (Figure 2.1). By utilizing the μFACS-aided directed evolution approach, a new family of FP-based Ca^{2+} sensors called yellow genetically encoded Ca^{2+} indicators for optical imaging (Y-GECO) was successfully engineered from a yellow FP mPapaya1[242] (Figure 2.2). The *in vitro* characterization of purified Y-GECO1m, the best variant of Y-GECO, demonstrated a 95% decrease in fluorescence with excitation at 525 nm upon Ca^{2+} binding.

In this chapter, we present some performance characterization of our μFACS system using cells expressing Y-GECO sensors. Since the sorting performance affects the efficacy of directed evolution, we studied the sorting efficiency of the piezoelectric sorter by adding a second detector to the system. The parameters related to the sorting performance were examined and optimized. As a further characterization of the total system, we measured the FP expression levels of single cells from within a single colony for three different variants, to investigate how the expression level influences the selection results in directed evolution.

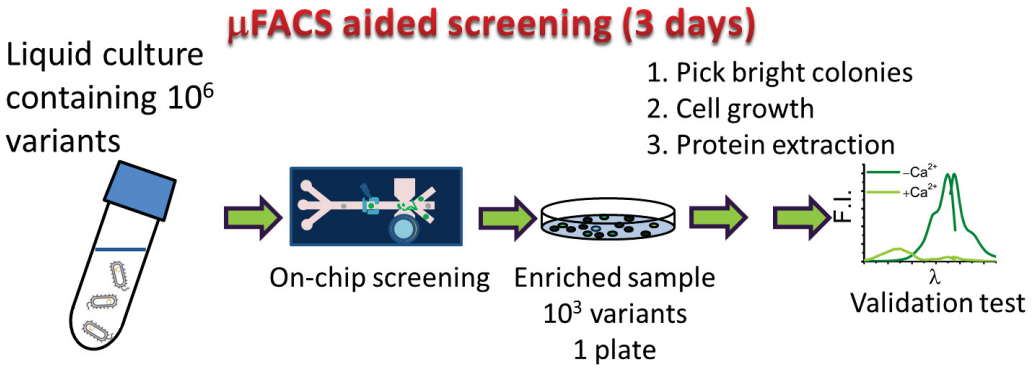

Figure 2.1 The general process of μFACS-aided directed evolution of FP-based sensors.

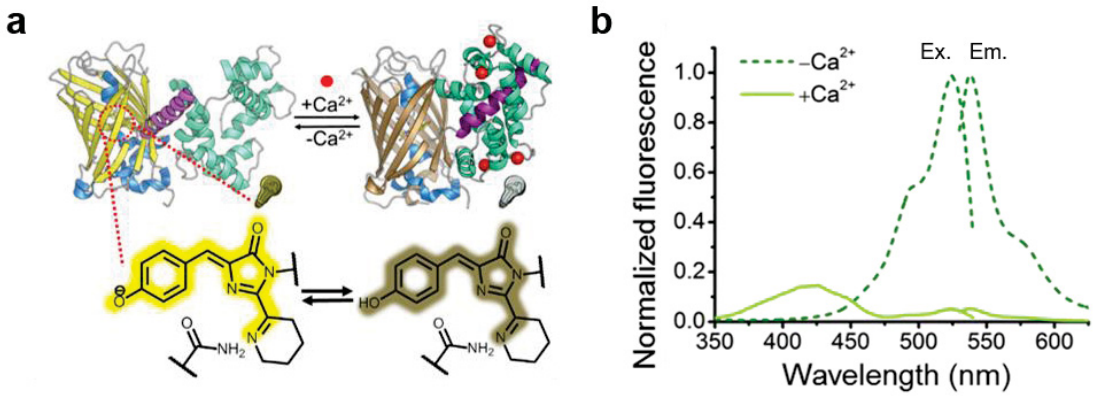

Figure 2.2 (a) Schematic representation of the Y-GECO structure, structural changes upon binding Ca^{2+} and changes in the aromatic fluorophore as a function of pH in relation to the sensing mechanism. (b) Normalized excitation and emission spectra of purified Y-GECO1m in Ca^{2+}-present and Ca^{2+}-absent states. Reprinted from Zhao *et al*[71]. © The Royal Society of Chemistry 2014.

2.2. Experimental section

2.2.1. Design of the microfluidic cell sorter and optical setup

The design of our μFACS platform is based on a PDMS microfluidic device with an integrated piezoelectric actuator for sorting, as illustrated in Figure 2.3a. Cells expressing FP-based Ca^{2+} sensors were suspended in buffers and injected into the device through the middle inlet channel by a syringe pump. The flow of cell suspension was focused in the center of the channel by the streams introduced by two side inlet channels. An epi-fluorescence microscope with a 505DRLP dichroic mirror, a 542/20 nm emission filter (FF01-542/20-25, BrightLine®), a 25/0.35 NPL Fluotar objective (Leitz Wetzlar) and a 800 μm pinhole was used to detect fluorescence signals. Fluorescence excitation was achieved by using a 488-nm argon laser and a photomultiplier tube (PMT) (R1477, Hamamatsu) was utilized for detection (Figure 2.4).

Signals are acquired at a sampling rate of 100 kHz and input into a computer for analysis by using a customized LabVIEW program, where intensity of the fluorescence peaks (peak height) are calculated. When cells demonstrate fluorescence intensities higher than the threshold, the system will trigger the piezoelectric actuator by applying a voltage. The actuator diaphragm bends to change the volume of the liquid in the reservoir below it upon receiving a trigger, deflecting the trajectory of a desired cell in the sorting region to one of the collection outlet channels (Figure 2.3b). A cell with a low fluorescence that does not trigger the actuator will go straight to the waste outlet channel. The width of each inlet or outlet channel is 50 μm. The channel which connects inlet and outlet channels is 5 cm long and 150 μm wide, designed for cells to travel in a central stream focused with sheath flows. The sorting region is 100 μm long and 150 μm wide geometrically. The depth of all channels is 50 μm.

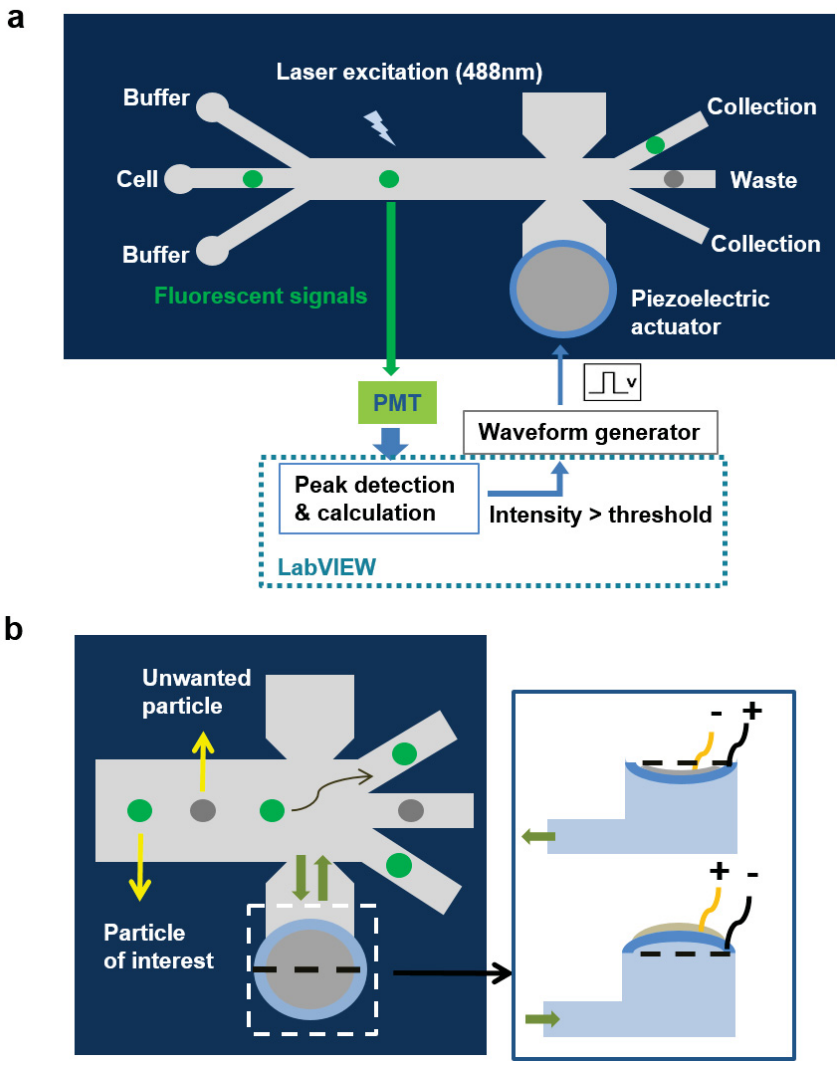

Figure 2.3 (a) Schematic representation of the μFACS design. (b) Working principle of piezoelectric actuator as a sorter.

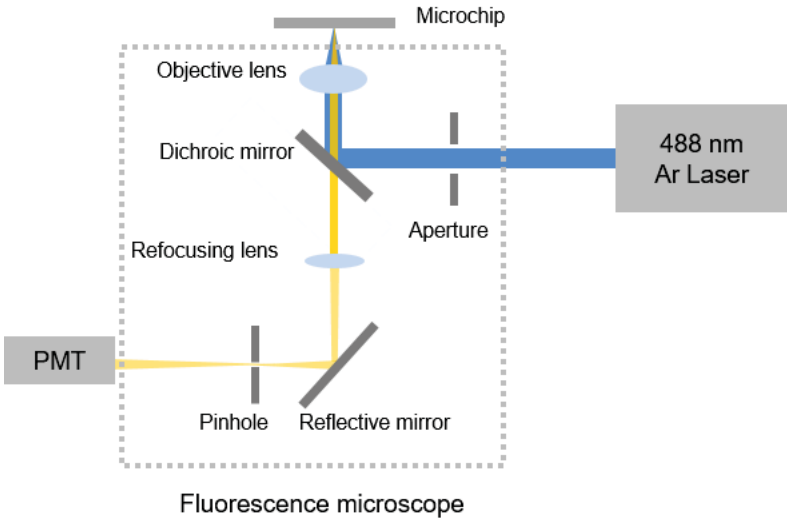

Figure 2.4 Schematic representation of the optical setup and the epi-fluorescence microscope for detection.

2.2.2. Device fabrication

The PDMS based device was fabricated by traditional soft photolithography[154]. An SU-8 photoresist master was patterned by UV on a silicon wafer and the pattern was transferred to PDMS by pouring a mixture (10:1) of PDMS base and curing agent (Sylgard 184, Dow Corning) over the master, followed by overnight curing at 60 °C. PDMS replicas were then removed from the master. The inlet and outlet holes were punched with a 2 mm punch and the actuation chamber was cut out with a surgical knife. The PDMS device and glass substrate were carefully put into physical contact after treating with air plasma for 1 min and transferred to a 60 °C oven for a 30 min incubation. A piece of piezoelectric actuator was placed over the actuator chamber and sealed by syringe epoxy adhesive (Gorilla Epoxy). The inlet and outlet holes were inserted with tygon tubing (AAD02103-CP, Cole-Parmer) and sealing was then achieved with syringe epoxy adhesive.

2.2.3. Preparation of *E. coli* cells expressing Y-GECO sensors for performance characterization of μFACS

E. coli cells expressing single variants were used for characterization. The gene that encodes each Y-GECO Ca^{2+} sensor was ligated to pTorpe plasmid vectors[120] and transformed into electrocompetent *E. coli* DH10B cells by electroporation. The transfected cells were placed on LB/agar plates containing 100 μg/mL ampicillin and 0.002% arabinose for overnight culture at 37 °C. The next day, single colonies were picked and suspended in M9 buffers. Cells were diluted to a desired density and delivered into the μFACS for characterization. For simple tests of signal collection and optimization of sorting efficiency, cells expressing the sensor Y-GECO1m were used. For expression level studies, the genes of three variants, Y-GECO0.5, Y-GECO0.7 and Y-GECO1m (Y-GECO1.0), were transformed into cells separately for culture and expression. Single colonies of each variant were picked and suspended in buffers for use.

2.2.4. Sorting efficiency measurement by using a piezoelectric actuator

By utilizing another epi-fluorescence microscope with PMT as detector, we interrogated the sorting efficiency of our μFACS system at different flow rates. As is shown in Figure 2.5, the first detector was placed before the sorting region to detect cells and activate the piezoelectric actuator for sorting. The additional detector was placed at a collection channel to verify that cells were successfully sorted. The sorting efficiency is defined as:

$$\text{Sorting efficiency} = \frac{\text{Number of verification signals}}{\text{Number of detection signals}} \times 100\% \tag{2.1}$$

Due to the large size of the detector (> 2 cm in width) relative to the short distance between the two detection areas (< 2 mm), two fluorescence microscopes could not be placed for detection on

the same side of the microchip. We therefore set the first detector under the device and the additional detector for verification over the device. With this optical setup, there is no minimum distance limit between two detection regions and sorting efficiency can be measured.

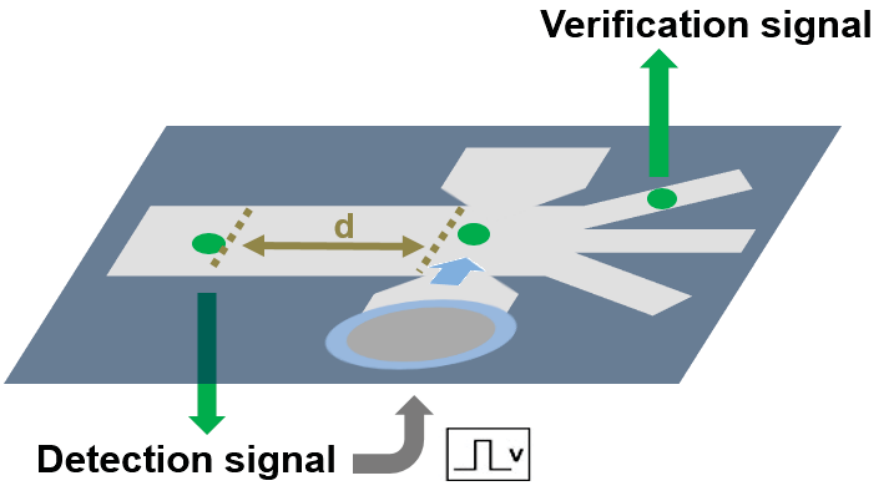

Figure 2.5 Measurement of sorting efficiency.

2.2.5. Measurement of the linear velocities of cells at different flow rates

To obtain the average linear velocity of cells at a specific flow rate, the two detectors were placed at the beginning and the end of the 5 cm long channel to measure the travel time of about 200 cells and the linear velocity was calculated as distance/travel time. The details of the flow rates and the measured average linear velocities are listed in Table 2.1.

Table 2.1 Flow rate setting[1] and average linear velocity[2]

Total flow rate (μL/min)	Sheath to center flow ratio	Flow rate of each sheath flow (μL/min)	Flow rate of center flow (μL/min)	Linear velocity (cm/s)
10.5	20:1	5	0.5	5.3±0.4
15.75	20:1	7.5	0.75	7.4±0.7
20.1	20:1	10	1	9.6 ±1.0

[1] Flow rate settings are given as the nominal setting values for each syringe pump. The pumps were not calibrated.

[2] Measured velocities determined from cell transit times between two detectors, error give is the standard deviation with n = 3.

2.2.6. Expression level of single colony

Three variants of Y-GECO sensors obtained from different rounds in the process of directed evolution were expressed in *E. coli* cells for on-chip measurement. For each variant, a single colony was picked, suspended in M9 buffer without Ca^{2+}, and diluted to a specific density (5×10^6 cells/mL) before injecting into the μFACS. The total flow rate in the μFACS (cell suspensions and sheath flows) was set to 10.5 μL/min with a sheath-to-center flow ratio of 20:1. Signals were continuously recorded for 10 s and 40 of such 10-s time traces were acquired for each colony. Fluorescence peaks were identified and peak height was calculated. The distribution of fluorescence intensity from a single colony of each variant were then plotted to compare the expression levels of different variants.

2.3. Results and discussion

2.3.1. Signal collection

Fluorescence signals from cells expressing Y-GECO1m were collected with a fluorescence microscope with a PMT detector, converted to voltage signals and collected by computer. Figure 2.6 illustrates the signals acquired over time when the total flow rate was set to 10.5 μL/min. The inset shows a peak collected for a single cell and its baseline peak width is ~ 0.2 ms. The diameter of the focused laser beam on chip is ~ 10 μm according to visual observation of its size relative to the size of the microchannel. The estimated linear velocity of the cell is ~ 5 cm/s, based on transit time through a laser beam. It is consistent with the average measured value 5.3±0.4 cm/s in Table 2.1, which is measured by the transit time between two laser beams.

The difference of the amplitudes of the signals from single cells is caused by three reasons. First, the abundance of the sensors expressed in each cell is not the same due to heterogeneous expression levels. Second, the focused laser spot is much larger than the cells and the intensity decreases from spot center to the edge changing the excitation intensity. Third, the parabolic flow profile will lead to some differences in cell velocity along different flow streams, even in a sheath flow design that centers the cell flow streams. Consequently, cells travelling along different flow streams at different velocities may experience different excitation intensity for different periods of time during a transit of the detection zone.

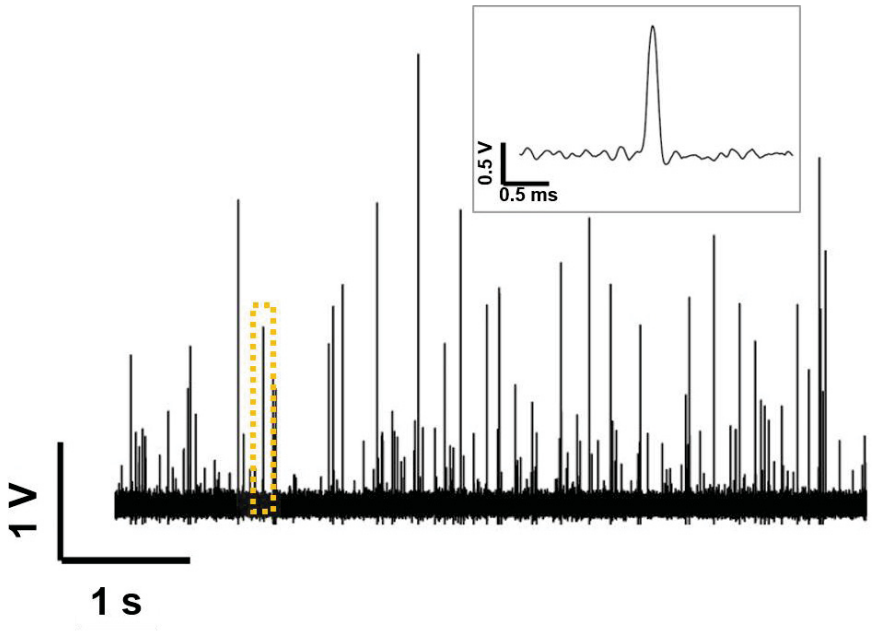

Figure 2.6 Spectra of acquired fluorescence signals from *E. coli* cells expressing Y-GECO1m. Inset: zoom-in time trace of the peak highlighted in the yellow box.

2.3.2. Sorting efficiency study

At a specific flow rate, the sorting efficiency is affected by distance from the detection point to the sorting region, time to trigger the actuator, voltage applied to the actuator and pulse width of the applied voltage. Since the detector for sorting is placed before the sorting region, a short time may be needed for a cell to reach the sorting region. So a delay time before sending the pulse to actuate the sorter is required, and the length of the delay time must be evaluated. The amplitude of the voltage applied to the actuator determines the extent of its bending and the volume of liquid being activated. A high voltage can generate too large a deflection, so that the cells may enter the actuator reservoir instead of the sorting channel, whereas a very low voltage may not deflect the cells enough from their original trajectory.

The pulse width of the voltage applied to the actuator is affected by the throughput. With a pulse width of 10 ms, the actuator can be activated up to 100 times in a second. Since the screening was performed at a throughput higher than 150 cells/s, the pulse width should be set below 7 ms. However, if the pulse width is too short a cell may experience deflection towards the sorting channel and then away from it before fully entering the sorting channel streamlines, and thus still enter the waste channel. The geometric length of the sorting region is 100 μm, but the actuator captures across a ~ 200 μm range because cells which are close to the geometric sorting region (± 50 μm) will also be deflected upon activation. The average travel time for cells is 4 ms at a flow rate 10.5 μL/min. Therefore, there is a chance of failure in sorting if the pulse width is shorter than 4 ms. On the basis of the above, a 5 ms pulse width was selected to maintain a high throughput and avoid failure in sorting due to too short a pulse.

Before studying the sorting performance, we first measured the response time of our system, from signal collection to actuation triggering, which affected the delay time setting. Voltage signals were generated from a pulse generator to mimic the fluorescence signals detected by a PMT, and collected in the computer for peak analysis. The amplitude of each signal was set to be higher than the threshold, so that it could output a pulse to trigger sorting. The input and output signals were also recorded using an oscilloscope and the response time was determined as the time difference between each pair of signals. We observed that the response time randomly varied from 2 ms to 10 ms with an average of 5.9 ± 2.9 ms from 15 signal pairs. The variation might result from the slow data processing using LabVIEW and electronics-induced timing jitter of the PC and data acquisition board which costs only < $500. The variation clearly makes precise timing control difficult. The problem can be solved by not using LabVIEW, so as to get a much faster response for the computer, or by building an external trigger circuit that does not use the computer. Chen

and coworkers reduced the response time of their μFACS system to < 10 μs using a more sophisticated electronic control that cost more than $2000, including an external drive embedded with a field-programmable gate array (FPGA) chip[241]. Without a simple approach to reduce the variation of the response time, we investigated how the response time and other factors influence the sorting efficiency of the system.

In the development of Y-GECO sensors, the total flow rate was set between 10.5 and 21 μL/min for screening with a constant sheath to center stream flow ratio of 20:1, and the average linear velocity of the cells was between 5 and 10 cm/s. We first studied the sorting efficiency at 10.5 μL/min. As we observed the response time of our system varying from 2 ms to 10 ms, the average response time was 6 ms and cells traveled an average distance of 300 μm during this time. We thus placed the first detector 300 μm before the geometric sorting region, assuming no delay time required to activate the sorting at 10.5 μL/min flow rate, to investigate the other three parameters including sorting voltage, delay time and pulse width (Figure 2.7a-c).

Figure 2.7a shows the actuator can generate effective fluid displacement to shift a cell to the collection channel with a 15 V voltage trigger, when delay time was 0 and pulse width was 5 ms. We then evaluated delay time with sorting voltage set to 15 V and pulse width at 5 ms, Figure 2.7b. Without any delay time to activate the actuator, the highest sorting efficiency was obtained, because the average system response time provided the needed offset for the travel time of cells from the detector to the sorting region. With longer delay time, more cells had passed the sorting region at the time of sorting. As for pulse width, evaluated with a 0 ms delayed, 15 V pulse, the highest sorting performance was achieved when the pulse width was set to 5 ms and longer (Figure 2.7c), which is consistent with the parametric analysis discussed above. Note though, that this test does

not exam how many low intensity cells might be captured during the pulse triggered for the high fluorescence intensity cell, and longer pulse widths may lead to more low performance cells being captured. However, the following plate growth step for identifying the brightest colonies means any false positive cells captured do not influence subsequent screening studies.

As no delay time was required with the lowest flow rate, better sorting performance was not likely to be achieved with a higher flow rate. Cells travelling at a faster speed will take a shorter time to reach the sorting region when the sorter has not yet been triggered. Similarly, it is not likely to improve the sorting performance by placing the first detector closer to the sorting region. Therefore, we further investigated the sorting performance by placing the detector away from the sorting region at two locations, 600 μm and 1200 μm from the sorting region. The optimized sorting efficiency at the three detector locations with different flow rates are presented in Figure 2.7d, and the optimized parameters are listed in Table 2.2. From the results, higher sorting efficiency is not obtained as the detector moves away from the sorting region, but as expected, a delay time for the pulse was required as the distance from detector to sorting channel increased. While not improving performance, the results illustrate that a longer distance from excitation probe to cell sorting position can be used effectively, with a longer pulse delay time. This result is of value if a secondary process were to be explored, such as time of reaction of the cell with an agonist or antagonist.

It seems likely that the relatively poor sorting performance is partly attributed to the lack of a three-dimensional focusing flow. In the vertical direction, cells were not focused to the middle of the channel and so traveled at different linear velocities due to the parabolic flow profile of pressure-driven flow. A portion of cells were not in the sorting region upon sorting activation, due to the

non-uniform velocity and travel time from detector to sorting region. For example, the average linear velocity of cells is 9.6±1.0 cm/s at the flow rate of 21 μL/min and the average travel time from a detector located 1200 μm before the geometric sorting region to the center of the geometric sorting region (1250 μm for the total distance) is 13.2±1.5 ms. As we mentioned earlier, the geometric sorting region is 100 μm long, but the actual sorting region is 200 μm long. If the variation of the system response time is not considered and the delay time to activate the sorter is 13.2 ms, then 43% of the cells is out of the actual sorting region with a travel distance > 1150 μm or < 1350 μm. Table 2.3 lists the percentage of cells which are out of the actual sorting region at different distances for detection and various total flow rates. We note that there are fewer cells in the sorting region upon sorting activation as the distance between the detector and the sorting region becomes longer because longer travel time will lead to a larger variation of travel distance at a specific flow rate. When the distance from the detection point to the geometric sorting region is 300 μm, the percentage of cells out of sorting region is insignificant. To further improve the sorting efficiency, we assume that by utilizing a three dimensional focusing flow, the distribution of the linear velocity can be narrowed and more cells will be in the sorting region when the actuator is triggered.

The relatively high linear speed (> 5 cm/s) and the corresponding short time (< 4 ms) in the sorting region may significantly reduce the chance of cells being collected in the sorting channel. Even if all the cells travel at the same speed, the response time of the system is not constant and no specific choice of delay time was found to offset the varied response time. With a slower speed, a cell spends longer in the sorting region, which could increase the chance of successfully selecting a cell, because it is more likely to be in the sorting region when the system responds to activate the

actuator. Those two possible reasons for the observed ~30 % efficiency of capture upon a trigger will be verified and further discussed in chapter 3.

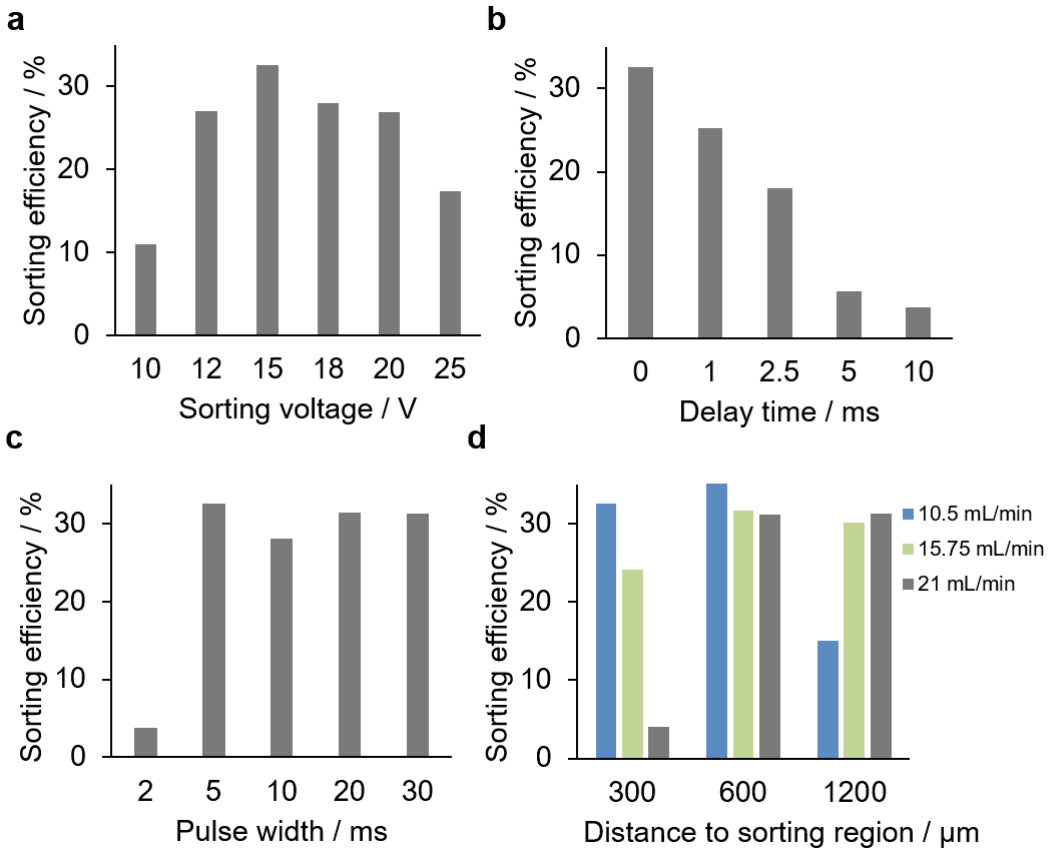

Figure 2.7 Sorting efficiency study.

(a-c) Flow rate was 10.5 µL/min and detection point was at 300 µm before the geometric sorting region. (a) Sorting voltage was varied. Delay time = 0, pulse width = 5 ms. (b) Delay time was varied. Sorting voltage = 15 V, pulse width = 5 ms. (c) Pulse width was varied. Delay time = 0, sorting voltage = 15 V. (d) Optimized sorting efficiency at different flow rates and distances to the geometric sorting region using the parameters listed in Table 2.2.

Table 2.2 Optimized parameters for sorting efficiency at different flow rates and distances between detector and geometric sorting region.

Distance to geometric sorting region / μm	Flow rate / μL/min	Sorting voltage / V	Delay time / ms	Pulse width / ms	Sorting efficiency / %
300	10.5	15	0	5	33±3
	15.75	15	0	5	24±2
	21	25	0	5	4±0.5
600	10.5	20	5	5	35±2
	15.75	20	0.5	5	32±2
	21	20	0	5	31±7
1200	10.5	20	12.5	5	15±1
	15.75	20	5	5	30±7
	21	20	2.5	5	31±3

Table 2.3 Percentage of cells out of actual sorting region upon sorting activation at different flow rates and distances between detector and geometric sorting region

Distance to geometric sorting region / μm	Flow rate / μL/min	Average travel time to the center of the actual sorting region /ms	Percentage of cells out of actual sorting region /% [1]
300	10.5	6.6±0.6	0
	15.75	4.8±0.5	2
	21	3.7±0.4	2
600	10.5	12.3±1.1	7
	15.75	8.9±0.8	11
	21	6.8±0.8	14
1200	10.5	23.6±2.1	31
	15.75	17.1±1.6	28
	21	13.2±1.5	43

[1] At the distance of 300 μm, the cells out of the actual sorting region are those traveling a distance of < 250 μm or > 450 μm during the average travel time to the center of the actual sorting region at each flow rates, based upon the variation observed in flow rates. At 600 μm and 1200 μm, the traveling distances are out of 550-750 μm and 1150-1350 μm, respectively.

2.3.3. Expression level of single colony from different variants

As the expression level of a Y-GECO variant may vary from cell to cell, a cell with a higher expression level shows a higher brightness. When a library of variants expressed in cells was screened, a variant with poor photophysical properties (extinction coefficient and quantum yield) but a high expression level in the cell may lead to a false positive being selected. To study the influence of the expression level on directed evolution by μFACS screening, we measured

fluorescence signals from three different variants discovered in the process of directed evolution. The three variants, Y-GECO0.5, Y-GECO0.7 and Y-GECO1.0, show increased *in vitro* absolute brightness (extinction coefficient×quantum yield).

During signal collection, the PMT was supplied with a 570 V voltage to obtain a high sensitivity. Sensitivity increases with supply voltage, but too high a voltage will result in signal saturation, meaning that the system cannot distinguish cells with different brightness. In our system, saturation happens when output signals are higher than 10 V. With a 570 V supply voltage, only 0.2% of cells in a colony expressing the brightest variant Y-GECO1.0 show signals over 9.5 V. As a result, 570 V was selected for the expression level measurement of the three variants to reduce the influence of signal saturation but maintain a high sensitivity for detection.

For each variant, thousands of cells from a single colony were measured and the normalized distribution of the fluorescence intensity was plotted. In Figure 2.8, a broad distribution of the brightness within a single colony is observed, but the upper range of each distribution does reflect the brightness of the variant. Along with variations of expression level, the broad distribution of the signals from a single colony is also affected by the cells traveling at different velocities in different flow streams, and the differing laser intensity across the detection zone, as discussed in Section 2.3.1. Nevertheless, cells expressing Y-GECO1.0, the final product of our directed evolution with the highest brightness, can be distinguished from cells expressing the other two variants when the capture threshold is set above 5 V, with the PMT supply set to 570 V. A 2 V threshold is set to distinguish Y-GECO0.7 and Y-GECO0.5 so that there is a higher chance to capture cells expressing Y-GECO0.7 than Y-GECO0.5 as indicated in Figure 2.8.

For directed evolution based on screening of single cells, signal heterogeneity may cause false positives as well as false negatives, restricting the efficacy of directed evolution. Cells expressing poor variants at high expression levels or excited with the highest intensity portion of the laser beam could be selected, whereas cells expressing improved variants might be eliminated because of their low expression levels or excitation in lower intensity regions. To reduce the risk of false negatives, a threshold could be set at a lower intensity, such as at 3 V instead of 5 V to help select what would otherwise be a false negative for Y-GECO1.0 in Figure 2.8. Also, more than one cell expressing the same variant may be screened given the higher throughput (> 10^6 cells/round) of the μFACS compared to a manual based search, so it is still more likely to select an improved variant. To address the problem of false positives, a subsequent manual on-plate screening was conducted after the on-chip screening to enhance the performance of the directed evolution. The selected cells, which will have some false positives from the μFACS, were cultured on agar plates. The colonies were then manually picked based on brightness for protein extraction, followed by screening according to both brightness and Ca^{2+}-dependent fluorescence change using platereader with high reliability. False positive derived cell colonies were easily identified and so were not selected for subsequent directed evolution cycles. Overall, the data in Figure 2.8 support the ability of the cell sorter to identify and isolate the brightest strains of fluorophore, independent of the factors that can reduce accuracy, such as flow rate variation, cell position in the flow stream, and FP expression heterogeneity.

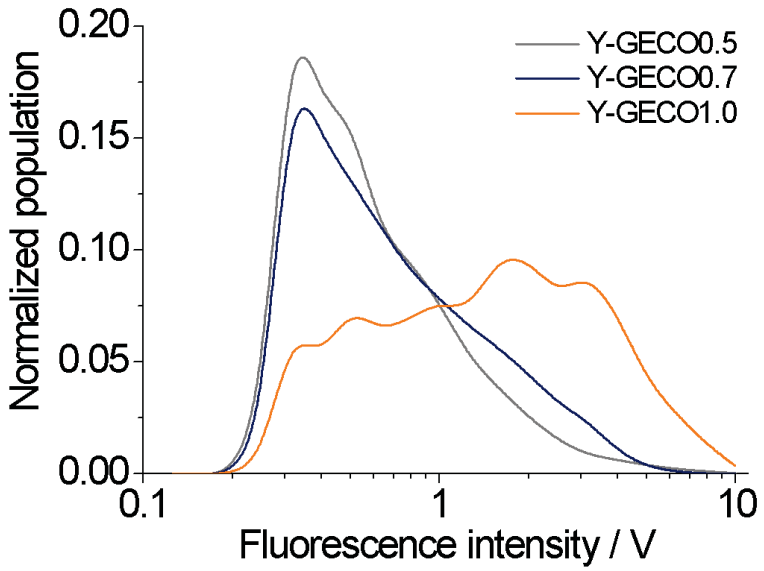

Figure 2.8 Normalized distributions of fluorescence signals obtained in μFACS from single colonies of three variants of Y-GECO. Note the highest intensity cells at low population levels are of the greatest interest for selective capture. Y-GECO1.0 is the brightest variant produced by directed evolution, while the other two varieties are less bright, but still strong fluorophores produced by directed evolution.

2.4. Conclusions

In this chapter, characterization studies were performed to evaluate the μFACS system for directed evolution of FP-based Ca^{2+} sensors. The sorting efficiency was studied in regard to different flow rates. Factors that influence the sorting performance were optimized, such as distance of the detector to the sorting region, the voltage applied to the actuator, pulse width, and delay time for triggering the actuator. The optimized sorting efficiency was less than 40% and possible reasons were discussed. With a throughput of up to 10^6 cells, over 3×10^5 cells can be screened and are likely to be sorted, significantly higher than conventional manual screening on agar plates (~ 10^4

cells). The expression distribution of single colonies from three different variants were examined, though this distribution was convoluted with any velocity and fluorescence excitation intensity differences for each cell in the detector. Despite the broad distribution of each variant, which may cause false positives and negatives, the highest fluorescence intensity of each distribution generally reflects the absolute brightness of the purified proteins. With a high throughput, a lower threshold for sorting and a subsequent step of colony-based screening, false negatives and positives from μFACS are not likely to cause serious problems in the directed evolution. Our μFACS-aided brightness based screening, with high throughput, provides a fast and effective approach to engineer FP-based Ca^{2+} sensors with high brightness.

Chapter 3. Microfluidic cell sorter for multiparameter screening in directed evolution

3.1 Introduction

Microfluidic activated cell sorters (μFACS) have been applied to perform directed evolution of functional proteins. High throughput and automated screening by microfluidic systems can significantly speed up the selection process, enlarge the library size for screening and reduce the workload. Droplet based microfluidic platforms are used for directed evolution of enzymes to develop variants demonstrating better catalytic performance with reaction volume and time being well-controlled[12,15,40,60,61,63]. A single-phase flow cell sorter is often selected when reaction is easily realized without droplets, an example of which is screening fluorescent protein (FP) based sensors towards improved photophysical and biochemical properties[65–68,70,71]. Our group demonstrated a one-phase flow, cell sorting system to select sensors expressed in *E. coli* cells showing higher brightness, with 100-fold increased throughput (> 150 cells/s and 10^6 cells/round) compared to conventional manual screening on agar plates[71]. However, that μFACS system selected for indicators based only on a single-point measurement of brightness. A single-point measurement cannot provide information on the magnitude of the fluorescent response, which is determined by the difference between the brightness in the Ca^{2+}-bound and Ca^{2+}-free states.

The Palmer group developed a μFACS platform with multiple fluorescence detection beams and optical tweezers for cell sorting, and applied the established cell sorting system to screening libraries of mCherry variants to improve both its photostability and brightness through directed evolution[68]. The two-factor screening led to beneficial mutants with increased photostability, but

unfortunately decreased brightness. Moreover, exposure to the optical tweezer resulted in a decrease in cell viability to 80% after 24 hours. The same group devised a different droplet-based microfluidic cell sorter (using dielectrophoretic sorting) at a throughput of ~7 cells/s using two beams to evaluate analyte-induced fluorescence change of FP-based sensors[70]. A mixture of two known Zn^{2+} sensors, were sorted to enrich one sensor with >90% purity of the target. This microfluidic cell sorter was not utilized for screening libraries of variants in a course of directed evolution of FP-based sensors.

Further developing our previous system with the concept of multi-parameter screening, we introduce a single-phase flow μFACS system with two-point detection for directed evolution of an FP-based Ca^{2+} sensor. Two fluorescence microscopes are utilized to determine the magnitude of Ca^{2+}-induced fluorescence change, along with the overall brightness of the sensor. In the absence of oil in water droplets for precise flow control, a 3D focusing flow was configured for better spatial control of cells and signal pair-matching. A piezoelectric actuator for sorting is integrated on-chip, which causes little damage to cells, as previously reported[36]. The μFACS screens both the brightness and Ca^{2+}-dependent fluorescence change of the sensor at a throughput of 10 cells/sec and selects for the top 1% variants. This microfluidic-based platform greatly improves the selectivity of directed evolution compared to the microfluidic FACS with a single point detection, leading to variants of a Ca^{2+} sensor with increased brightness and greater Ca^{2+}-dependent fluorescence change after two rounds of directed evolution.

3.2 Methods

3.2.1 Device fabrication.

A PDMS-based microfluidic device was fabricated by the standard soft lithography method, as we described in Section 2.2.2.

3.2.2 Two detector operation.

To calibrate signals from two detectors, *E. coli* cells expressing Y-GECO1f were suspended in buffers containing EGTA and tested in the μFACS, with EGTA for the sheath flow also. The position of the two detectors, the laser intensity and the PMT voltage were then adjusted to minimize the difference of the signals from each individual cell at the two detectors. After calibration, a diluted cell suspension was used to determine the average Δt: ~ 500 cells were collected and matched to determine the transit time between detectors, then used for subsequent cell pair-matching.

To determine sorting efficiency, one detector was placed before the sorting junction at the standard detector 2 location, and another was placed downstream in the collection channel (Figure 3.4a).

3.2.3 Preparation of Y-GECO-expressing *E. coli* cells for system characterization.

The preparation of Y-GECO1f-expressing *E. coli* cells for μFACS has been described in Section 2.2.3.

3.2.4 Directed evolution of Y-GECO1f using μFACS.

The process of directed evolution based on the μFACS is illustrated in Figure 3.1. First, a gene library of Y-GECO1f was generated by error-prone PCR and ligated to pTorPE plasmid vectors[120] for periplasmic expression. Competent *E. coli* DH10B cells were transformed with a gene library encoding Y-GECO1f and plated on agar for overnight incubation at 37 °C. TBS buffer with 0.2 mM $CaCl_2$, 1% glycerol, 100 μg/mL ampicillin and 0.002% arabinose was used to wash colonies on the agar plate for cell collection. The cell suspension was diluted to desired cell densities for on chip screening. The sorted cells from the μFACS were then plated on agar for overnight culture. Since only brightness could be acquired by colony-based screening, colonies showing medium to high brightness of fluorescence were picked for liquid cultures and protein extractions by B-PER. The extracted proteins were tested in a microplate reader for both brightness and fluorescence change upon Ca^{2+} binding. False positives from μFACS screening were thus eliminated. The plasmids of the superior mutants were collected as templates for the next round of evolution.

To compare the efficacy of directed evolution by μFACS with the two-point detection system, we also performed parallel brightness-based screening using our previously established platform at the same flow rate 5.25 μL/min. The throughput of the one detector screening was over 50 cells/s and 5×10^5 cells could be screened in 3 hours, significantly higher than the two detector system. While the throughput is lower than our previous work due to the lower flow rate, the 85% capture efficiency, which will be discussed in 3.3.3, compared to ~40% with our previous 2D μFACS used for brightness based screening in directed evolution of Y-GECO1f and 1m greatly compensated, so the number of cells evaluated per hour was similar. Cells with the top 0.1% brightness were sorted, followed by a manual colony-based screening to remove false positive cells. After each

round, the beneficial variants from both platforms were pooled as templates for next round of screening, to reset the method comparison with each round.

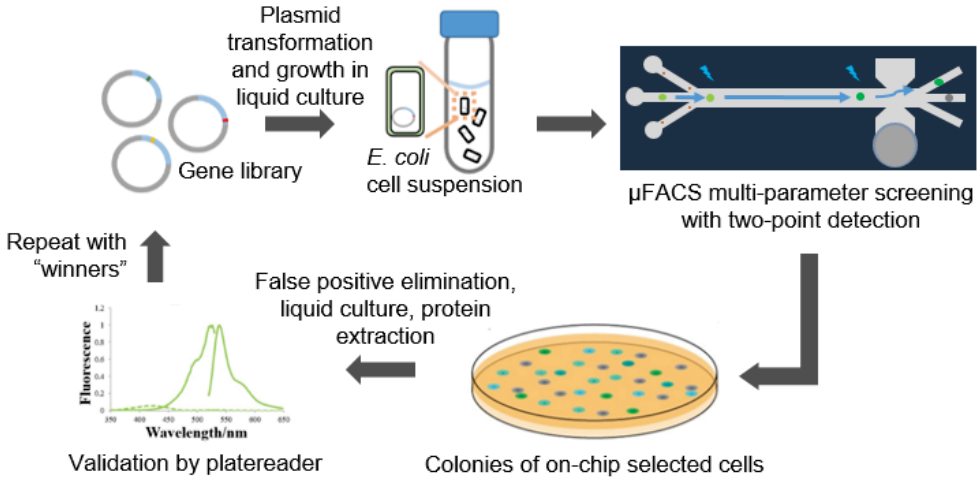

Figure 3.1 Directed evolution process of Y-GECO genetically encoded Ca^{2+} indicators, aided by μFACS. Overview of the iterative process of directed evolution used in this work.

3.2.5 Purification and *in vitro* characterization of Y-GECO proteins.

For purification of Y-GECO variants, electrocompetent *E. coli* DH10B cells were transfected with pTorPE plasmids encoding the proteins, then cultured overnight culture at 37 C on agar plates containing LB/ampicillin (200 μg/mL). Single colonies were then picked and cultured overnight in 4 mL LB/ampicillin (200 μg/mL) liquid at 37 ℃ with shaking at 250 rpm. 1 mL liquid bacteria suspension was added to 1 L TB rich medium (0.002% wt/vol Arabinose) for culture at room temperature and 250 rpm shaking for two days. Bacteria, collected by centrifugation and suspended in 30 mM TBS buffer, were lysed by French press. Lysed cell pellets were separated from dissolved proteins by centrifugation. Ni-NTA affinity chromatography was used to extract and purify the proteins, followed by exchange of buffer to 10 mM MOPS, 100 mM KCl (pH 7.2).

A DU-800 UV-vis spectrophotometer (Beckman) and Safire2 plate reader were used to measure the absorption, excitation and emission spectra of the Ca^{2+} indicators, correspondingly. The ratiometric response to Ca^{2+} of Y-GECO is defined as $(R_{max} - R_{min}) / R_{min}$. R = (I with 526 nm excitation) / (I with 416 nm excitation), where I is the fluorescence intensity at 550 nm. The intensiometric response to Ca^{2+} of Y-GECO is defined as $(I_{max} - I_{min}) / I_{min}$. The absorption spectra was determined in Ca^{2+} buffer (30 mM MOPs, 100 mM KCl and 10 mM Ca^{2+} at pH 7.20) and Ca^{2+}-free buffer (30 mM MOPs, 100 mM KCl and 10 mM EGTA at pH 7.20). By comparing the absorption peak of alkaline denatured Y-GECO with the peak of denatured mPapaya, the concentration of the sensor was determined, assuming the extinction coefficients of denatured mPapaya and denatured Y-GECO are the same. The concentration of mPapaya was calculated by dividing its absorption peak in non-denatured condition by its known extinction coefficient. The extinction coefficient of Y-GECO was then calculated by its absorption peak in non-denatured condition based on the concentration.

FP mT-Sapphire and mCitrine were used as standards to determine quantum yield of Y-GECO sensors for fluorescence with excitation at 414 nm and 524 nm, respectively. The total fluorescence of each FP was obtained by integrating the whole emission peak. The integrated fluorescence vs. absorbance of each FP was plotted and its slope (S) was used to calculate the quantum yield:

$$\Phi_{Y\text{-}GECO} = \Phi_{standard} \times (S_{Y\text{-}GECO} / S_{standard}) \quad (3.1)$$

The pK_a of the sensors in Ca^{2+}-free or Ca^{2+}-bound was measured by pH titration. The titration buffers were 50 mM Tris, 50 mM citrate,50 mM glycine, 100 mM NaCl and 10 mM either Ca^{2+} or EGTA. A series of buffers with pH ranging 4.5 to 11.5 were generated by pH adjustment with HCl or NaOH solution. Solutions of purified Y-GECO sensors was diluted into the pH titration buffers

and the fluorescence response of each buffer was measured. The ratiometric response of the sensors vs. pH value was plotted and fit to a sigmoidal curve for pK_a determination.

The buffers to measure the dissociation constant, K_d', were prepared by mixing Ca^{2+} buffer (30 mM MOPS, 100 mM KCl, 10 mM EGTA, 10 mM $CaCl_2$ and pH 7.2) and Ca^{2+}-free buffer (30 mM MOPS, 100 mM KCl, 10 mM EGTA and pH 7.2) at different ratios. The free [Ca^{2+}] concentration of the prepared buffers at 25 °C ranges from 0 nM to 3900 nM. With purified Y-GECO proteins diluted into those buffers, the ratiometric fluorescence responses of Y-GECO sensors (R) was recorded and plotted versus free [Ca^{2+}] concentration, then fit to the Hill equation for K_d' determination as below:

$$R = R_{max} + (R_{min} - R_{max}) \frac{[Ca^{2+}]^n}{K_D'^n + [Ca^{2+}]^n} \quad (3.2)$$

3.2.6 Kinetics of Ca^{2+} association and dissociation fluorescence change of Y-GECO.

Stopped-flow spectroscopy was used to evaluate reaction kinetics of FP with Ca^{2+}, using an excitation wavelength of 520 nm, a 13.95 nm bandwidth, and an emission wavelength of 540 nm with a 37 nm bandwidth. To measure the kinetics of Ca^{2+} association and dissociation fluorescence change of Y-GECO in cells, *E. coli* cells expressing Y-GECO variants were first suspended in TBS buffer containing 0.2 mM $CaCl_2$ or 0.2 mM EGTA, followed by rapid mixing (1:1) with TBS buffer containing 20 mM EGTA or 20 mM $CaCl_2$.

To measure the Ca^{2+} dissociation rate constant, k_{off}, of Y-GECO, purified Y-GECO indicator was first diluted in a solution containing 30 mM MOPs, 0.2 mM $CaCl_2$ and 100 mM KCl, then followed by rapidly mixing (1:1) with another buffer containing 30 mM MOPs, 20 mM EGTA and 100 mM

KCl. Fluorescence signals were captured using ProData SX software. The fluorescence intensity vs. time was collected, plotted and fit to a single exponential curve, giving k_{off}.

3.2.7 Construction of plasmids for mammalian cell expression.

To express Y-GECO indicators in HeLa cells and dissociated neurons for *ex vivo* characterizations, the Y-GECO gene in pBAD vector, used for expression in *E. coli* cells, was amplified by PCR with the primers FW_BamHI_Kozak_6His and RV_CaM_stop_EcoRI, followed by gel purification of the PCR products. The purified gene was then digested with the restriction enzymes BamHI and EcoRI, purified and ligated into a modified pcDNA3 plasmid vectors which have been digested with the same enzymes and purified by gel. The ligation products, the plasmids for mammalian expression of Y-GECO indicators, were transformed into electrocompetent *E. coli* DH10B cells which were then plated on an agar plate containing 1× ampicillin for overnight culture at 37 °C. On the following day, individual colonies were picked for 12 h liquid culture in 4 mL B/ampicillin, shaken at 250 rpm. The cultured cells were then isolated and the plasmids were purified for mammalian cell transfection and expression.

3.2.8 Hela cell culture and imaging

Hela cells (40%-60% confluent) on 35 mm glass bottom dishes were transfected with 1 μg plasmid DNA and 2 μL Turbofect (Thermo Scientific) based on the instructions from the manufacturers. The media was exchanged to Dulbecco's modified Eagle's medium (DMEM) with 10% fetal bovine serum (FBS) after two hours incubation. The cells were then incubated in a CO2 incubator at 37 °C for 24 hours. Immediately before imaging, cells were washed with Hank's balanced salt solution (HBSS) twice, then 1 mL 20 mM HEPES buffered HBSS was added.

Wide-field imaging of cells was performed on an epifluorescence inverted microscope (Eclipse Ti-E, Nikon) equipped with a digital CCD camera (QuantEM 512SC). The microscope and camera were controlled using NIS-Elements Advanced Research software. Cells were imaged with a 20× air objective lens (NA 0.8). The cells were illuminated by a 100 W mercury arc lamp and a 25% neutral density filter was used to reduce the intensity of the light. To record the short Stokes shift fluorescence, we used a filter set of 480/40 nm (excitation), 505 (dichroic) nm and 535/40 nm (emission).

3.2.9 Dissociated rat hippocampal neurons preparation and imaging.

Dissociated rat hippocampal cells were from embryonic day 18 Sprague-Dwaley rats and stored in Hibernate® EB Complete Media. Those cells were purchased from BrainBits LLC and cultured for growing on a 35-mm dish with glass bottom containing NbActiv4 (BrainBits LLC) with 2% fetal bovine serum, 50 units/mL penicillin-G potassium salt, and 50 μg/mL streptomycin sulfate. Fresh media was used to replace half of the culturing media on DIV-4, which the fourth day *in vitro*. Transfection of plasmids for Y-GECO expression was performed on DIV-7 by using Lipofectamine 2000 or GenJet. The dissociated neurons were ready for imaging 2-4 days after the transfection was finished. Y-GECO indicators expressed in dissociated neurons were similarly imaged as their expression in HeLa cells mentioned above. A 60× oil objective lens was used for higher amplification and a 12.5 % neutral density filter was used to reduce the excitation intensity. Neurons were exposed to excitation light for continuous 1 min. Only short-Stokes fluorescence was recorded by using the filter set 480/40 nm (excitation), 505 (dichroic) nm and 535/40 nm (emission). Images were captured every 0.06 s.

3.3 Results and discussion

3.3.1 Design of a μFACS device with a two-point detection system.

To enhance the screening of libraries of Ca^{2+} indicator variants expressed in *Escherichia coli*, a multiple facet screening method is advantageous. We redesigned a previous μFACS[6] system based on a polydimethylsiloxane (PDMS) microchip, adding a two-point detection system to measure both brightness and fluorescence change upon reaction with Ca^{2+} (Figure 3.2a), incorporation of real time signal processing for selection of variants with the highest performance in both categories, and 3-D sheath flow to reduce dispersion in cell velocities (Figure 3.2b). The design used two vertical sheath flow channels with two horizontal sheath channels, along with the sample inlet channels, with three outlet channels. Syringe pumps were used to deliver buffers and cell suspension. The combination of two horizontal and two vertical channels provided a 3D sheath flow system around the middle inlet stream. The middle stream of Ca^{2+} buffer with *E. coli* cells expressing FP Ca^{2+} indicators, was sheathed by the two vertical sheath flow channels loaded with Ca^{2+} buffer (Figure 3.2b), while the two side inlet channels contained the Ca^{2+}-chelator EGTA. The EGTA diffused to the center of the stream, chelating Ca^{2+} to decrease the concentration of free Ca^{2+} in the 5 cm mixing channel and induce Ca^{2+} release from the FP indicators expressed in the cells.

A piezoelectric actuator was integrated on chip for cell sorting, deforming when a voltage was applied to deflect desired cells to a collection channel. An epi-fluorescent confocal microscope with photomultiplier tubes (PMT) as detector was located at the initiation of Ca^{2+} concentration change, with another 5 cm downstream (Figure 3.2a), to allow screening for both brightness and Ca^{2+}-dependent fluorescence change. The laser spot was shaped with spherical and cylindrical

lenses to give a beam ~300 μm long perpendicular to the direction of flow in the channel and ~10 μm wide along the flow axis (Figure 3.3). Using the equations developed by Lubbeck *et al*[65], the TEM00 beam of the laser is estimated to vary ~0.3 % in intensity across the 7.14 μm wide focused central flow channel loaded with cells. Even if the beam center is not quite optimal, for example shifted by a few tens of μm, the variation in intensity across the central cell channel is no more than 1%. This low variation ensures all cells see essentially the same excitation intensity.

Fluorescence signals were processed in real time, determining the fluorescence of nominally the same cell at each detector, as matched using the average travel time between detectors, $\Delta t = t_2 - t_1$ (where t_1 and t_2 are the times when a single cell is detected at detectors 1 and 2, respectively). The ratio of fluorescence intensity at each detector, F_2/F_1 and intensity at detector 2 downstream, F_2, were calculated and the combined term $F_2 \times (F_2/F_1)$ was used as the criteria for sorting.

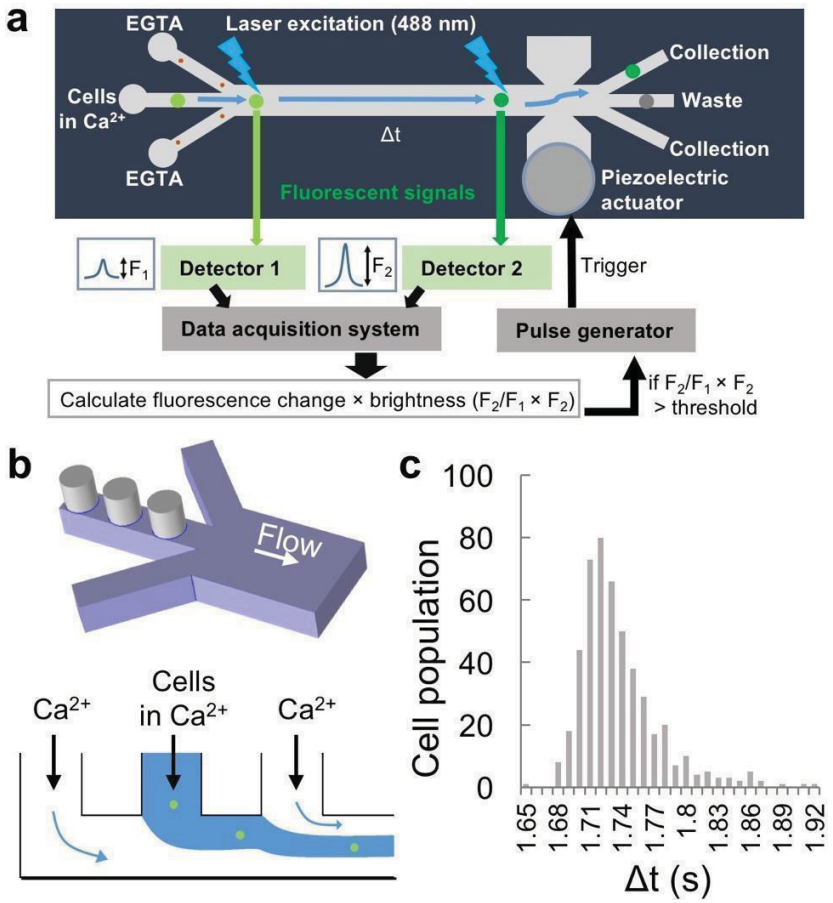

Figure 3.2 A μFACS system with two-point detection and 3D focusing to assist directed evolution of the Y-GECO Ca^{2+} indicator.

(a) Schematic representation of the μFACS system. (b) Schematic representation of 3D focusing flow on chip. Top: Sample inlets for 3D focusing. Bottom: Side view of the three input holes in the middle inlet channel. The first and third holes are vertical sheath flow with only buffers and the second hole introduces cell suspension to be focused. (c) Distribution of Δt with 3D focusing flow at the flow rate of 5.25 μL/min.

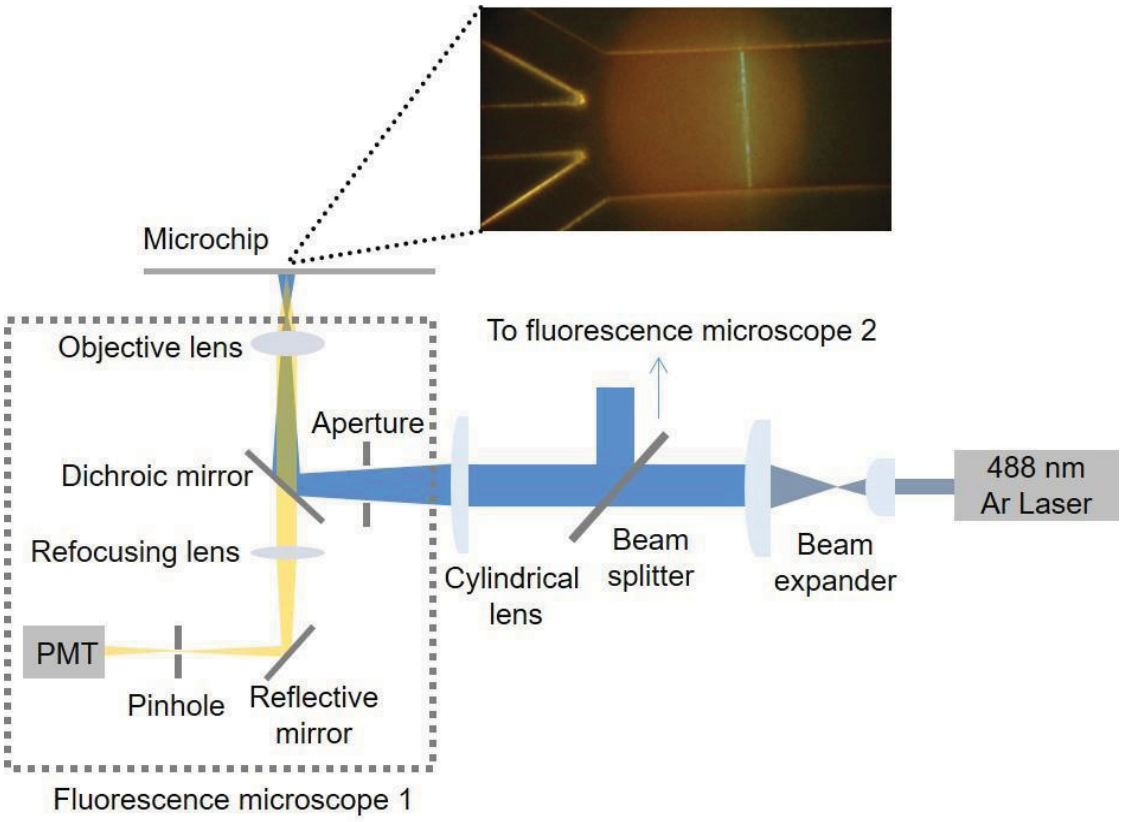

Figure 3.3 Illustration of the optical setup for detection system. Fluorescence microscope 2 is same with fluorescence microscope 1 and not represented in the figure. Also shown is a microscopic image of the linear focused beam on the chip near the inlet channels.

3.3.2 3D sheath flow system.

To evaluate the effect of the 3D sheath flow system (Figure 3.2b) on the standard deviation of Δt, a diluted suspension of *E. coli* cells expressing Y-GECO1f was analyzed in the μFACS. For 2D focusing with the two side sheath flows at 2.5 μL/min and the cell stream at 0.25 μL/min (total = 5.25 μL/min), the average Δt was 1.86 ± 0.33 s. This large standard deviation results in substantial uncertainty in the arrival time at the collection channel, and was a large contributor to 70% collection efficiency of the 2D design. For 3D focusing, performance was evaluated with the flow

rates of the horizontal sheaths at 2.5 μL/min each, both vertical sheaths at 0.1 μL/min and the central cell flow at 0.05 μL/min (total = 5.25 μL/min). Analysis of about 500 cells gave a Δt of 1.73 ± 0.04 s (Figure 3.2c). The much smaller standard deviation greatly improves both the throughput and sorting efficiency as discussed below, and confirms flow stream velocity differences as the major source of velocity dispersion in the 2D sheath flow design. Under optimized conditions (see below), a collection efficiency of ~85% could be realized with this 3D design.

3.3.3 Optimizing sorting efficiency.

To optimize the system performance, we positioned one detector 300 μm before the sorting junction and the second detector inside the collection channel (Figure 3.4a). Using this arrangement, we optimized the delay time to trigger the actuator (Figure 3.4b), the amplitude of the piezoelectric actuator voltage (Figure 3.4c), and the width of the pulse applied to the actuator (Figure 3.4d). A delay time following the trigger is required to offset the travel time of a cell from the detector to the sorting junction, taking into account any inherent trigger to actuator delay due to hardware or software. The amplitude of the voltage applied to the actuator determines the extent of its bending and the volume of liquid being deflected. These optimization experiments revealed that the sorting efficiency was maximized at delay times of 0 to 5 ms, actuator voltages of 15 V, and pulse widths of 10 ms. Notably, the response time of our data acquisition and software processing system varies from 4 to 15 ms, accounting for the nearly equal results for pulse delay times of 0-5 ms. External triggering hardware, and higher quality data acquisition boards have been shown to reduce this instrumental delay to a few μs[241], but were not employed in this work.

The maximal sorting efficiency with 3D focusing at 2.89 cm/s is 85%, while for the same velocity in a 2D configuration it was 70% in this study. Both values are far higher than the <40% collection efficiency in our previous work with a 2D device and single point, brightness-based screening at a velocity of ~ 5 cm/s. The slower linear velocity and longer time the cell spent in the sorting junction accounts for the improved sorting efficiency, compensating for variance in the instrument delay time t_r.

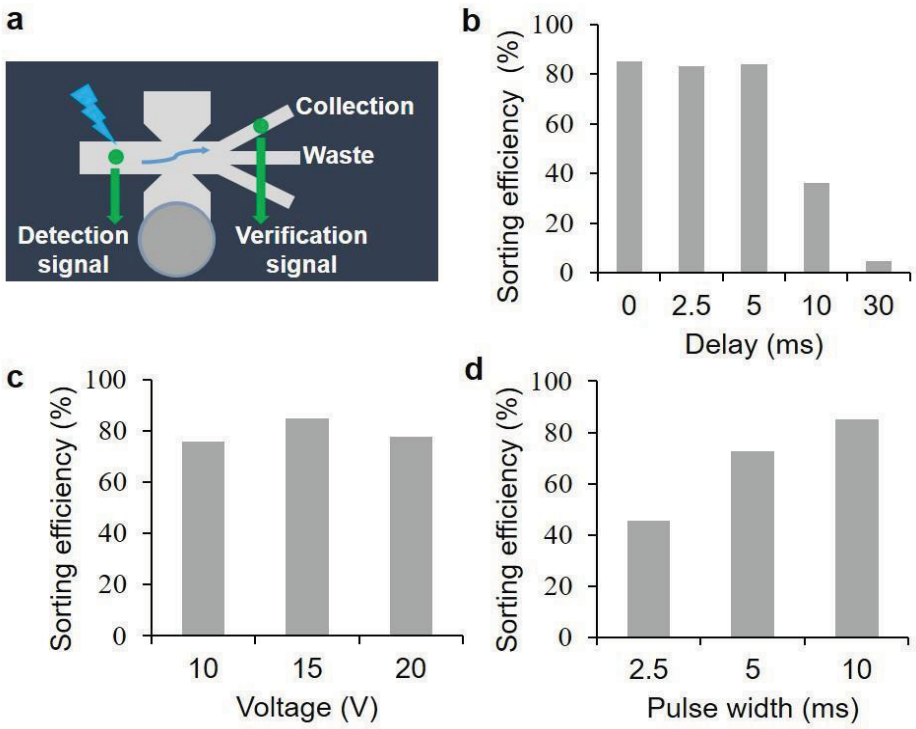

Figure 3.4 Optimization of pulse delay, voltage, and width for actuator activation.

(a) Schematic representation of detection setup for measurement of sorting efficiency. Sorting efficiency was optimized at a linear velocity 2.89 cm/s. (b) Sorting efficiency at different delay times to trigger the sorter. The voltage applied to the sorter is 15 V and the pulse width is 10 ms. (c) Sorting efficiency with different voltages applied to the sorter. The delay time is 0 and the pulse width is 10 ms. (d) Sorting efficiency at different pulse widths. The voltage applied to the sorter is 15 V and the delay time is 0.

3.3.4 Consideration of Ca^{2+} indicator kinetics.

The kinetics of fluorescence changes associated with Y-GECO1f Ca^{2+}-dissociation and Ca^{2+}-association in the periplasm of *E. coli* cells was measured by stopped-flow spectroscopy (Figure 3.5). The duration of the fluorescence change associated with Ca^{2+} association is < 0.05 s, and the time required for Ca^{2+} dissociation is ~2 s. Accordingly, the ~1.73 s from detector 1 to 2 along the 5 cm path of the μFACS (at a linear velocity of 2.89 cm/s and total flow rate of 5.25 μL/min) is well suited to observing changes in the kinetics of Ca^{2+}-dissociation from the indicator. The time required to travel from the sheath flow junction to detector 1 located 150 μm downstream is ~5 ms, while the time required for 20 mM EGTA to diffuse from the side sheath flow streams to reach 6 mM EGTA at the center of the channel is < 10 ms. As both of these times are much shorter than the ~2 s required for the indicator to change its fluorescent state, the signal measured at detector 1 will correspond to the Ca^{2+} bound state of the indicator. We note that by selecting the dissociation reaction as the screening test slower dissociation rates will be screened against, which is useful as more rapid rates are desirable for monitoring intracellular Ca changes.

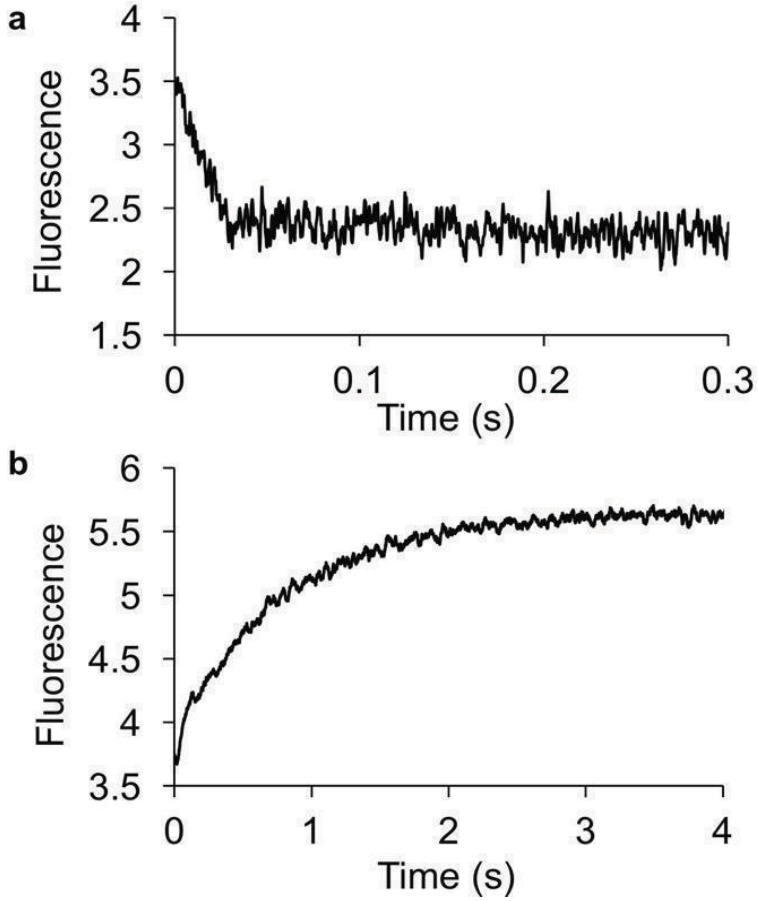

Figure 3.5 Ca^{2+} association and dissociation kinetics of Y-GECO1f in intact *E. coli* cells. (a) Fluorescence changes versus time for Ca^{2+}-association. (b) Fluorescence change versus time for Ca^{2+}-dissociation.

3.3.5 On-chip monitoring the Ca^{2+}-dissociation fluorescence change

Monitoring of the fluorescence of the FP is illustrated in Figure 3.6. Plots for detector 2 are shifted by the travel time, Δt, to make visible alignment of pair matched cells clearer. In Figure 3.6a, EGTA was added, so the signals collected at detector 2 demonstrate a significant increase compared to the signal for the pair matched cell at detector 1. In Figure 3.6b, no EGTA was added to induce free [Ca^{2+}] change, providing a measure of the repeatability of the two detectors for pair

matched cells. The results show EGTA successfully diffused from the sheath flow to the center and changed the free [Ca^{2+}] as well as the fluorescent signals of the FP Ca^{2+} sensors.

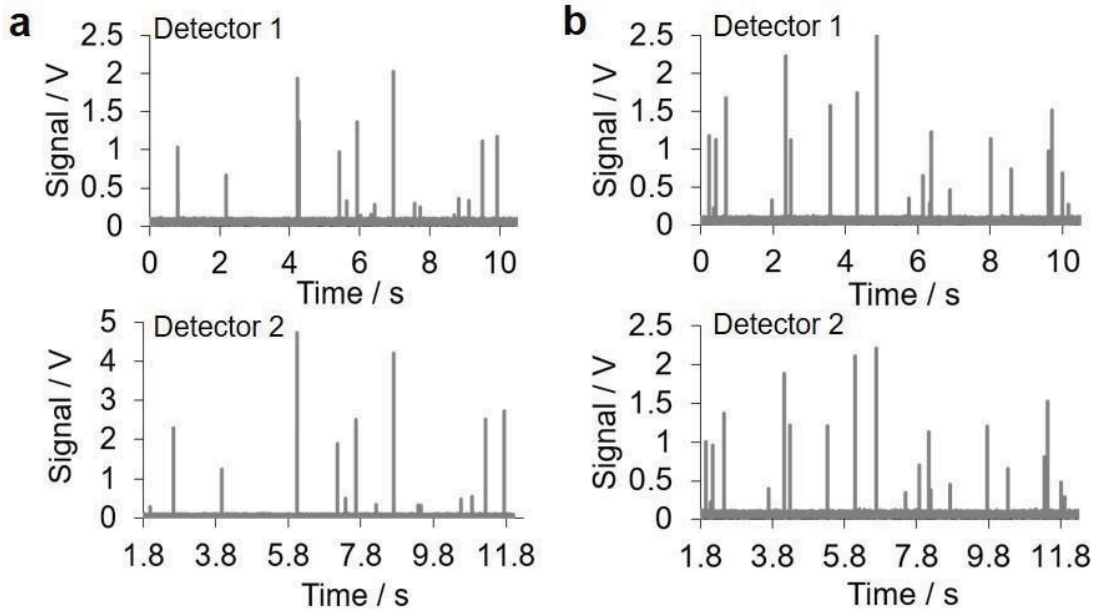

Figure 3.6 Monitoring of the fluorescence of single cells expressing Y-GECO1f, with (a) or without (b) changes in free Ca^{2+} concentration.

(a) Traces from detector 1 (upper) and detector 2 (lower) two detectors when EGTA was introduced via the horizontal sheath flow. The trace for detector 2 is shifted by the travel time, Δt, to facilitate visual alignment of pair matched cells. Signals collected at detector 2 demonstrate are substantially increased compared to the signal for the pair matched cell at detector 1. (b) As in (a) without EGTA added to introduce a change in the free Ca^{2+} concentration. Signals collected for the same cell at both detectors are of similar intensity. These results demonstrate that EGTA successfully diffused from the horizontal sheath flow to the center and changed both the extra- and intracellular Ca^{2+} concentration.

3.3.6 Pair-matching and throughput of the µFACS.

Pair-matching is the process by which a cell detected at detector 2 (at time t_2) is matched with the cell detected at detector 1 (at time $t_2 - \Delta t$), starting from the cell after the last matched cell. Cell sorting requires real time pair-matching, and the parameters that govern errors in matching control the achievable throughput and performance of a two-measurement cell sorter. The detection of a cell at detector 2 must be correctly matched to detection of the same cell at detector 1. As Δt varies slightly for individual cells, a tolerance time window ($\Delta t \pm t_{tol}$) is required. A primary source of pair-mismatch is cells with travel times outside the tolerance time window. With 3D focusing, and a standard deviation of 0.04 s at 5.25 µL/min, 3% of cells will lie outside a window of 1.73 ± 0.1 s, leading either to failure to sort the cell or mismatch to the wrong cell if it lies within the ± 0.1 s time window. At a throughput of 5 cells/s, 53% of cell to cell distances are within 0.2 s, causing a chance of mismatch if they are following a mismatched cell, when selecting a ± 0.1 s tolerance (Table 3.1). The first cell following a mismatched cell contributes to the total chance of mismatch with 53% × 3% = 1.6%. If a mismatch is made it may then propagate into subsequent linked mismatches, described by $3\% \times 53\%^N$ for the N^{th} cell in a sequence. The total chance of mismatch following an error is the sum of each possibility, which is < 7% for a ± 0.1 s tolerance. For a throughput of 10 cells/s or 20 cells/s, the total chance of propagating a mismatch is < 15% and > 50%, respectively.

By increasing the tolerance time window to 1.73 ± 0.15 s, it is less likely that cells fall out of the matching time window (< 1%). However, cell density then becomes a greater source of mismatch with the longer tolerance time, with 90% of adjacent cells closer than 0.3 s at a throughput of 10 cells/s. Mismatch propagation under these conditions is < 10%, while for 5 cells/s it is ~2%, and for 20 cells/s it becomes unreasonably high. Despite the mismatch propagation at 10 cells/s (i.e.,

36,000 cells/h), the higher throughput enables screening of twice as many variants in a given time period and increases the chance of finding rare, superior variants. As the subsequent manual screening step will eliminate false positives caused by mismatch, the higher throughput choice evaluating 10^5 cells in 3 hours is the better one.

Another factor that could potentially limit the throughput is the risk of co-sorting cells in the sorting junction. With a linear velocity of 2.89 cm/s, a cell spends ~7 ms in the sorting region (100 μm geometrically, but the actuator captures across a 200 μm range). At a throughput of 10 cells/s, cells are 100 ms apart on average and so co-sorting of cells is unlikely. Again, the subsequent manual screening step can eliminate false positives caused by co-sorting (Figure 3.1).

Table 3.1 Distribution of the cell-to-cell time difference at different throughput at the flow rate of 5.25 μL/min

Throughput (cells/s)	Percentage of cells at different cell-to cell time difference					Total number of cells
	< 0.05 s	< 0.1 s	< 0.2 s	< 0.3 s	< 0.5 s	
3	6%	15%	31%	46%	61%	2144
5	13%	31%	53%	68%	84%	2143
10	27%	51%	77%	90%	97%	2051
20	59%	86%	97%	99%	100%	2149

3.3.7 Directed evolution of Y-GECO1f based on brightness and Ca^{2+}-dissociation fluorescence change.

Using the optimized conditions discussed above, the μFACS system enabled single cells to be reliably monitored (Figure 3.6a,b) and sorted on the basis of both fluorescence brightness and their Ca^{2+}-dependent change in fluorescence. Libraries of Y-GECO1f were generated by error-prone PCR and expressed in *E. coli* using a previously reported plasmid that includes a periplasmic export sequence[120], then were sorted using the μFACS system. The top variants from each round of sorting were pooled and the corresponding Y-GECO genes used as the template for the next round of library creation and screening. In each round, about 30 colonies were picked based on their brightness during the manual screening step, and further tested for brightness (product of extinction coefficient and quantum yield) and fluorescence change with a platereader.

The most promising variant after the two rounds of screening had three mutations (Table 3.2) relative to Y-GECO1f and was designated Y-GECO2f. Further rounds of screening did not lead to the discovery of further improved variants. *In vitro* characterization revealed that Y-GECO2f exhibits a 26% increase in brightness and greater than 300% larger Ca^{2+}-dependent fluorescence change relative to Y-GECO1f (Table 3.3) while retaining a similar spectral profile (Figure 3.7a). Y-GECO2f retained a similar Ca^{2+} affinity and slightly slower k_{off} than Y-GECO1f (Table 3.4).

The resulting Y-GECO2f variant exhibits a large improvement in fluorescence change which is primarily attributed to the shift of chromophore pK_a, in Ca^{2+} bound state, from 8.5 to 9.1. A higher pK_a in the Ca^{2+} bound state means that more of the chromophore is in the non-fluorescent protonated form at physiological pH, and the fluorescence is thereby diminished to a greater degree. Due to its relatively close proximity to the chromophore, we speculate that the T30S mutation is

the key mutation responsible for the shift in pK_a. An analogous E30S mutation was discovered during the directed evolution of the R-GECO1 red fluorescent Ca^{2+} indicator[120]. Efforts to screen other residues at position 30 did not lead to the identification of further improved variants.

To compare the performance of our two detector, two parameter μFACS system with that of a one detector, brightness-based μFACS system, directed evolution was performed in parallel using the older system. As shown in Figure 3.7b, the two-point, two parameter system enabled identification of Y-GECO variants with higher brightness and fluorescence change, compared to the single detector system which screened for brightness alone. The top sorted variants from the two-point screening system exhibited an average of 35% better performance than those from the older system in the first round and 55% better in the second round. The best selected variant by two-parameter screening was 110% better than the best variant from the one-paramater study.

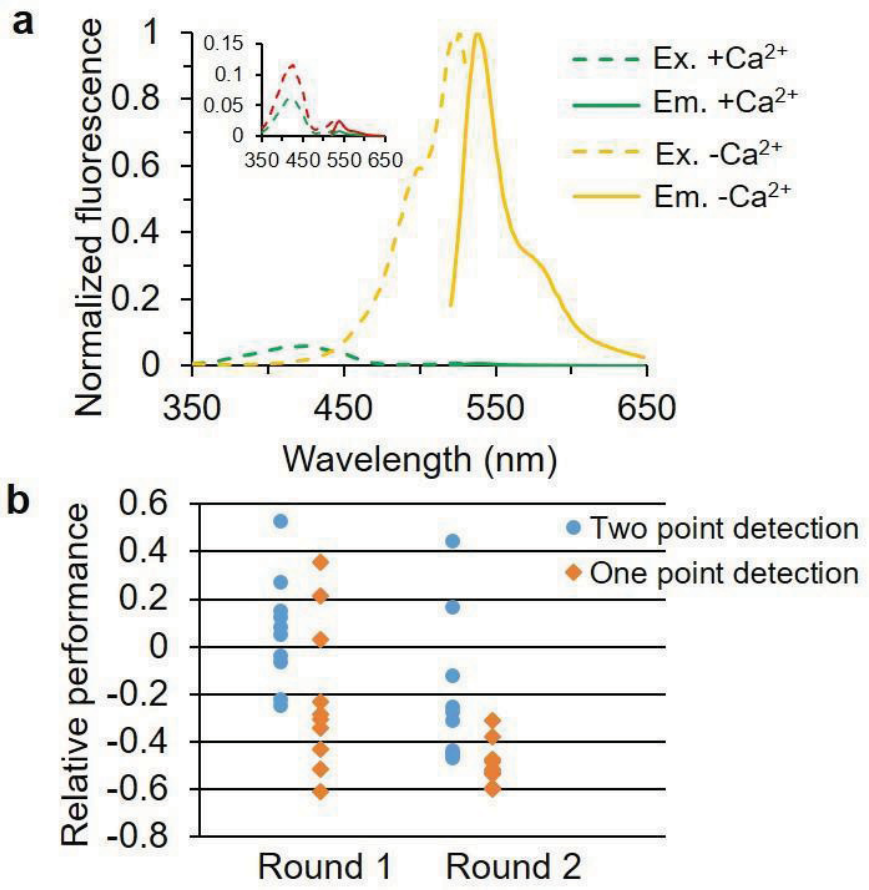

Figure 3.7 Results of μFACS-aided directed evolution of Y-GECO1f.

(a) Excitation (dashed lines) and emission (solid lines) spectra of Y-GECO2f in the Ca^{2+}-free (yellow) and Ca^{2+}-bound states (green). Inset is the excitation (dashed lines) and emission (solid lines) spectra of Y-GECO2f (green) and Y-GECO1f (red) in Ca^{2+}-bound state with zoomed-in y-axis. (b) Comparison of top mutants sorted by two-point and one-point detection systems in first two rounds of screening. Each dot represents a Y-GECO mutant isolated μFACS, where performance = brightness × calcium response and relative performance = (performance of the specific variant) / (performance of best variant from previous round) – 1.

Table 3.2 Mutations in Y-GECO variants.

Variant	Mutations
Y-GECO1m	-
Y-GECO1f	ΔG13[1]
Y-GECO2f	ΔG13, M1T, T30S, S128P

[1] ΔG13 represents that G13 is deleted.

Table 3.3 Properties of Y-GECO variants.

Protein variant	Ca^{2+}	λ_{abs} (nm) with ε ($mM^{-1}cm^{-1}$) in parenthesis	ϕ [1]	ε * ϕ [2]	Change in brightness	pK_a[3]
Y-GECO1f	-	412 (17) 522 (26)	0.05 (x412 m538) 0.75 (x522 m538)	0.9 19.5	4× (x412) 6× (x522)	6.3
	+	412 (23) 522 (6)	0.16 (x412 m538) 0.58 (x522 m538)	3.7 3.5		8.5
Y-GECO2f	-	412 (20) 522 (31)	0.06 (x412 m538) 0.77 (x522 m538)	1.2 23.9	2× (x412) 24× (x522)	6.4
	+	412 (30) 522 (2)	0.09 (x412 m538) 0.51 (x522 m538)	2.7 1.0		9.1

[1] Quantum yield ϕ for emission (m) at the 538 nm peak measured at the two excitation (x) peaks.

[2] The product of ε and ϕ is proportional to the overall fluorescent brightness in units of $mM^{-1}cm^{-1}$.

[3] The pK_a is defined as the pH at which the ratio fluorescence response (excitation at 526 nm/ excitation at 416 nm) is 50% of maximum.

Table 3.4 *In vitro* k_{off} and K_d' of Y-GECO variants

Protein variant	k_{off} (s^{-1})	K_d' (nM) with Hill coefficient in parenthesis
Y-GECO1f	11.65	2500 (2.7)
Y-GECO2f	5.96	2200 (1.4)

3.3.8 Imaging of new Y-GECO variants in cultured cells.

To demonstrate the performance of the most promising of the new Y-GECO variants for live cell imaging, genes were expressed in cultured HeLa cells and dissociated rat hippocampal cells, and fluorescence was imaged using wide-field illumination. Imaging of Y-GECO2f in HeLa cells revealed no fluorescence changes associated with histamine induced Ca^{2+} oscillations. This result is attributed to the high K_d' of the indicator. When Y-GECO2f was expressed in neurons, rapid but relatively small oscillations in fluorescence were observed following neuronal activation with a depolarizing electric pulse (Figure 3.8).

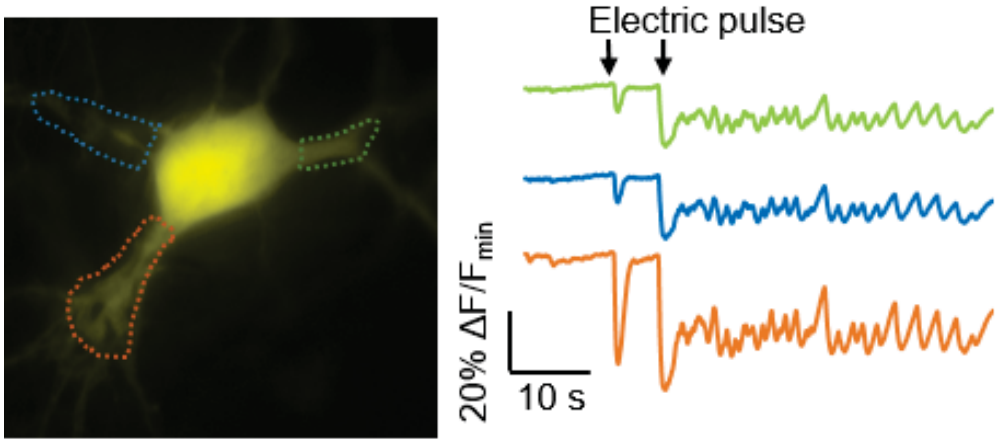

Figure 3.8 Imaging of 2f variants in a dissociated neuron. The traces represent signals from the regions defined with the same color in the left image.

3.4 Supporting Tables

Table 3.5 Oligonucleotides used in this work

Name	5’ to 3’ sequence
FW_XbaI_6His	GCGATGTCTAGAGGTTCTCATCATCATCATCAT CATGGTATGGCTAGC
RV_stop_HindIII	GCGATGAAGCTTCTACTTCGCTGTCATCATTTG TACAAACTCTTCGTAGTTT
FW_BamHI_Kozak_6His	AAACAGGAGGAATTAAGCTTGGGATCCACCAT GGGTTCTCATCATCATCATCATCATGGTATGGC
RV_CaM_stop_EcoRI	CGCGAATTCCTACTTCGCTGTCATCATTTGTAC

Chapter 4. Inverse-response Ca^{2+} indicators for optogenetic visualization of inhibitory synapse activity

4.1 Introduction

Genetically encoded fluorescent protein (FP)-based calcium ion (Ca^{2+}) indicators are widely used for non-invasive monitoring of intracellular signaling dynamics in systems ranging from cultured cells to live animals. Directed protein evolution has proven to be a highly effective strategy to develop Ca^{2+} indicators with altered fluorescence hues[120–122] or improved performance[117,119].

We previously introduced a first generation microfluidic fluorescence activated cell sorter (μFACS) platform for directed evolution of FP-based Ca^{2+} indicators with higher throughput than typical manual screening of bacterial colonies[71]. This platform was applied to the development of yellow genetically encoded Ca^{2+} indicators for optical imaging (Y-GECO, Figure 4.1a) based on mPapaya[242], a monomeric variant of the *Zoanthus* sp. yellow FP[84]. Among these indicators were variants with both fast (Y-GECO1f) and medium (Y-GECO1, designated as Y-GECO1m in the following discussions) dissociation kinetics[71]. The overall dissociation rate constant, k_{off}, is reported, but it should be noted that there are multiple steps involved in the reaction rate. These include Ca^{2+}-dissociation, structural rearrangement, protonation/deprotonation and solvation. The Y-GECO1f indicator exhibited fast Ca^{2+}-dissociation kinetics with k_{off} = 9.75 s^{-1}, which compares favorably to Y-GECO1m (k_{off} = 1.40 s^{-1}) and GCaMP6f (k_{off} = 2.32 s^{-1}) measured under the same conditions. However, the improved kinetics were also associated with substantially decreased Ca^{2+} affinity (K_d' = 2.5 μM for Y-GECO1f vs. 190 nM for Y-GECO1m), and Ca^{2+}-dependent fluorescence change (i.e., the change for Y-GECO1f is ~32% that of Y-GECO1m).

In an effort to provide researchers with an expanded range of Ca^{2+} indicator options, we have used site-directed mutagenesis to modify the Ca^{2+} affinities and off-rate kinetics of Y-GECO variants. We demonstrate that these inverse response indicators are particularly well-suited for imaging of inhibitory neuronal signaling associated with transient decreases in intracellular Ca^{2+} concentration.

4.2 Results

4.2.1 Development of Y-GECO variants with higher affinity and slower kinetics.

To expand the Y-GECO series of indicators to include variants with higher affinity for Ca^{2+}, we explored the introduction of three previously reported mutations, M300I, Q276D, and L309F, in Y-GECO1m (K_d' = 190 nM). One of these mutations (M300I) represents the reversion of a mutation in the first Ca^{2+}-binding site of Y-GECO that was acquired during the earlier development of Y-GECO1f[71]. The other two mutations were reported to contribute to the increased Ca^{2+} affinity of jRGECO1a[243]. Individually, all three mutations increased the affinity to Ca^{2+} (Figure 4.1b). We designated Y-GECO1m M300I as Y-GECO2s (K_d' = 120 nM), Y-GECO1m Q276D M300I as Y-GECO2.1s (K_d' = 63 nM), and Y-GECO1m Q276D M300I L309F as Y-GECO2.2s (K_d' = 25 nM) (Figure 4.1c and Tables 4.1-4.3). These variants are designated with an 's' due to the slower kinetics (Figure 4.2a), which are a necessary consequence of their higher Ca^{2+} affinities. These Y-GECO variants exhibited very similar pH dependence (Figure 4.3b-d).

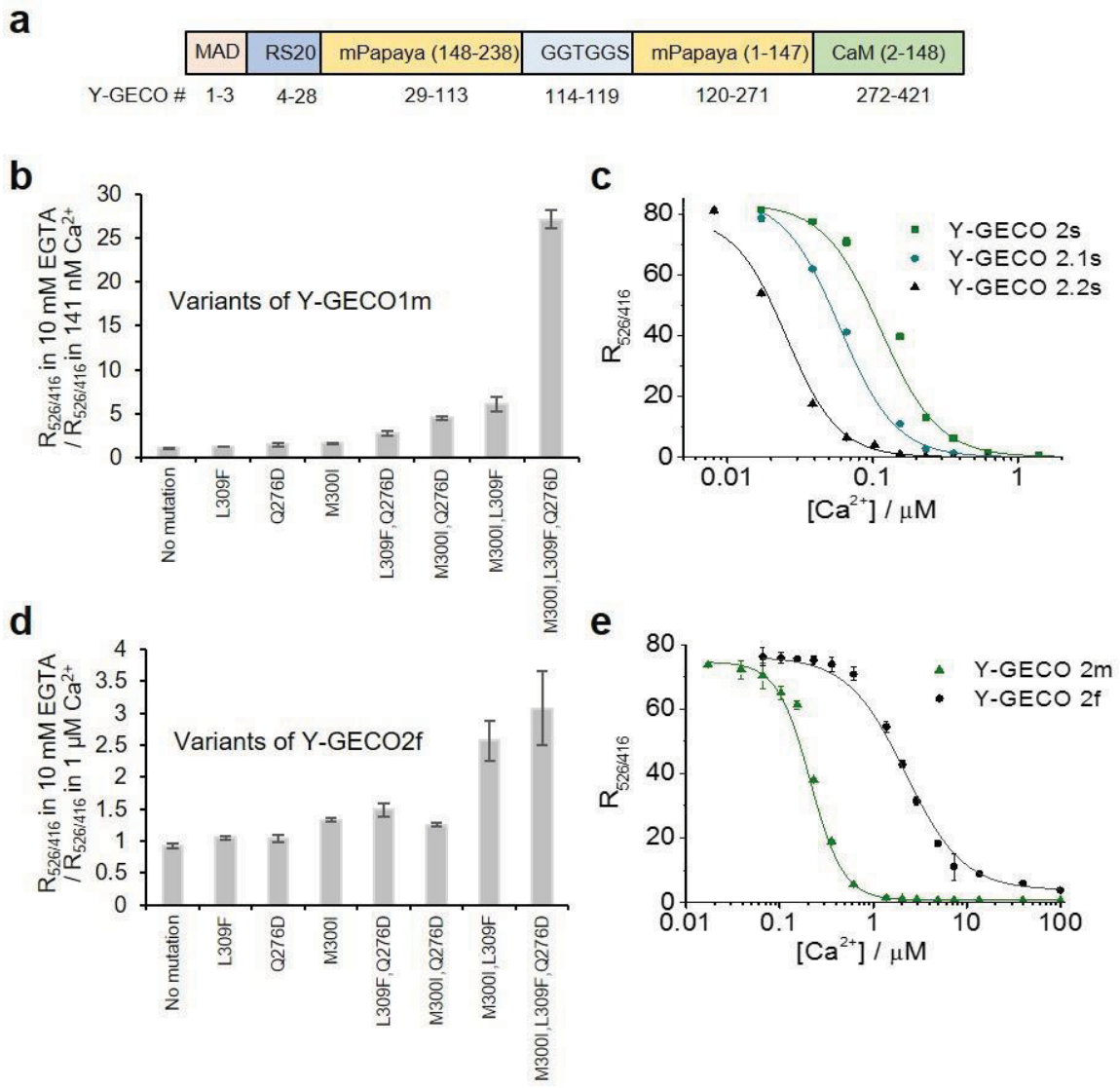

Figure 4.1 Development of new Y-GECO Ca^{2+} indicators.

(a) Gene structure of Y-GECO. (b) Single mutation of M300I, Q276D, and L309F and combinations thereof were introduced into Y-GECO1m. The ratio of $R_{526/416}$ in 10 mM EGTA to $R_{526/416}$ in 141 nM Ca^{2+} was evaluated for Y-GECO1m variants. $R_{526/416}$ is the ratio of fluorescence excited at 526 nm to fluorescence excited at 416 nm. (c) Ca^{2+} titrations for Y-GECO1m-derived variants. Data points were fit to Hill equation to determine K_d'. (d) Screening of Y-GECO2f variants with mutations at the same positions as in (b). The ratio of $R_{526/416}$ in 10 mM EGTA to

$R_{526/416}$ in 1.27 μM Ca^{2+} was evaluated for all variants. The variant with all 3 mutations was designated as Y-GECO2m. (e) Ca^{2+} titration of Y-GECO2m. Y-GECO2f data from Chapter 3.

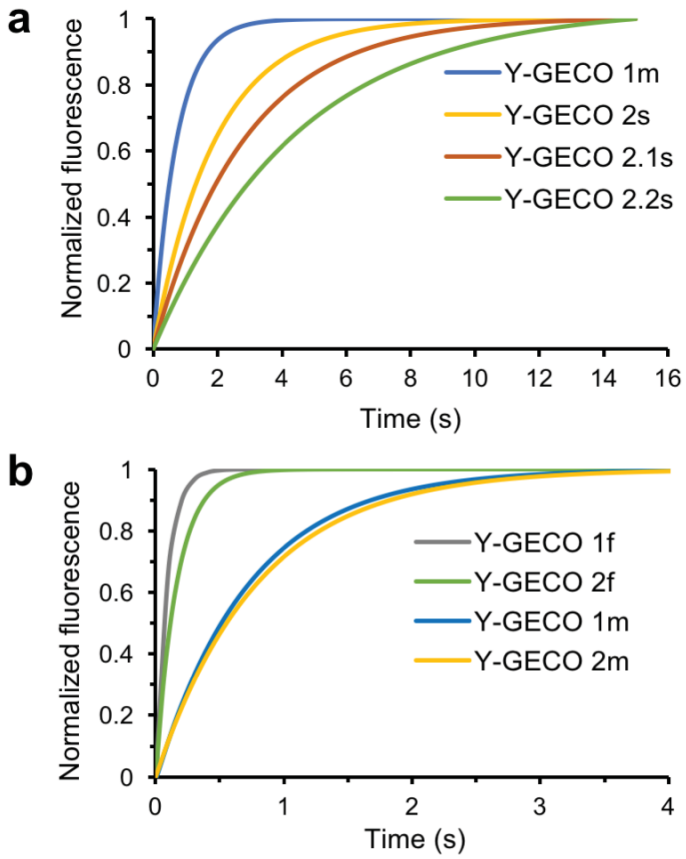

Figure 4.2 Ca^{2+} dissociation kinetics for Y-GECO variants. (a) Ca^{2+}-dissociation kinetics of Y-GECO1m, 2s, 2.1s, and 2.2s. (b) Ca^{2+}-dissociation kinetics of Y-GECO1f, 2f, 1m (reproduced from (a) for the sake of reference), and 2m. Y-GECO1f and 2f data from Chapter 3.

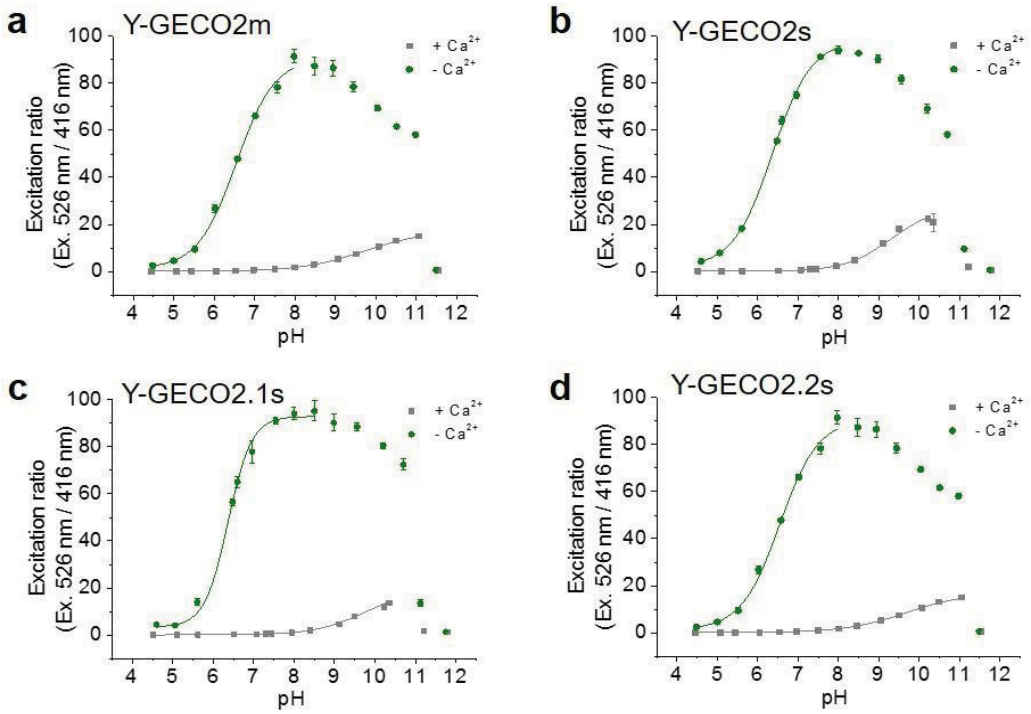

Figure 4.3 pH titrations of Y-GECO variants. (a) Y-GECO2m. (b) Y-GECO2s. (c) Y-GECO2.1s. (d) Y-GECO2.2s.

Table 4.1 Mutations in Y-GECO variants.

Variant	Mutations
Y-GECO1m	-
Y-GECO1f	ΔG13[a]
Y-GECO2f[b]	ΔG13, M1T, T30S, S128P
Y-GECO2m	ΔG13, M1T, T30S, S128P, Q276D, M300I, L309F
Y-GECO2s	M300I
Y-GECO2.1s	Q276D, M300I
Y-GECO2.2s	Q276D, M300I, L309F

[a] ΔG13 represents that G13 is deleted.

[b] Data from Chapter 3.

Table 4.2. Properties of Y-GECO variants.

Protein variant	Ca^{2+}	λ_{abs} (nm) with ε ($mM^{-1}cm^{-1}$) in parenthesis	ϕ [a]	ε*ϕ [b]	Change in brightness	pK_a [c]
Y-GECO1f	-	412 (17) 522 (26)	0.05 (x412 m538) 0.75 (x522 m538)	0.95 19.5	4× (x412) 6× (x522)	6.3
	+	412 (23) 522 (6)	0.16 (x412 m538) 0.58 (x522 m538)	3.7 3.5		8.5
Y-GECO1m	-	412 (18) 522 (25)	0.09 (x412 m538) 0.85 (x522 m538)	1.6 21.3	6× (x412) 19× (x522)	6.5
	+	412 (26) 522 (2)	0.35 (x412 m538) 0.56 (x522 m538)	9.1 1.1		8.8
Y-GECO2f[d]	-	412 (20) 522 (31)	0.06 (x412 m538) 0.77 (x522 m538)	1.2 23.9	3× (x412) 24× (x522)	6.4
	+	412 (30) 522 (2)	0.09 (x412 m538) 0.51 (x522 m538)	2.7 1.0		9.1
Y-GECO2m	-	412 (20) 522 (26)	0.08 (x412 m538) 0.83 (x522 m538)	1.6 21.6	3× (x412) 54× (x522)	6.5
	+	412 (29) 522 (1)	0.16 (x412 m538) 0.40 (x522 m538)	4.6 0.4		9.5
Y-GECO2s	-	412 (17) 522 (25)	0.06 (x412 m538) 0.74 (x522 m538)	0.7 18.5	14× (x412) 26× (x522)	6.3
	+	412 (25) 522 (2)	0.39 (x412 m538) 0.33 (x522 m538)	9.8 0.7		8.9
Y-GECO2.1s	-	412 (18) 522 (25)	0.05 (x412 m538) 0.71 (x522 m538)	0.8 17.8	13× (x412) 59× (x522)	6.3
	+	412 (26) 522 (1)	0.39 (x412 m538) 0.32 (x522 m538)	10.1 0.3		9.3
Y-GECO2.2s	-	412 (17) 522 (23)	0.05 (x412 m538) 0.71 (x522 m538)	0.9 16.3	13× (x412) 54× (x522)	6.5

	412 (27)	0.44 (x412 m538)	11.9	
+				9.6
	522 (1)	0.33 (x522 m538)	0.3	

[a] Quantum yield ϕ for emission (m) at the 538 nm peak measured at the two excitation (x) peaks.

[b] The product of ε and ϕ is proportional to the overall fluorescent brightness in units of $mM^{-1}cm^{-1}$.

[c] The pK_a is defined as the pH at which the fluorescence intensity ratio (excitation at 526 nm / excitation at 416 nm) is 50% of maximum.

[d] Data from Chapter 3.

Table 4.3. *In vitro* k_{off} and K_d' of Y-GECO variants

Protein variant	k_{off} (s^{-1})	K_d' (nM) with Hill coefficient in parenthesis
Y-GECO1f	11.65	2500 (2.7)
Y-GECO1m	1.41	190 (2.6)
Y-GECO2f[a]	5.96	2200 (1.4)
Y-GECO2m	1.23	204 (2.4)
Y-GECO2s	0.53	121 (2.2)
Y-GECO2.1s	0.35	63 (2.3)
Y-GECO2.2s	0.22	25 (2.5)

[a] Data from Chapter 3.

4.2.2 Development of Y-GECO variants with lower affinity and faster kinetics.

In an effort to identify variants with fast and large fluorescent responses, we developed and used a μFACS system based on a polydimethylsiloxane (PDMS) microchip with a two-point detection system (work described in Chapter 3). This system allowed us to screen libraries of randomly mutated Y-GECO1f variants expressed in *Escherichia coli*. Use of this system led to the identification of Y-GECO2f (Table 4.1) which exhibits a 26% increase in brightness and greater than 300% larger Ca^{2+}-dependent fluorescence change relative to Y-GECO1f (Table 4.2) while

retaining a similar spectral profile. Y-GECO2f retained a similar Ca^{2+} affinity and slightly slower k_{off} than Y-GECO1f (Table 4.3).

While Y-GECO1f and Y-GECO2f exhibit relatively fast kinetics, they also share relatively high apparent dissociation constants of 2.5 μM and 2.2 μM, respectively. In an effort to lower the K_d' to better match the typical concentrations of Ca^{2+} in cytoplasm (~0.1 to 1 μM), we introduced the three mutations discussed earlier (M300I, Q276D, and L309F) (Figure 4.1d). Ultimately we found that the combination of all three mutations together gave the highest affinity, with a K_d' of 204 nM (Figure 4.1e). Accordingly, Y-GECO2f Q276D M300I L309F was designated as Y-GECO2m (Table 4.1). As expected for a higher affinity variant, the Ca^{2+} dissociation kinetics of Y-GECO2m had slowed and were similar to Y-GECO1m (Figure 4.2b and Table 4.3). Relative to Y-GECO1m, Y-GECO2m exhibits a larger Ca^{2+}-dependent fluorescence change (over 200% increase) when excited at 526 nm (Figure 4.4), due to the shift of pK_a in the presence of Ca^{2+} towards a higher value (Figure 4.3a and Table 4.2).

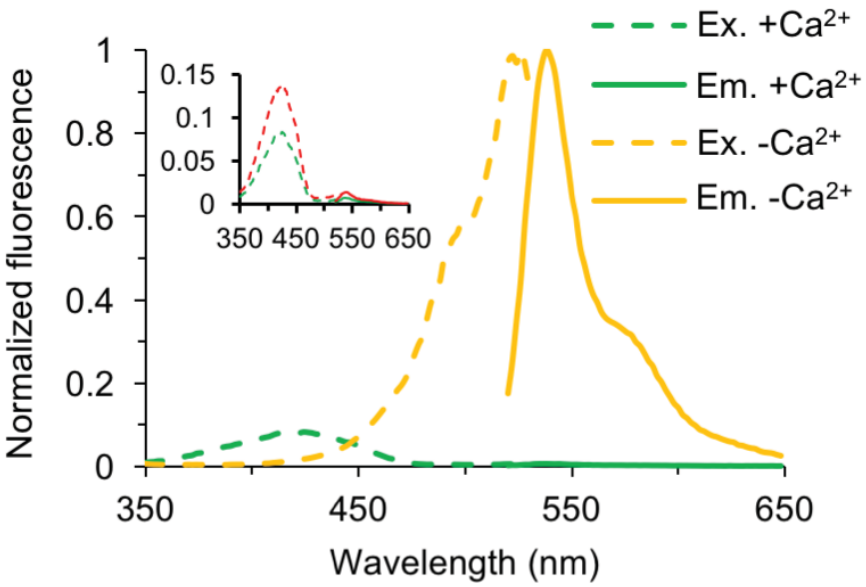

Figure 4.4 Fluorescence spectra for Y-GECO2m in the presence and absence of Ca^{2+}. Excitation

(dashed lines) and emission (solid lines) spectra in the Ca^{2+}-free (yellow) and Ca^{2+}-bound states (green). Inset is the excitation (dashed lines) and emission (solid lines) spectra of Y-GECO2m (green) and Y-GECO1m (red) in Ca^{2+}-bound state with zoomed-in y-axis.

4.2.3 Imaging of new Y-GECO variants in cultured cells.

To demonstrate the performance of the most promising of the new Y-GECO variants for live cell imaging, genes were expressed in cultured HeLa cells and dissociated rat hippocampal cells, and fluorescence was imaged using wide-field illumination. With its near optimal K_d' for detection of cytosolic and reasonable dissociation kinetics, Y-GECO2m is a promising indicator for imaging of Ca^{2+} dynamics in cultured cells. Expression in HeLa cells and treatment with histamine resulted in large fluorescence changes (maximal intensity changes of 10-fold vs Y-GECO2m vs. 6-fold for Y-GECO1m) attributable to oscillations of cytoplasmic Ca^{2+} concentration (Figure 4.5a and Table 4.4). Ratiometric imaging with alternating 438 nm and 480 nm excitation revealed that Y-GECO2m gives ratiometric changes approximately 2-fold greater than that of Y-GECO1m (maximal ratio changes of 35-fold for Y-GECO2m vs. 18-fold for Y-GECO1m) (Figure 4.5b,c and Table 4.4). Analogous experiments with Y-GECO2s revealed average intensity and ratio changes similar to those of Y-GECO2m (Table 4.4). Y-GECO2m also proved effective for imaging of slow Ca^{2+} waves when expressed in glial cells in dissociated rat hippocampal cultures (Figure 4.5d).

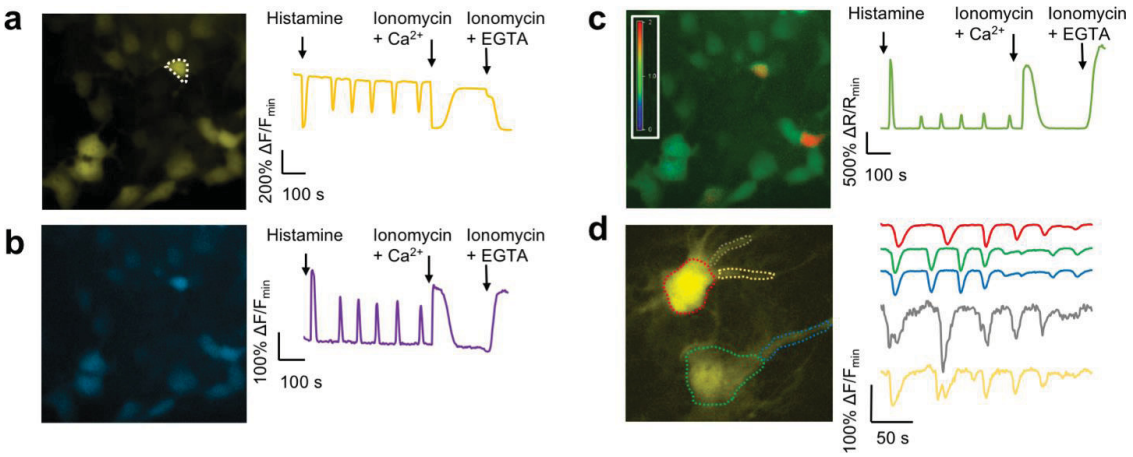

Figure 4.5 Imaging of new Y-GECO2m.

(a - c) Fluorescence images of Hela cells expressing Y-GECO2m. For each panel, the right hand chart shows fluorescence signals for the cell enclosed with a dashed-line in response to histamine-induced Ca^{2+} oscillations. (a) Fluorescence with excitation at 480 nm. (b) Fluorescence with excitation at 440 nm. (c) Ratiometric response (Excitation at 440 nm/ excitation at 480 nm). (d) Fluorescent image of glial cells in dissociated rat hippocampal culture expressing Y-GECO2m. The fluorescence responses of selected regions to the spontaneous Ca^{2+} changes over time are demonstrated in the traces at the right side in the same color (excitation at 480 nm).

Table 4.4. Characterization of Y-GECO variants in HeLa cells. Cells were treated first with histamine (abb. His), then with EGTA/ionomycin (abb. EGTA), and then with Ca^{2+}/ionomycin (abb. Ca^{2+}).

Protein variant	n[a]		Maximum EGTA to minimum Ca^{2+} ratio[b]	Maximum His to minimum His ratio[c]	His to EGTA/Ca^{2+} ratio of ratios[d]
Y-GECO1m	33	Intensity[e]	6 ± 4	1.8 ± 0.5	0.5 ± 0.3
		Ratio[f]	18 ± 14	4 ± 2	0.4 ± 0.4
Y-GECO2m	47	Intensity	10 ± 5	2.2 ± 0.6	0.3 ± 0.2
		Ratio	35 ± 19	6 ± 3	0.3 ± 0.2
Y-GECO2s	48	Intensity	11 ± 5	3 ± 1	0.4 ± 0.2
		Ratio	30 ± 16	8 ± 5	0.3 ± 0.2

[a] Number of transfected HeLa cells imaged for each variant.

[b] The highest fluorescence response after EGTA treatment to the lowest response after Ca^{2+} treatment.

[c] The highest fluorescence response to the lowest response after His treatment.

[d] The ratio of (max His to min His) to (max EGTA to min Ca^{2+}).

[e] Intensity with 480/40 nm excitation and 535/40 nm emission.

[f] Ratio of intensity with 438/24 nm excitation and 542/27 nm emission divided by intensity with 480/40 nm excitation and 535/40 nm emission.

4.2.4 Imaging of inhibitory synapse activity in *Drosophila* using the YGECO2s series.

Since all Y-GECO variants exhibit an inverted response to Ca^{2+}, we reasoned that they would be useful as positive indicator for detecting inhibitory (hyperpolarizing) responses, possibly enabling transient decreases in Ca^{2+} to be imaged with improved sensitivity. To explore this possibility and to examine the dependence of the response on indicator K_d', we expressed a series of Y-GECO variants in the *Drosophila melanogaster* Mi1 neuron. The Mi1 neuron acts in the ON circuit,

depolarizing when light increases and hyperpolarizing when light decreases[244,245]. Here, we mimic the light decrease by optogenetically stimulating the L1 neuron that projects from the lamina into the medulla where it makes an inhibitory synaptic connection to Mi1[246] (Figure 4.6a). When inhibited, the free Ca^{2+} levels in Mi1 drop, a response thus far observed with Ca^{2+} indicators that increase fluorescence in response to increases in Ca^{2+} concentration[246].

We used the Gal4/UAS system to express Chrimson[247] in L1 neurons and the LexA/LexAOP system to express Y-GECO1m (K_d' = 190 nM), Y-GECO2s (K_d' = 120 nM), Y-GECO2.1s (K_d' = 63 nM), or Y-GECO2.2s (K_d' = 25 nM) in Mi1 neurons (Figure 4.7a). Chrimson activation with red light stimulation (660 nm, 1-photon) occurred every 30 s at a constant intensity of 0.24 mW/mm^2 with duration increasing from 1, to 2, to 4, to 8 seconds, followed with a final 1 s pulse (Figure 4.7c). During activation, Y-GECO fluorescence was imaged using 2-photon excitation (920 nm) in *ex vivo* preparations, in an ROI spanning medulla layers 8-10 where the dendritic arbors from Mi1 provide the largest grouped area (Figure 4.6a-c and Figure 4.7b).

These experiments revealed that fluorescence response ($\Delta F/F$) of a particular Y-GECO variant corresponded with the variant's K_d' and the length of the stimulation period (Figure 4.6d,e). The correspondence between K_d' and fluorescence response is best observed during the 8 s stimulation period. For this stimulation period, the highest affinity indicator, Y-GECO2.2s, exhibited the greatest $\Delta F/F$, followed by Y-GECO2.1s, then Y-GECO2s, and finally Y-GECO1m. All variants exhibited an increasing delay to maximum signal with increasing stimulation period (Figure 4.6f). Y-GECO2.2s exhibited the greatest signal to noise ratio (SNR) for the 8s stimulation period but

the two variants with intermediate Ca^{2+} affinity, Y-GECO2s and Y-GECO2.1s, exhibited higher SNR at the 4s stimulation, and similar SNR at 2 s and 1 s stimulation (Figure 4.6g).

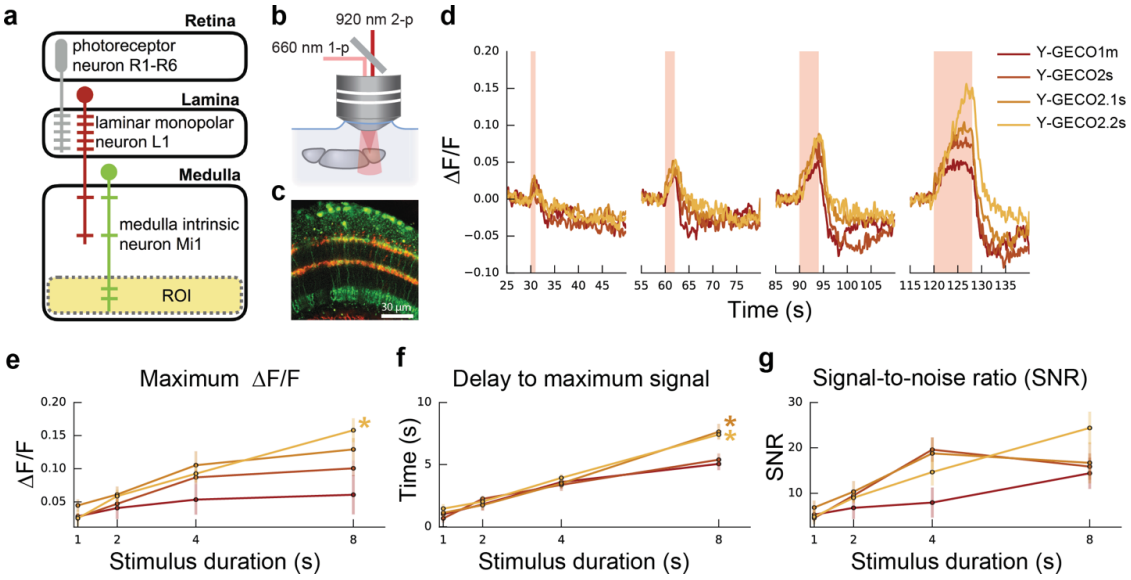

Figure 4.6 Imaging of Mi1 activation upon optogenetic activation of L1.

(a) Schematic (modified from Strother *et al.*)[245] featuring an L1 neuron (red) projecting from lamina to the medulla where it connects to an Mi1 neuron in layer 4. The Y-GECO response in Mi1 is measured in a region-of-interest (ROI) (faded yellow) spanning layers 8-10 (Figure 4.7b). (b) Y-GECO fluorescence was imaged using 2-photon excitation at 920 nm, while optogenetic activation of Chrimson was achieved using 1-photon excitation at 660 nm. (c) Image of L1 neurons labeled with Chrimson-tdTomato (red) and Mi neurons expressing Y-GECO1m (green). (d) Red light triggered Chrimson activation in L1 over durations spanning 1, 2, 4, and 8 seconds and presented here in the order they occurred during the protocol (Figure 4.7c). The median ΔF/F response for each time period is shown. Raw data is provided in Figure 4.8. (e-f) The maximum ΔF/F response (e), delay to maximum to signal (f), and signal-to-noise ratio (g), are shown for simulations lasting 1, 2, 4 and 8 s. Lines for Y-GECO variants are colored as in (b). The 1 s

stimulation derives from only the first 1 s time stimulation in the protocol. The response is measured from stimulation onset and includes 2 s after the stimulation is turned off. Bars are standard error. An asterisk indicates that Kruskal-Wallis H-test finds significant difference ($P < 0.05$) in the group and paired Wilcoxon ranksum finds point significantly different between Y-GECO1m and the given variant ($P < 0.05$). Numbers tested Y-GECO1m = 5, Y-GECO2s = 9, Y-GECO2.1s = 8, and Y-GECO2.2s = 9.

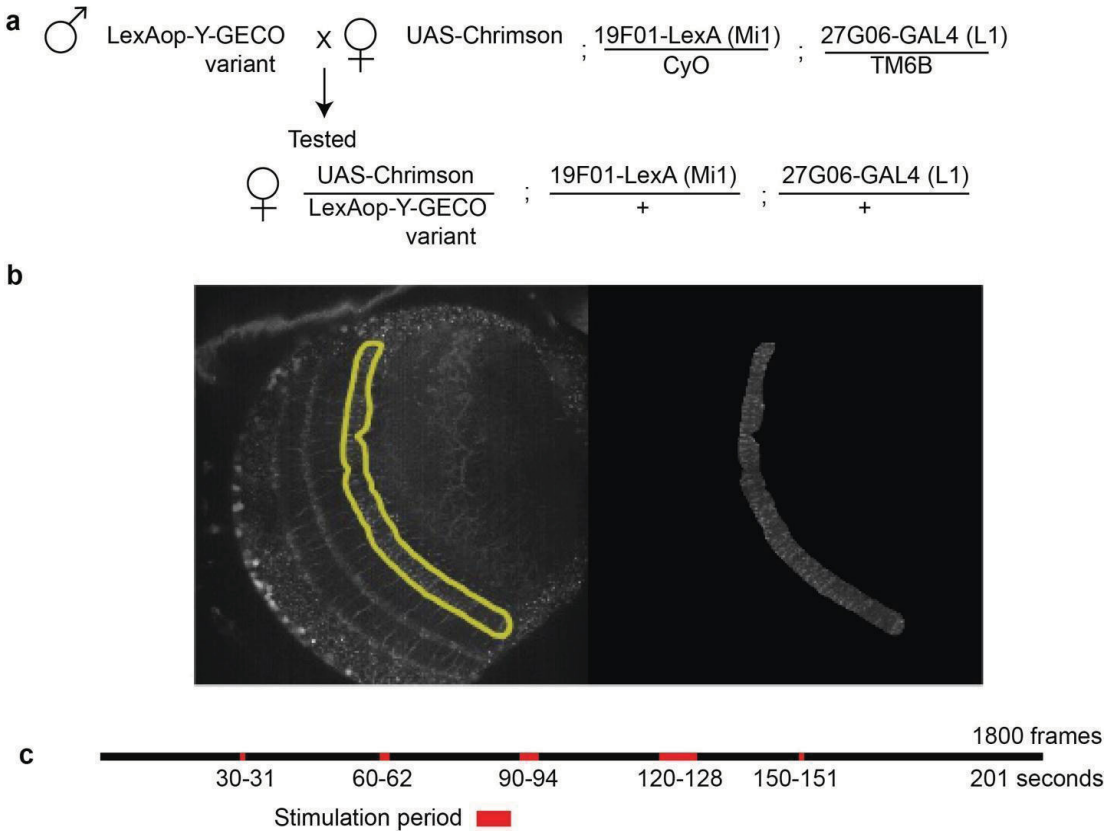

Figure 4.7 Generation of transgenic flies and imaging protocol.

(a) Crossing scheme used to generate females expressing the Y-GECO variants. The GAL4/UAS system was used to drive expression of Chrimson in L1 neurons, and the LexA/LexAop system was used to drive expression in Mi1 neurons. Males passed a LexAop driven Y-GECO while

females passed the UAS-Chrimson (10×UAS-Chrimson-tdTomato) driver lines 19F01-LexA and 27G06-GAL4. The 27G06-GAL4 drives Chrimson expression in the L1 neurons while the 19F01-LexA drives Y-GECO variant expression in the Mi1 neurons. (b) Representative image (left) shows the standard deviation in the medulla over the time series from a single plane from a Y-GECO2.2s fly. Outline in yellow is the ROI used to measure changes in fluorescence in the M8-10 layer. Image (right) shows the standard deviation after application of a mask defined by the ROI at left. (c) Stimulation protocol where red light is turned on (represented in red) at a constant intensity and durations of 1 s, 2 s, 4 s, 8 s and back to 1 s at 30 s intervals.

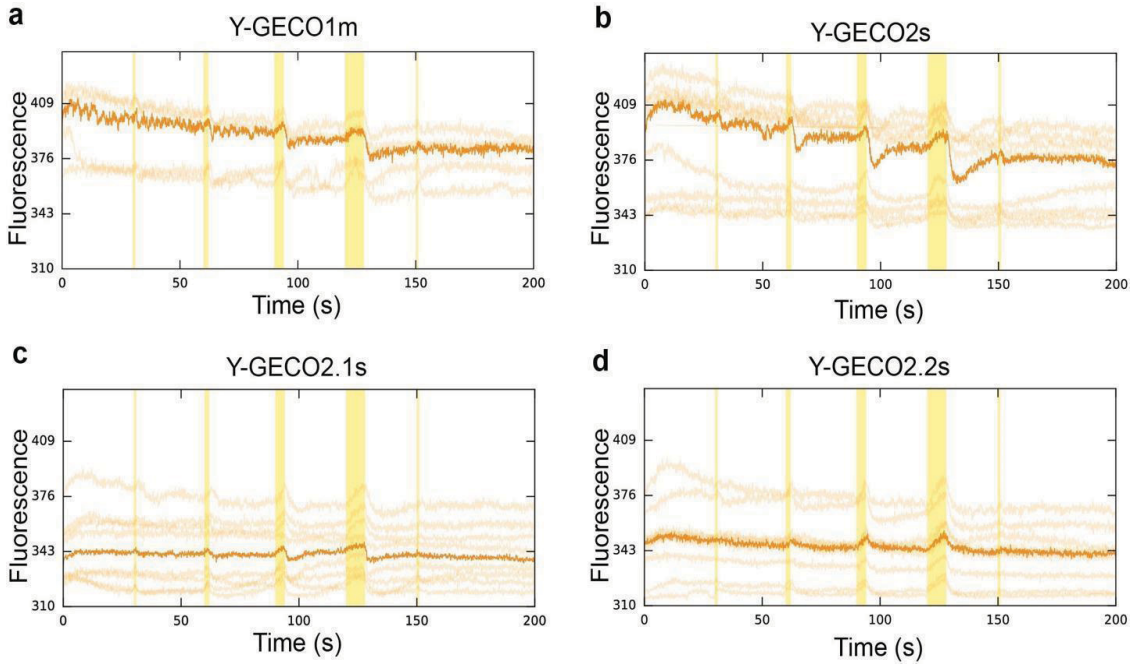

Figure 4.8 Raw fluorescence traces from fly imaging. Raw fluorescence measured from the Y-GECO variants tested over the time series. Shaded orange represents individual trials. Dark orange is the median result.

4.3 Discussion

4.3.1 New Y-GECO variants with a broad range of Ca^{2+} affinities.

The Y-GECO series now contains a total of seven variants with K_d' values ranging over 2 orders of magnitude. From highest to lowest affinity, this series includes: Y-GECO2.2s (K_d' = 25 nM); Y-GECO2.1s (K_d' = 63 nM); Y-GECO2s (K_d' = 121 nM); Y-GECO1m (K_d' = 190 nM); Y-GECO2m (K_d' = 204 nM); Y-GECO2f (K_d' = 2200 nM); and Y-GECO1f (K_d' = 2500 nM). For monitoring of neural activity with a cytosolic indicator, Ca^{2+} K_d' values in the 100 to 200 nM range have been empirically found to be close to ideal, as demonstrated by the GCaMP series of highly optimized indicators[119]. Due to the fundamental relationship $K_d = k_{off} / k_{on}$, faster off rate kinetics (k_{off}) must be associated with a higher K_d, assuming no changes in on rate kinetics (k_{on}). Accordingly, all genetically encoded Ca^{2+} indicators for neural activity imaging represent compromises between K_d (lower is better) and k_{off} (higher is better). As the Y-GECO series of indicators all share very similar spectral properties, they provide researchers with the opportunity to empirically test and identify the particular indicator that is best tuned to the respond to intracellular Ca^{2+} dynamics under investigation. In addition, their inverse response behavior means that decreases in Ca^{2+} concentration associated with hyperpolarization will be reported as increasing fluorescence signals, which are generally preferred for tissue imaging.

4.3.2 Inverse response Ca^{2+} indicators for visualization of hyperpolarization.

It has been demonstrated, using *in vivo* electrophysiological recordings[244] and imaging with a genetically encoded voltage indicator[246], that a light to dark transition causes the L1 neuron of the *Drosophila* visual pathway to depolarize. In response, the Mi1 neuron hyperpolarizes, clearly demonstrating an inhibitory contact between L1 and Mi1. *In vivo* Ca^{2+} imaging with GCaMP6f[119]

has revealed that the intracellular Ca^{2+} concentration follows the membrane polarization (i.e., a Ca^{2+} decrease below resting levels during hyperpolarization), in layer M10 of stimulated Mi1 neurons[246].

To further probe Ca^{2+} signaling in the Mi1 neuron, we used a series of Y-GECO indicators with K_d' values ranging from 25 nM to 190 nM and expressed them in Mi neurons at the same concentration and activated the neurons identically. These experiments revealed that the K_d' of the indicator has a substantial effect on the ΔF/F and SNR, and a lesser effect on the delay to reach the maximum signal. For an 8 s stimulation, the relationship between K_d' and ΔF/F was clear: a lower K_d' gave a higher ΔF/F. We speculate that, for the 8 s stimulation, free Ca^{2+} levels drop below K_d' (i.e., well below 25 nM) for all variants. Variants with a greater K_d' (i.e., 100 – 200 nM) have a reduced change in fluorescence because their K_d' is closer to the resting Ca^{2+} concentration and so they have higher fluorescence prior to stimulation and diminished ΔF/F. Consistent with their larger values of k_{off} (i.e., faster dissociation), the two variants with higher K_d' (Y-GECO1m and Y-GECO2s) exhibited a decreased delay to maximum fluorescence relative to the two variants with lower K_d' (Y-GECO2.1s and Y-GECO2.2s) with an 8 s stimulus. Lastly, the signal-to-noise ratio (SNR) depends on the amount of fluorescence signal acquired, which is necessarily dependent on both K_d' and k_{off}. Accordingly, neither the highest (Y-GECO2.2s) nor the lowest (Y-GECO1m) affinity variants (slowest and fastest, respectively) gave the highest SNR at stimulus durations up to 4 s. Rather, the two middle affinity variants (Y-GECO2s and Y-GECO2.1s), which must represent appropriate compromises of affinity and off-rate kinetics, tended to provide the best SNR at stimulus durations up to 4 s. Following a stimulus duration of 8 s, the slow kinetics of the high affinity Y-GECO2.2s variant are presumably no longer limiting and so this variant provides the highest SNR within the series.

4.3.3 Summary.

Despite the fact that 30% of neurons in humans and *Drosophila* are inhibitory, there are relatively few optogenetic indicators optimized for imaging of inhibitory neuronal activity. We propose that, for imaging of inhibitory activity, inverse response Ca^{2+} indicators have an inherent advantage to direct response Ca^{2+} indicators. Specifically, imaging of inhibitory activity with a direct response Ca^{2+} requires detection of a dimming response that could be readily obscured by out of focus fluorescence from adjacent bright cells. In contrast, inhibitory activity could be more easily detected with an inverse response Ca^{2+} indicator due to the diminished background fluorescence originating from adjacent out-of-focus cells.

Our results suggest that, for an inverse response indicator in the Mi1 neuron, a K_d' of less than 100 nM produces greater changes in fluorescence without compromising the response time. In contrast, direct response Ca^{2+} indicators optimized for detection of neuronal action potentials range have been found to perform best when the K_d' is tuned to the 100 to 200 nM range. An important caveat is that this conclusion applies only to the Mi1 neuron within the synaptic region studied. Other neurons or even regions within the same neuron could have different resting Ca^{2+} levels which would change the optimum K_d'. For this reason, we advocate the empirical identification of the optimal K_d' by testing a series of variants such as the ones described in this work.

4.4 Methods

4.4.1 Site-directed mutagenesis for mutation introduction.

Mutations were introduced by Quikchange II Site-directed Mutagenesis kit (Agilent Technologies) with primers containing desired mutations at specific positions.

4.4.2 Purification and *in vitro* characterization of Y-GECO proteins.

The procedure for purification and determination of extinction coefficient, quantum yield, and K_d' of Y-GECO variants has been previously in Section 3.2.5.

4.4.3 Kinetics of Ca^{2+} dissociation fluorescence change of Y-GECO.

Stopped-flow spectroscopy was used to evaluate reaction kinetics of FP with Ca^{2+}. Ca^{2+}-dissociation kinetics of purified Y-GECO indicators were measured as described previously in Section 3.2.6. The fluorescence intensity vs. time was collected, plotted and fit to a single exponential curve, giving k_{off}.

4.4.4 Construction of plasmids for mammalian cell expression.

Plasmids for mammalian cell expression were constructed as described in Section 3.2.7.

4.4.5 HeLa cell culture and imaging.

HeLa cells were cultured and transfected as described previously[71]. Wide-field imaging of cells was performed on an epifluorescence inverted microscope (Eclipse Ti-E, Nikon) equipped with a digital CCD camera (QuantEM 512SC). The microscope and camera were controlled using NIS-Elements Advanced Research software. Cells were imaged with a 20× air objective lens (NA 0.8).

The cells were illuminated by a 100 W mercury arc lamp and a 25% neutral density filter was used to reduce the intensity of the light. To record the long Stokes shift fluorescence, we used a filter set of 438/24 nm (excitation), 458 nm (dichroic) and 542/27 nm (emission). Exposure time was set to 700 ms. To record the short Stokes shift fluorescence, we used a filter set of 480/40 nm (excitation), 505 (dichroic) nm and 535/40 nm (emission), with exposure time 500 ms.

To image histamine induced Ca^{2+} dynamics, images were acquired every 4 s for ~ 20 min. After ~ 30 s of initial recording, 100 μM histamine solution was added to the dish to reach a final concentration of 10 μM. After ~10 min recording, 10 mM EGTA, 40 μM ionomycin in Ca^{2+}-and Mg^{2+}-free HHBSS was then added to reach a final concentration of 1mM EGTA, 4 μM ionomycin. Then, 20 mM Ca^{2+}, 40 μM ionomycin in Ca^{2+} and Mg^{2+} free HHBSS was then added to reach a final concentration of 2 mM Ca^{2+}, 4 μM ionomycin.

4.4.6 *Drosophila* imaging.

LexAOP2-Y-GECO variants were inserted into the genome at the su(Hw)attP8 landing site. Brains from females (Genotype: 10xUAS-Chrimson-tdTomato (attP18)/ LexAOP2-Y-GECO (suHwattP8); 19F01-LexA (suHwattP5) (Mi1) /+; 27G06-GAL4 (attP2) (L1)/+) expressing Chrimson-tdTomato in L1 neurons and Y-GECO variants in Mi1 neurons were tested

Flies were reared at 25 ℃ on retinal supplemented (0.2 mM) cornmeal medium that was shielded from light. All experiments were performed on female flies, 1-4 days after eclosion. Brains were dissected in a saline bath (103 mM NaCl, 3 mM KCl, 2 mM $CaCl_2$, 4 mM $MgCl_2$, 26 mM $NaHCO_3$, 1 mM NaH_2PO_4, 8 mM trehalose, 10 mM glucose, 5 mM TES, bubbled with 95% O_2 / 5% CO_2).

After dissection, the brain was positioned anterior side up on a coverslip in a Sylgard dish submerged in 3 ml saline at 20°C.

The sample was imaged with a resonant scanning 2-photon microscope with near-infrared excitation (920 nm, Spectra-Physics, INSIGHT DS DUAL) and a 25× objective (Nikon MRD77225 25XW). The microscope was controlled by using ScanImage 2015.v3 (Vidrio Technologies)[248]. Images were acquired with 141 μm × 141 μm field of view at 512 × 512 pixel resolution, approximately 9 Hz frame rate after averaging 5 frames. The excitation power for Ca^{2+} imaging measurement was 12 mW.

For the photostimulation, the light-gated ion channel Chrimson was activated with a 660-nm LED (M660L3 Thorlabs) coupled to a digital micromirror device (Texas Instruments DLPC300 Light Crafter) and combined with the imaging path with a FF757-DiO1 dichroic (Semrock). On the emission side, the primary dichroic was Di02-R635 (Semrock), the detection arm dichroic was 565DCXR (Chroma), and the emission filters were FF03-525/50 and FF01-625/90 (Semrock). Photostimulation light was delivered in a pulse train that consisted of three 5 pulses with increasing pulse durations (1, 2, 4, 8 and 1 seconds) every 30 seconds as outlined in Figure 4.7c. The light intensity was 0.24 mW/mm^2, as measured using Thorlabs S170C power sensor.

In custom python scripts, an ROI was drawn over layers M8-10 on a figure containing the standard deviation over time. Before calculating the change in fluorescence (ΔF), the offset was subtracted from the fluorescence and then baseline fluorescence was subtracted. Baseline fluorescence is the median fluorescence over a 5 s time period before stimulation started. The ΔF was then divided by baseline to normalize signal (ΔF/F). The final signal was run through a gaussian filter (sigma =1).

The time period included in the maximum fluorescence, delay to maximum signal, and signal to noise ratio start from stimulation start to 2 s after stimulation ended. Signal to noise ratio was calculated by taking the maximum ΔF/F signal and dividing by the baseline (5 s period before simulation started) standard deviation.

4.5 Supporting Tables

Table 4.5. Oligonucleotides used in this work

Name	5' to 3' sequence
FW_XbaI_6His	GCGATGTCTAGAGGTTCTCATCATCATCATCATCATGGT ATGGCTAGC
RV_stop_HindIII	GCGATGAAGCTTCTACTTCGCTGTCATCATTTGTACAAA CTCTTCGTAGTTT
FW_BamHI_Koza k_6His	AAACAGGAGGAATTAAGCTTGGGATCCACCATGGGTTC TCATCATCATCATCATCATGGTATGGC
RV_CaM_stop_Ec oRI	CGCGAATTCCTACTTCGCTGTCATCATTTGTAC
FW_ M300I	CGGGGATGGGACGATAACAACCGAGGAG
FW_ Q276D	GCTGACACGCGTGACGACCTGACTGAAGAGCAG
FW_ L309F	GCTGGGGACGGTGTTCCGGTCTCTGGGGC

Chapter 5. Centrifugal microfluidic sample preparation for metabolite analysis in serum sample by mass spectrometry

5.1 Introduction

A profile of metabolites can provide useful information for biomarker discovery[249–252], diagnosis of disease[253–257] and toxic effect assessment of drugs, toxins and food additives[258–262]. Considerable research in this field is focused on small molecule metabolites (< 1500 Da) such as amino acids[257,263–265], lipids[266–269] and fatty acids[264,270,271]. For example, it has been demonstrated that fingerprinting free amino acids in plasma shows great potential for early diagnosis of cancer[257]. Methods of metabolite fingerprinting are required for discovery and for diagnostics. This chapter focuses on diagnostics and the need to develop automated sample preparation methods.

Human blood serves as a liquid carrier of small molecules exchanged from tissues and organs in the body, so human blood, serum and plasma are rich in various kinds of metabolites which are closely related to the conditions of the body[272]. Profiling and analyzing the metabolites in blood derived samples such as serum is of primary interest for metabolomics research. As human serum contains a high concentration of proteins as well as other biomolecules, sample preparation is required to remove those biomolecules, which may generate large background signals in the following detection step. Conventional sample preparation methods for human serum include organic solvent precipitation and ultrafiltration[273–276], which can only prepare relatively large volume samples (>100 μL). Organic solvent precipitation methods take time and require that many operation steps be performed. Ultrafiltration[185,277,278] is often conducted using commercial

ultrafiltration centrifuge tubes, requiring a high-speed centrifuge in the lab as well as other standard lab steps.

Microfluidic techniques for convenient sample preparation are often suggested, but rarely realized. One of the challenges is that sample placed on a chip is often in too low a volume to be recovered for analysis off-chip, and integrating all of the detection components makes for an expensive single-use disposable device. In this work, we are developing a system to give dirty sample in/clean sample out, which may eventually be developed with a generic sample preparation tool. Such a device can be low cost and rapid.

Digital microfluidics has been utilized for sample preparation coupled with mass spectrometry in proteomic[279–283] and metabolomics[284,285] studies. However, digital microfluidics requires a sophisticated electronic control system for fluid manipulations and relatively high cost for device fabrication. Centrifugal microfluidics features a simple control system, inexpensive material for device fabrication and offers the possibility of high-throughput sample processing[137,138]. For example, Gustafsson *et al* reported a centrifugal microfluidic device for parallel preparation of 96 samples, including concentration and desalting, for MALDI analysis of peptides[181].

As we mentioned in Chapter 1, centrifugal microfluidic devices to prepare samples for metabolomic studies have not been reported. In this chapter we introduce a centrifugal microfluidic device to prepare ~ 5 μL serum samples for small molecule analysis by solid matrix laser desorption/ionization mass spectrometry (SMALDI-MS). Our centrifugal microfluidic device, fabricated by print, cut and laminate method[161], enables sample preparation by removing proteins and lipids from serum. The sample is removed from the disc following clean-up, then transferred

to a SMALDI-chip, which provides an additional clean-up by segregating the electrolyte background from the sample salts. The SMALDI-chip utilizes a unique crystallization-based segregation step that arises from surface properties of the chip, to give protein, lipid and background electrolyte free sample. The resulting mass spectrum of the prepared sample shows a relatively clean background and high signal to noise ratio for metabolite peaks. Quantitative analysis of three metabolites are demonstrated. These metabolites are part of a whole fingerprint analysis which could facilitate early diagnosis of a disease, such as cancer, as discussed above. By separating the detection system from the microfluidic functions, a relatively generic sample preparation step which can be used for automated sample processing in the lab or transported in the field, is readily achieved.

5.2 Experimental section

5.2.1 Design of the centrifugal disc

The centrifugal microfluidic device for human serum clean-up consists of seven layers of polyester film with 10 cm diameter (Figure 5.1a). Layer 2, 4 and 6 are printed with toner as bonding agent between layers. Features are cut by laser cutter and layers are aligned and laminated by hot laminator, as described later in 5.2.2. The assembled disc is fixed on a spinning motor (0923/S010-R1, McMaster Carr), which is controlled by a DC power supply (6217A, Hewlett Packard). The spinning frequency is measured by an RPM meter (1905T22, McMaster Carr). Figure 5.1b represents the microfluidic design of one processing unit on the disc for sample preparation, which includes three reservoirs. The microfluidic features at different layers are illustrated in different colors corresponding to Figure 5.1a. Reservoir 1 and 2 are for sample and reagent introduction, respectively. A filter is inserted in the channel between reservoir 1 and 3, as indicated in Figure

5.1b, to separate supernatant and pellets under filtration. Reservoir 3 is a two-level structure with a shallow center area for sample drying and mixing and its side view is illustrated in Figure 1C. Sample stays in the center due to capillary force when the device is not spinning. When sample is being dried under vacuum, liquid will not contact with the edge of the reservoir and enter the gap between layers. When the device is spinning and the centrifugal force overcomes the capillary force, the liquid sample will be driven to the outmost region in the reservoir 3. Using spin-stop cycles, the liquid is moving to accelerate sample mixing (Figure 5.1c). A small collector at the far end of reservoir 3 (shown at the bottom in Figure 5.1b) is used to collect silica nanoparticles by centrifugation which is added to remove proteins in the sample.

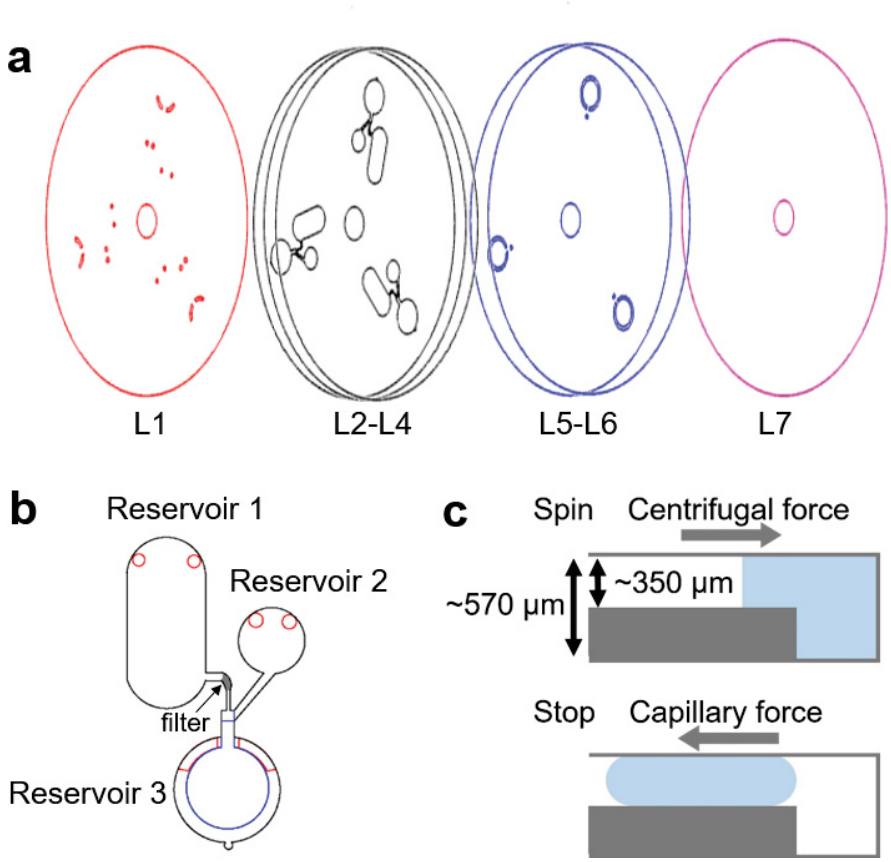

Figure 5.1 (a) Schematic representation of the centrifugal microfluidic device (seven layers of

polyester films). Features on L2-L4 are same and L5-L6 are same. (b) Design of the centrifugal microfluidics. Vents and inlets are shown in red. Shallower area is shown inside blue lines. (c) Side views of reservoir 3 under a spin-stop cycle.

5.2.2 Fabrication of the centrifugal disc

The A4 size transparency sheets (APO09209, APOLLO) were used as substrates for printing and laser cutting. For toner-printed transparency films, the whole area of each side was printed with 3 layers of black toner at a resolution of 600 dpi with the laser printer (HP LaserJet 2055dn). The DXF format file of the microfluidic design was created in AutoCAD software for laser cutting. Each layer of transparencies was fabricated by a CO_2 laser cutter (Epilog Legend) in the 'Vector cutting' mode. The laser cutter was manually aligned and the cutting was performed with the setting of 9% power, 80% speed, 1200 DPI and 5000 frequency. The fabricated layers were removed from the rest of the transparencies, cleaned with ethanol and distilled water and dried under N_2 before assembling. Transparency films were manually aligned and taped together with Scotch tape one layer a time, from bottom layer to top layer. Before adding the top layer, a small piece (~ 1 mm×1 mm) of glass fiber filter (Whatman GF/B) was inserted. The assembled device was sandwiched between two layers of aluminum foil for hot lamination. The lamination was performed by using the laminator (Catena 35) under 260F, 3 mm roller pressure and lowest speed. The device was then removed from the foil and cooled for 1 min.

5.2.3 Fabrication and surface modification of SMALDI chip

Vertical silicon nano-posts (500 nm thickness) were deposited on a silicon wafer substrate (Silicon Materials, prime grade, 500 μm thickness) by using the GLAD technique[226]. An 86° deposition

angle with rotation at 2.4 nm deposited/rotation was employed. Silicon (Kurt J. Lesker, p-type, 99.999% purity) was evaporated by electron-beam under vacuum. The fabricated GLAD film was then transferred into an air environment where oxide was formed on the surface of the silicon nano-posts. To generate fluorinated derivatization on the surface, the film was immersed in the methanol solution (1.2% v/v) of (1H, 1H, 2H, 2H-perfluorooctyl) dimethylchlorosilane (pFMe2SiCl, Gelest) at room temperature for 30 min reaction[185] (Figure 5.2) . The film was then transferred into a petri dish and stored overnight for use.

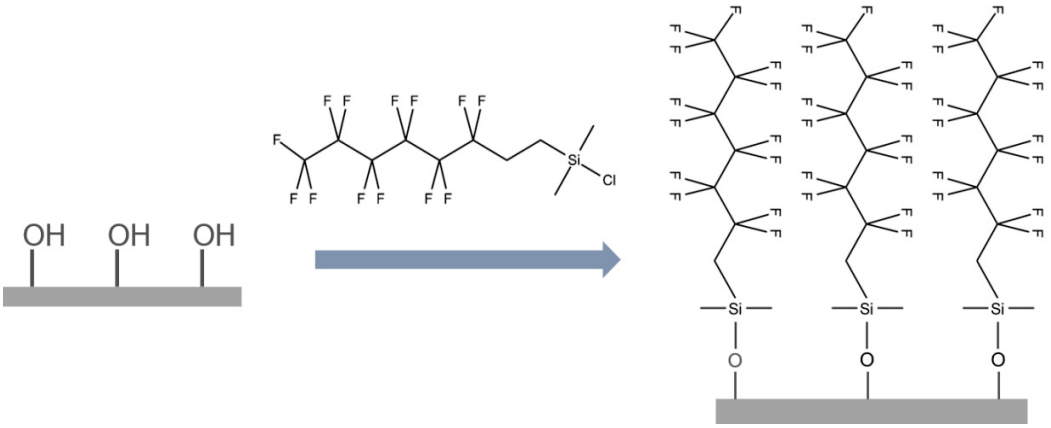

Figure 5.2 Schematic representation of silanization on GLAD film by (1H, 1H, 2H, 2H-perfluorooctyl) dimethylchlorosilane.

5.2.4 Sample preparation coupled with offline SMALDI-MS

Figure 5.3a demonstrates the workflow of the sample preparation and detection. Pooled human serum sample (Innovative Research, MI) was first premixed with methanol and C18 beads for 1 min, to precipitate proteins and extract lipids, respectively. C18 was suspended in methanol at the density 0-10% (weight/voltume) and the volume ratio of serum to C18 suspended methanol was 1:3. 25 μL premixed sample was then prepared on-chip (Figure 5.3b). The precipitated proteins

and C18 beads was separated from the liquid phase by the filter inserted under 1500 rpm for 2 min. The supernatant containing the analytes was transferred into the two-level reservoir 3. The disc was then removed from the spinner and placed in a vacuum chamber to dry the supernatant for 20 min. After the sample was dried, 15 μL aqueous suspensions of silica nanoparticles, whose density ranged from 0 to 0.25% (weight/volume), was added through reservoir 2 to re-dissolve the dried sample and mixed by spin-stop cycles for 3 min. The silica nanoparticles adsorbed the remaining proteins in the sample and were separated from the solution by 2000 rpm centrifugation for 5 min, pelleted in the small collection region. 10 μL cleaned sample is pipetted out and acidified with 1μL 2 M HCl to reach a final concentration of 0.18 M HCl. A 1.8 μL sample was then spotted onto a SMALDI-chip in a petri dish and dried at 4 ℃ overnight for salt crystallization.

The SMALDI-chip with dried sample spots was attached to a customized MALDI plate with a double-sided conductive carbon tape (Electron Microscopy Sciences). The MALDI plate was inserted into an AB Sciex Voyager Elite MALDI-TOF mass spectrometer for analysis. A pulsed nitrogen laser (337 nm, 3 ns pulse) was employed for desorption and ionization. Mass spectrum was acquired in negative mode and the signals were average by 100 laser shots, while rastering the beam to fresh locations within the spot. The laser intensity for desorption and ionization was set to 2200 (a.u.) for C18 optimization and 2100 for other measurement. Other detailed instrument settings are summarized in Table 5.1, using previously optimized conditions[185].

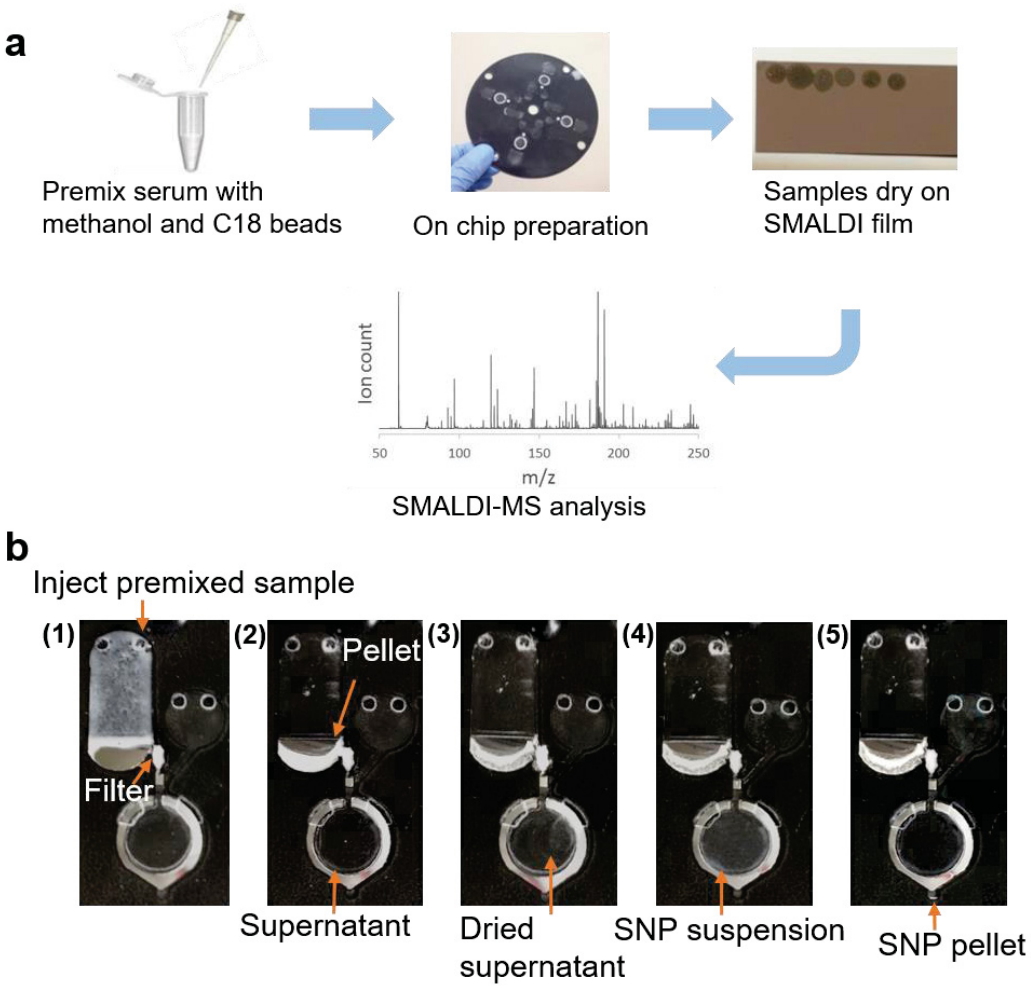

Figure 5.3 (a) Work flow of on-chip sample preparation and analysis of metabolites by SMALDI-MS. (b) Images of on-chip preparation steps: (1) Inject serum samples premixed with methanol and C18 beads. (2) Pellet proteins and C18 beads by centrifugation and filtration. (3) Dry the supernatant by placing the disc in a vacuum chamber. (4) Add silica nanoparticles (SNP) suspension to dissolve the dried sample and adsorb remaining proteins in the sample. (5) Remove SNP by centrifugation.

Table 5.1 Setting of MALDI-TOF-MS in negative mode

Mode of operation	Extraction mode	Accelerating voltage	Grid voltage	Guide wire	Delay time
Reflector	delayed	18 kV	73%	0.05%	150 ns

5.2.5 Sample preparation by ultrafiltration and methanol precipitation

Centrifugal ultrafiltration tubes (Amicon Ultra-4, 3K Da cut-off) were purchased from EmdMillipore for deproteinating human serum. The tube was first rinsed with 4 mL deionized water under 4°C and 4000 g on a lab centrifuge (Allegra X-22, Beckman Coulter) with a swing bucket rotor for 10 min to eliminate glycerol on the membrane. The human serum sample was deproteinated using the rinsed tube under the same condition mentioned above for 30 min. The ultrafiltered sample was acidified with HCl to reach a final concentration of 0.18 M HCl and then spotted on a SMALDI-chip for drying and MS analysis. The laser intensity for desorption and ionization was set to 2100 or 2000.

Methanol precipitation was achieved by mixing serum sample with cold methanol with a volume ratio 1:3 for 5 min, followed by 10,000 RPM in a centrifuge (Sanyo MSE Micro Centaur) for 3 min to pellet the precipitated proteins. The supernatant was transferred into a micro centrifuge tube for drying under vacuum. The dried sample was reconstituted with deionized water to the original supernatant volume. 10 μL sample was then acidified by 1 μL 2 M HCl to contain 0.18 M HCl and analyzed on a SMALDI-chip with the same procedure described in 5.2.4.

5.3 Results and discussion

5.3.1 Sample preparation assay development for serum clean-up

To provide a comparison for the sample workup provided by the microfluidic device, we first explored the sample preparation assay to remove proteins and lipids from serum samples. A widely used clean-up method for metabolomics in serum uses methanol precipitation of protein, followed by chloroform extraction[286]. Methanol replaces the water around the protein molecule and decreases its solvation layer, inducing protein aggregation by the increased electrostatic and dipole-dipole forces. Liquid-liquid extraction is then normally employed, by adding chloroform to extract hydrophobic molecules from the sample. The aqueous phase is then analyzed.

As organic solvents with low polarity such as chloroform can cause severe damage to the microfluidic device by dissolving the toners, we replaced the liquid-liquid extraction with solid phase extraction by using C18 beads. C18 beads suspended in methanol were mixed with serum with a volume ratio of 3:1 for protein precipitation and extraction. The required particle density (concentration) of C18 suspended in methanol was investigated and optimized off chip. The supernatant, after mixing of serum, methanol and C18 beads, was collected, dried under vacuum and re-dissolved with the same volume of water for SMALDI-MS detection. Sample preparation with four different densities of C18 beads was performed and the sample spots on SMALDI-chips were observed under microscope. Figure 5.4 shows spots from the sample preparation with 0 and 1.7% C18 (Figure 5.4a and 5.4b) are larger than the sample spots prepared with higher density C18. The contact angle of the samples prepared with less C18 is smaller, since the hydrophobic molecules in serum, such as lipids, are not completely removed, resulting in more spreading of the spot. Additionally, the sample spots are cleaner and background electrolyte crystallization is

localized in larger crystals, allowing better mass spectrometry of the metabolites as more C18 is used. The signal to noise ratio (SNR) of six different metabolites which were identified previously[185] was obtained by SMALDI-MS to evaluate the sample preparation performance with different densities of C18 beads, as presented in Figure 5.5. Treating samples with C18 beads improves the SNR of aspartic acid, glutamic acid, uric acid and citric acid. A two tailed t-test for each of the four metabolites was used to compare the highest SNR of metabolites in a sample with C18 treatment with the SNR in a sample without C18 treatment. The analysis showed $p < 0.05$ for glutamic acid and aspartic acid and $p < 0.1$ for uric acid and citric acid, confirming the value of the C18 treatment. Samples treated with 3.3% C18 give the highest or second highest SNR for all the metabolites except taurine. Preparations with higher density of C18 suffer from a loss in SNR for these metabolites. Although 1.7% C18 treatment leads to good results for taurine, uric acid and citric acid, the other three analytes are not detected with high SNR. A two-tailed t-test shows that the SNR of aspartic acid, malic acid and glutamic acid in samples prepared with 3.3% C18 are significantly higher than those in samples prepared with 1.7% C18 ($p < 0.05$). Based on this study, 3.3% C18 was selected for the solid phase extraction step.

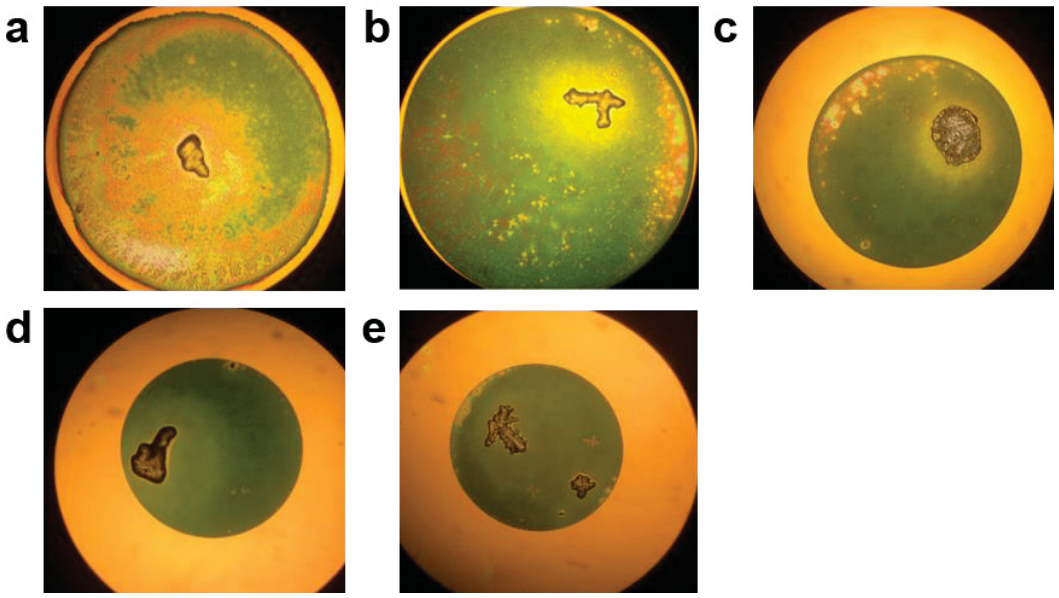

Figure 5.4 Microscopic photos of serum samples prepared with methanol precipitation and solid phase extraction with different densities of beads: (a) 0%; (b) 1.7%; (c) 3.3%; (d) 6.6%; (e) 10%.

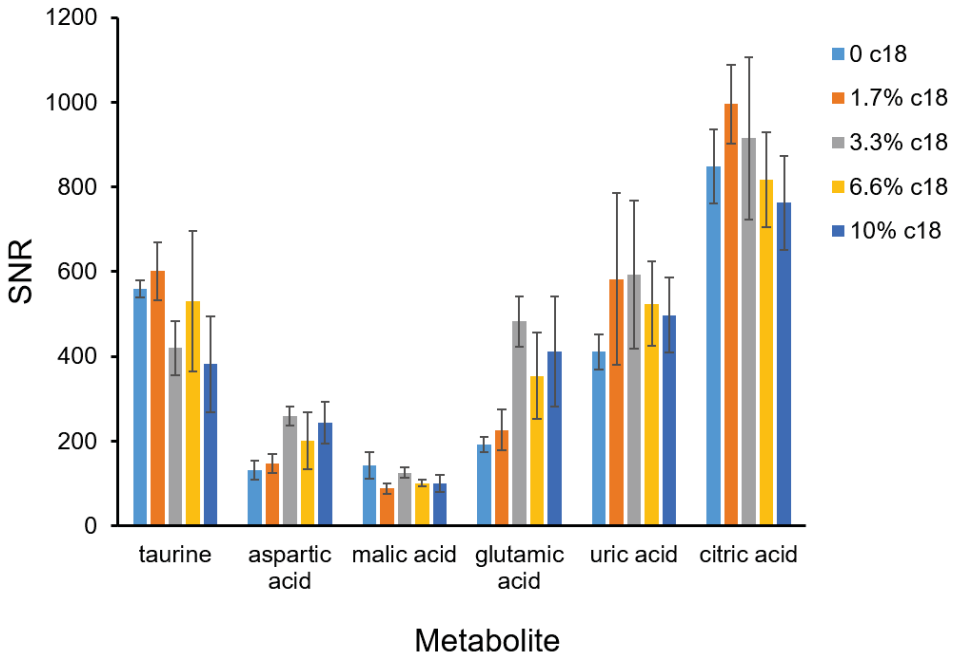

Figure 5.5 Signal to noise ratio of six metabolites from serum samples prepared by methanol

precipitation and C18 beads extraction with different densities.

As methanol precipitation cannot completely remove the proteins in serum[287,288], additional steps may be required to further clean the samples. Silica nanoparticles were selected as a second extraction phase, since they have been reported to adsorb proteins in biofluids such as serum samples[289–292]. Mixing and separation of the nanoparticles was not difficult to realize on a centrifugal microfluidic platform. The effect of the size of the silica nanoparticles on protein adsorption has been studied previously, showing that smaller size nanoparticles with larger surface area adsorb more proteins[289]. In our microfluidic device, it was observed that particles with a diameter less than 200 nm needed too long a time to remove by centrifugation. Conversely, nanoparticles with a diameter larger than 500 nm were difficult to mix in the spin-stop cycles. We thus selected 235 nm silica nanoparticles and evaluated the performance of further protein removal on chip with three different densities. Figure 5.6 illustrates the SNR of six metabolites in samples prepared with different densities of nanoparticles. Compared to preparation without silica nanoparticles, 0.05% silica nanoparticles increase the SNR of all six metabolites, as confirmed by $p < 0.1$ for uric acid and $p < 0.05$ for the other five metabolites, using a two-tailed t-test. However, higher density of silica nanoparticles leads to lower SNR, probably because silica nanoparticles can adsorb some metabolites when protein is absent, as suggested by a previous study[293]. In the presence of proteins, silica nanoparticles are not likely to adsorb metabolites, due to the stronger interactions with proteins than with metabolites[290].

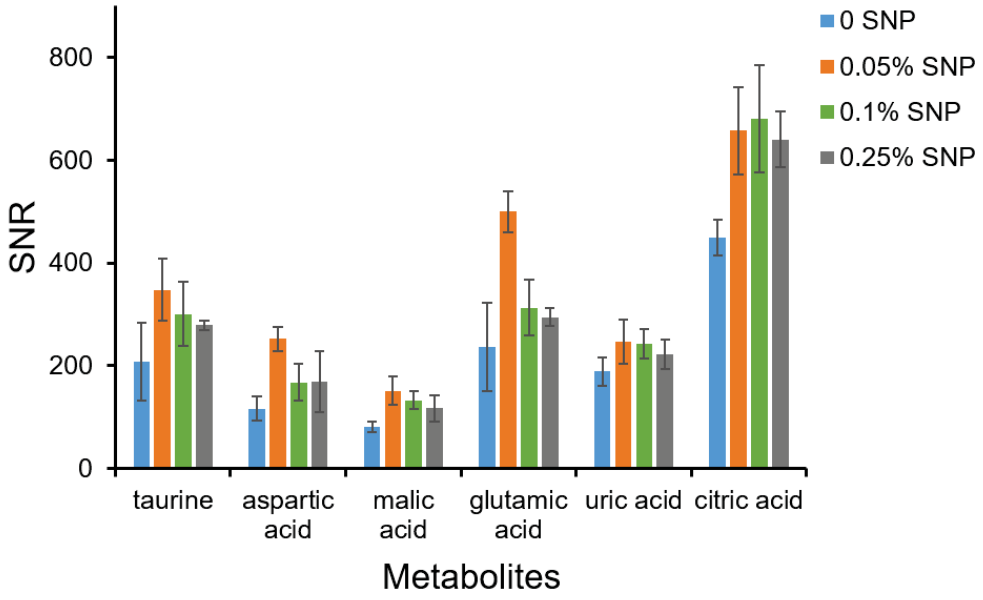

Figure 5.6 Signal to noise ratio of different metabolites from serum samples prepared on-chip with different densities of silica nanoparticles (SNP) to remove proteins after methanol precipitation and C18 beads extraction.

5.3.2 Mass spectrum of on-chip prepared sample

Figure 5.7 illustrates the mass spectra of the serum samples after on-chip preparation with the optimized assays, off-chip ultrafiltration and off-chip methanol precipitation. The identified metabolite [M-H] peaks are labeled with their m/z values. The mass spectrum of the on-chip prepared sample (Figure 5.7a upper trace) gives a flat baseline, little noise and tens of metabolite peaks, which is similar to the spectrum of the ultrafiltered sample (Figure 5.7a middle trace). The lower intensities of the metabolites from on-chip prepared sample compared to the ultrafiltered sample is mainly attributed to dilution in the process of on-chip preparation. The SNR of the six

metabolites in on-chip prepared samples shows an average 48±9% decrease compared to those in ultrafiltered sample. After methanol precipitation and C18 extraction, the sample is about four times diluted and not concentrated again in the following steps. The reduction in signal from the dilution can be expected to cause some increase in the detection limits compared to the ultrafiltration process.

To further evaluate the role of the C18 and silica treatment, a negative control was performed using lab-based methanol precipitation and SMALDI of the aqueous reconstituted serum sample. The spectrum in Figure 5.7a lower trace, shows a poor baseline, large background peaks and low SNR for analytes, presumably due to the incomplete removal of proteins and lipids. For example, a large decrease in the SNR of glutamic acid (76%), aspartic acid (60%) and malic acid (38%) is observed. There are clusters of background peaks with strong intensities in different m/z regions such as 170-175, 185-190 and 200-205, which may be identified as false positive metabolite peaks (Figure 5.7b). Those peaks are less significant in the mass spectra of the samples prepared on-chip with solid phase extraction steps, or by ultrafiltration. Some of the putative metabolite peaks in those m/z regions, such as peaks at m/z 186.0, 187.0 and 188.0, may be buried in the background peaks or suppressed because of a competition for ionization in samples treated by methanol alone.

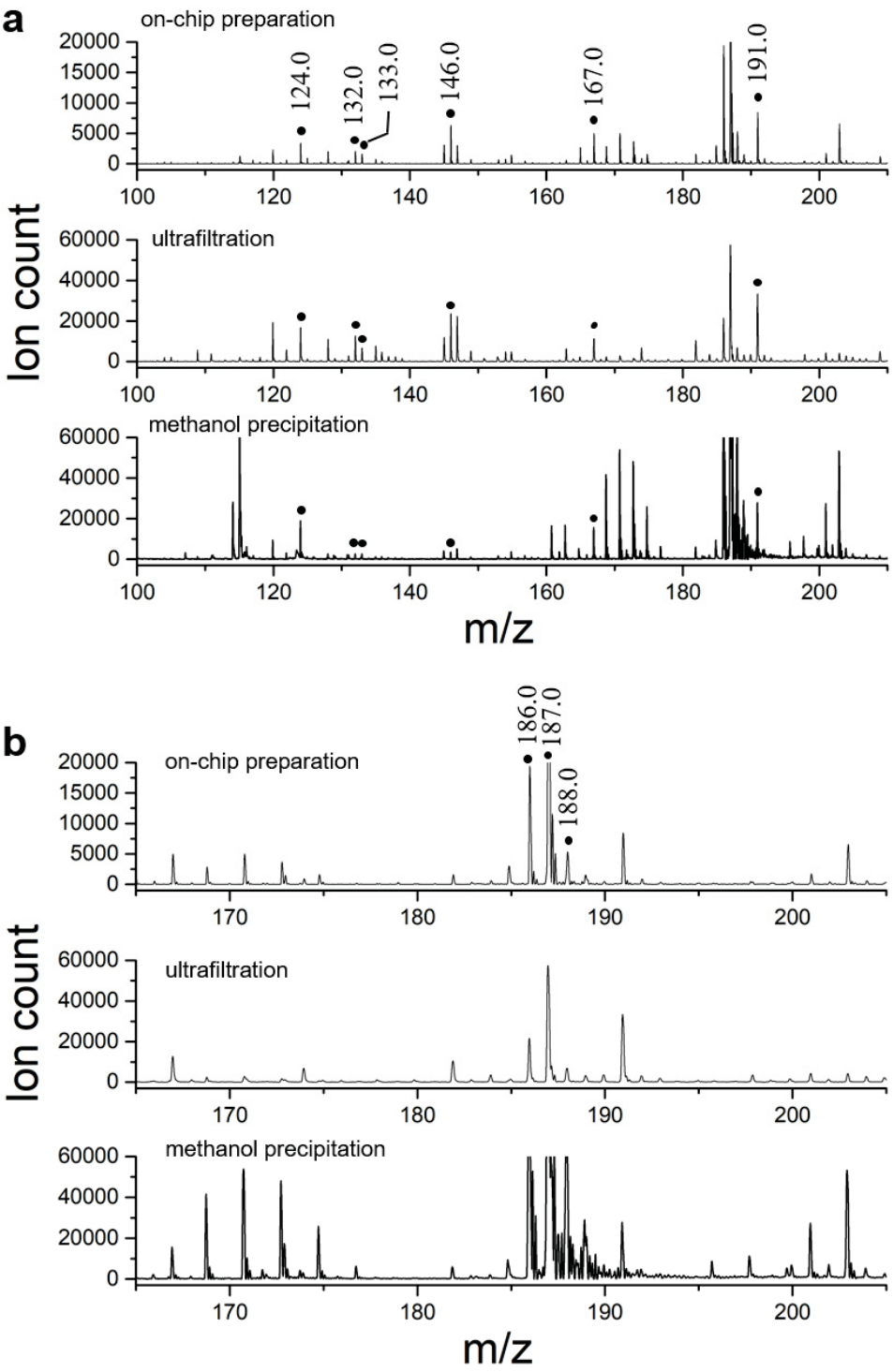

Figure 5.7 Mass spectrum (negative mode) of serum sample after on-chip preparation with labeled peaks (taurine: 124.0; aspartic acid: 132.0; malic acid: 133.0: glutamic acid: 146.0; uric

acid: 167.0; citric acid: 191.0), off-chip ultrafiltration and off-chip methanol precipitation in the mass range of 100-210 (a) and 165-215 (b).

5.3.3 Reproducibility

The robustness of the sample preparation method was assessed according to the reproducibility of the signals for the metabolites. Six parallel sample preparation experiments were performed in separate microfluidic units on two discs. Each disc contained three microfluidic units. The intensity of each metabolite from each unit was compared, as demonstrated in Figure 5.8a. The reproducibility of aspartic acid, malic acid, glutamic acid and uric acid are much better, with the relative standard deviation (RSD) much smaller, compared to taurine and citric acid (Table 5.2). Taurine and citric acid within one disc shows better reproducibility compared to disc-disc reproducibility, as shown in Figure 5.8. The poor reproducibility of those two metabolites might be caused by the less precise control of the manual operations such as reagent loading and mixing with beads in each run. For example, as the analytes have interactions with C18 and silica beads, the concentration of the analytes remaining in solution could be affected by the mixing time of the sample with those beads and the amount of beads added. Besides, the samples prepared in each disc were spotted on separate SMALDI-chips for drying and detection. The differences of the substrates and the operating conditions during sample drying and MS detection may affect the ionization efficiency of the analytes for detection and so cause less reproducible results. The signals of the other four metabolites may be less dependent on the sample processing conditions, so that better reproducibility was obtained.

To improve the reproducibility of the metabolites, internal standards, with similar physical and chemical properties to analytes, are usually added to samples to correct the loss of analytes in the process of sample preparation. The relative intensity of the analyte to the internal standard signal is less influenced by the variation generated by sample preparation and thus gives better reproducibility. Here, many endogenous metabolites in human serum have already been identified and can serve as internal standard for other analytes without the need to spike. We chose citric acid as an internal standard for taurine and the ratio of taurine/citric acid was evaluated from each run. Compared to the signal of taurine with no reference to an internal standard, the relative signal of taurine to citric acid demonstrates better reproducibility, shown in Figure 5.8b, with a decreased RSD from 40% to 18%. Similarly, malic acid is selected as the internal standard for citric acid (Figure 5.8c) and the RSD of the relative signal of citric acid to malic acid is 15% compared to 26% from the signal of citric acid without internal standard. The reproducibility of the six metabolites based on relative intensity of an internal standard are summarized in Table 5.2. However, given their chemical differences, there is no single metabolite that is a satisfactory internal standard for all six metabolites. For example, the relative intensity of citric acid and taurine to glutamine show larger RSD (20% and 35%) than that of citric acid to malic acid (15%) and taurine to citric acid (18%). Using malic acid as internal standard, the RSDs of the relative intensity for glutamic acid, aspartic acid, taurine and uric acid were also larger (Table 5.2), even though the reproducibility of citric acid is improved.

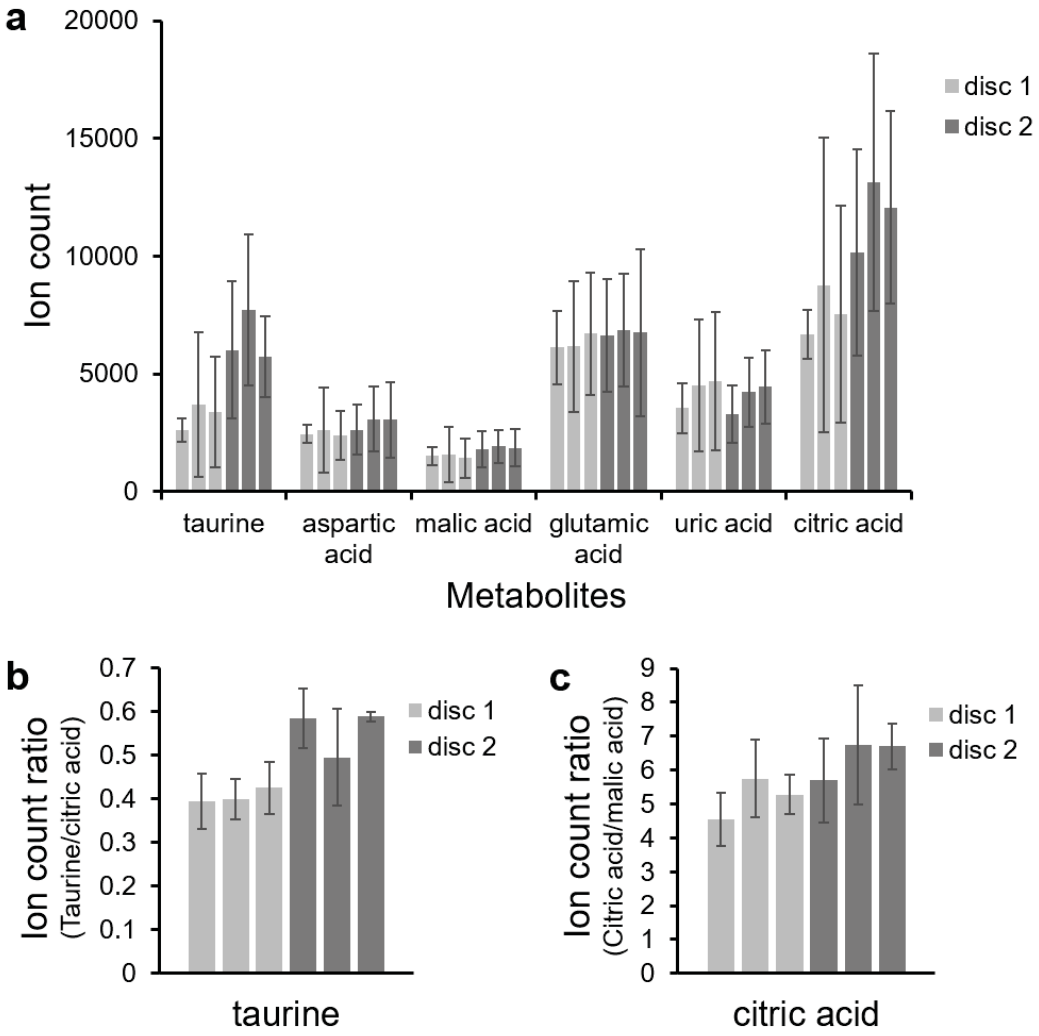

Figure 5.8 Reproducibility of on-chip prepared serum samples.

Six identical microfluidic units in two disc were used for parallel preparation. The results from the three units in disc 1 are represented in light grey and the results from the three units in disc 2 are represented in dark grey. (a) Ion count reproducibility of six different metabolties. (b) Reproducibility of taurine based on relative intensity with citric acid as internal standard. (c) Reproducibility of citric acid based on relative intensity with malic acid as internal standard.

Table 5.2 Relative standard deviation (RSD) of the metabolites in the assessment of reproducibility based on ion count and relative intensity.

Metabolite (m/z)	RSD		
	Ion count	Relative intensity[1] (reference metabolite)	Relative intensity (malic acid)
Taurine (124.0)	40%	18% (citric acid)	30%
Aspartic acid (132.0)	11%	4% (glutamine[2])	9%
Malic acid (133.0)	12%	9% (aspartic acid)	-
Glutamic acid (146.0)	5%	7% (glutamine)	18%
Uric acid (167.0)	14%	12%(glutamine)	21%
Citric acid (191.0)	26%	15% (malic acid)	15%

[1] Relative intensity is the intensity ratio of metabolite and reference metabolite (internal standard)

[2] m/z of glutamine is 145.0

5.3.4 Response to spiked sample

Serum samples spiked with three metabolites, 400 μM glutamic acid, 100 μM aspartic acid and 200 μM citric acid, were prepared on chip to evaluate whether significant losses of analytes exist during on-chip preparation, compared to spiked samples prepared by off-chip ultrafiltration. Internal standards, endogenous glutamine and malic acid from serum, were used for better reproducibility of those metabolites. Relative intensities of glutamic acid/aspartic acid to glutamine and citric acid to glutamine were evaluated for various sample preparation methods.

Figure 5.9a shows the relative intensities of three metabolites from on-chip prepared serum samples with and without a spike. A 97% signal increase for glutamic acid, 175% increase for aspartic acid and 96% increase for citric acid was observed. The relative signal changes for spiked metabolites in serum prepared by the on-chip method were then compared to those in serum

prepared by ultrafiltration. Three-fold diluted serum samples, in which the metabolites are at similar concentrations as on-chip prepared samples, demonstrate comparable signal intensity ratios and changes as for spiked on-chip preparations. There was a 129% increase for glutamic acid, 166% increase for aspartic acid and 91% increase on citric acid, as shown in Figure 5.9b.

Without dilution, serum samples prepared by ultrafiltration (Figure 5.9c) demonstrate comparable relative signal intensity changes to the on-chip prepared samples on glutamic acid (117% increase) and aspartic acid (135% increase). However, the relative intensity of citric acid increases by only 50% in a spiked sample. With the same instrument settings for the mass spectrometer, signals of the metabolites from the ultrafiltered serum shows much higher intensities than the corresponding signals from the on-chip prepared serum. This issue was discussed above in section 5.3.2 and Figure 5.7, and was attributed to the higher concentration in the ultrafiltered sample without any dilution. The absolute intensity (ion count) of citric acid in ultrafiltered sample after spiking is ~ 50,000 which is close to the saturation limit of the instrument, accounting for the apparent decrease in sensitivity.

The problem with signal saturation for un-diluted serum samples may also be addressed by adjusting the laser operating parameters. When the laser intensity is lowered we see a 143% increase for glutamic acid, 156% increase for aspartic acid and 134% increase for citric acid, as shown in Figure 5.9d. Although on-chip prepared samples can lead to decreased signals due to dilution, both preparation methods show similar signal changes for the spiked analytes. The results indicate that on-chip preparation does not result in a significant losses of analytes compared to off-chip ultrafiltration. The results confirm the ability to perform quantitative analysis of some metabolites by using the on-chip preparation method.

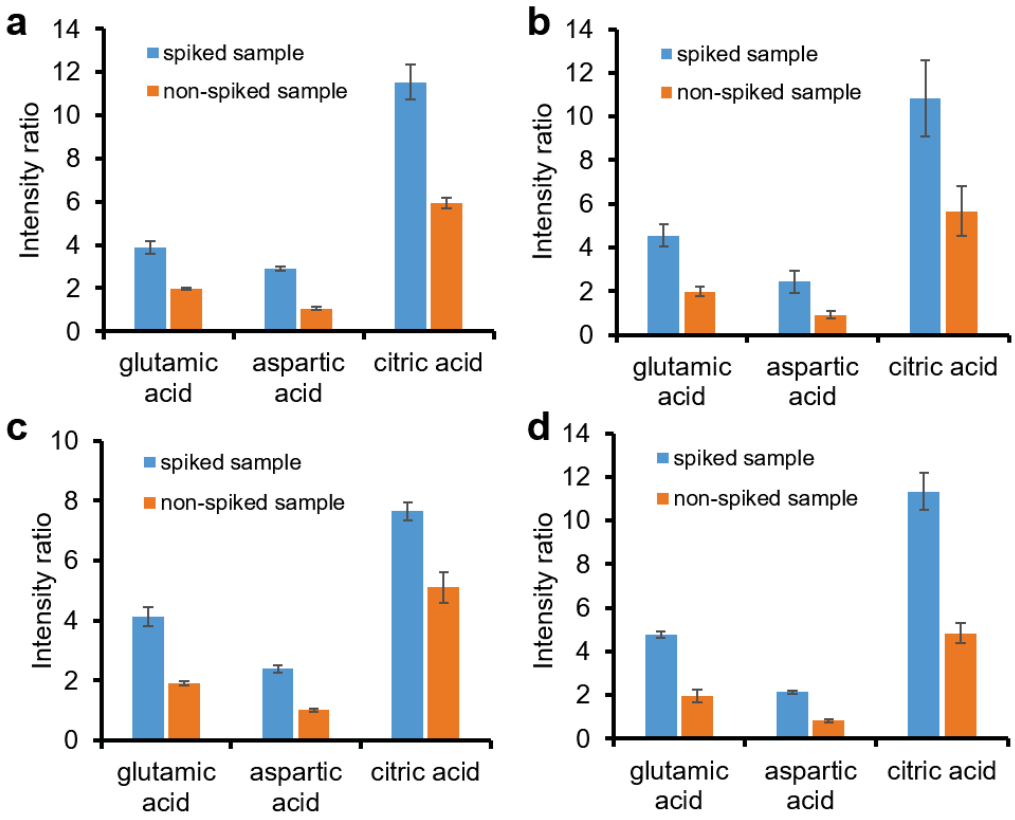

Figure 5.9 Comparison of signal response on spiked glutamic acid, aspartic acid and citric acid with microfluidic preparation (a) and ultrafiltration (b-d).

Endogenous glutamine and malic acid from serum are used as internal standards for glutamic acid/aspartic acid and citric acid, respectively. Intensity ratios denote intensity of glutamic acid to glutamine, aspartic acid to glutamine and citric acid to malic acid. Serum with or without spiked 400 μM glutamic acid, 100 μM aspartic acid and 200 μM citric acid were prepared. (b) Serum with or without spiked amino acid were diluted to 1/3 and then prepared. (c) Serum with or without spiked amino acid were prepared without dilution. (d) Serum with or without spiked amino acid were prepared without dilution but detected using a lower laser intensity for desorption and ionization.

5.3.5 Quantification of several metabolites

Glutamic acid, aspartic acid and citric acid in serum samples prepared on chip were quantified by a standard addition method. Endogenous glutamine in serum was selected as an internal standard for glutamic acid and aspartic acid, while endogenous malic acid served as the internal standard for and citric acid. The calibration curve for each metabolite was plotted as intensity ratio *vs.* concentration of standard (Figure 5.10). The results of quantification are summarized in Table 5.3, together with results obtained from a metabolite database, as well as those from previous analysis of serum prepared by ultrafiltration then quantified by SMALDI-MS or NMR. The results of glutamic acid and aspartic acid, 281.0 μM and 43.2 μM were consistent with those from other preparation and quantification methods. The much higher concentration of these two amino acids, as compared to the results from database, might be owing to the hydrolysis of glutamine and asparagine in the sample. Citric acid was not quantified by other methods from our previous work, but the result of centrifugal disc-SMALDI-MS, 180.9 μM, is in the range from the Human Metabolome Database.

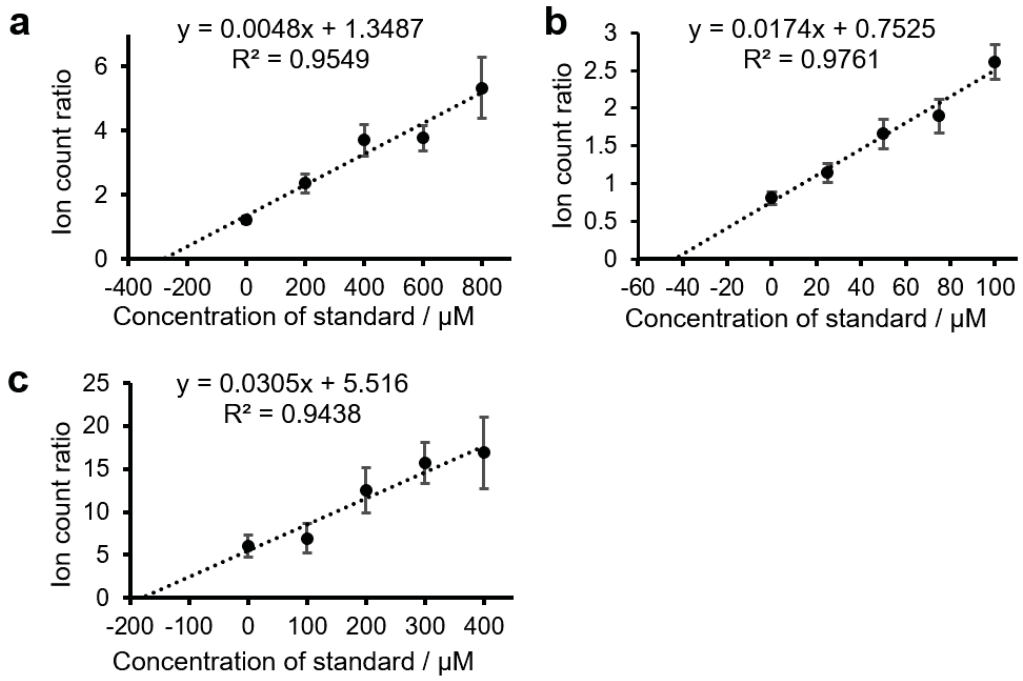

Figure 5.10 Calibration curves of (a) glutamic acid, (b) aspartic acid and (c) citric acid in serum samples prepared by centrifugal microfluidic disc and detected on SMALDI-chip. Standard addition method was employed for quantitative analysis. Intensity ratio in each calibration curve is glutamic acid/glutamine (a), aspartic acid/ glutamine (b) and citric acid/malic acid (c).

Table 5.3 Comparison of the quantitative results of three metabolites in human serum samples prepared and quantified by centrifugal microfluidic disc-SMALDI-MS, ultrafiltration-SMALDI-MS and ultrafiltration-NMR.

	Concentration in original serum sample /μM			
	Centrifugal disc-SMALDI-MS	Ultrafiltration-SMALDI-MS[1]	Ultrafiltration-NMR[2]	Database[3]
Glutamic acid	281.0	353.2	261.5	<100
Aspartic acid	43.2	55.3	62.7	<25
Citric acid	180.9	N/A	N/A	50-200; 30-400

[1, 2] Data from reference 185.

[3] Data from Human Metabolome database (HMDB, www.hmdb.ca).

5.4 Conclusion

In this chapter, we present a centrifugal microfluidic platform to prepare human serum samples for metabolites analysis on mass spectrometry. Methanol precipitation and C18 beads extraction were utilized to remove proteins and lipids, respectively. Further protein cleaning was achieved by silica nanoparticles adsorption and the whole sample preparation assay was optimized to obtain large SNR of six identified metabolites. The protein and lipid free sample after the established on-chip preparation demonstrated clean sample spot on the SMALDI-chip where salts from the sample were well crystalized in the process of drying. The mass spectrum after on-chip preparation was cleaner with less noise and lower background peaks than the serum sample treated with only methanol. The reproducibility of the on-chip preparation was assessed based on the signals of the six metabolites in the mass spectrum. Two of the metabolites, taurine and citric acid, were less

reproducible than the other four metabolites and it is likely because of the less precise controlled operations that are completed manually. The reproducibility is improved by using relative signal intensity instead of absolute intensity. Aspartic acid and glutamic acid, which showed the best reproducibility among the six, were spiked in human serum and detected after on-chip preparation to compare with ultrafiltered sample. The signals from on-chip prepared samples showed comparable fold of signal change on the spiked metabolites with those from ultrafiltered samples. The two amino acids and citric acid were quantified by a standard addition method and the quantitative results are also consistent with other sample preparation and quantification methods or database values.

Chapter 6. Conclusion and future work

6.1 Microfluidic cell sorting system for directed evolution

This thesis has demonstrated two microfluidic platforms to solve biochemical problems. Microfluidic techniques offer many potential advantages such as high throughput, low cost, automation, and low sample consumption, which offer the possibility to accelerate directed evolution of functional proteins and to prepare complex samples for small molecule analysis. In Chapter 2, characterization of the performance of our previously developed μFACS with a single-point detection system were presented. The collection efficiency of the system with the piezoelectric actuator was evaluated and optimized to reach a maximal < 40% under the operating condition of ≥ 10.5 μL/min for the directed evolution of the fluorescent protein sensor Y-GECOs. We then studied the effect of cellular heterogeneity of expression level on the directed evolution, by measuring the fluorescence of single cells expressing each of three variants of Y-GECO with different inherited brightness. The results revealed broad distributions of single cell expression of each variant with large overlapping regions, which could lead to false positives and false negatives during the screening. The three distributions from those three variants can be partially distinguished by the high fluorescence regions of each distribution. Potential solutions to the problem of false positives and false negatives were discussed, including utilizing a second agar plate-based screening step to measure colonies, or increase the throughput while lowering the threshold for selection.

In an effort to explore microfluidic cell sorters with enhanced performance for directed evolution, we introduced a novel μFACS with a two-point detection system based on the previous design in

Chapter 3. The two-point detection allows examination and improvement of two critical parameters of FP-based sensors, brightness and analyte-dependent fluorescence change. By using the two point detector for a two parameter screen we enhanced the process of directed evolution. The new system also features several other improvements. For instance, a simple 3D focusing flow was realized to reduce the variation of the travel time between the two detectors and so enhance the pair matching. The laser beam for fluorescence excitation was linearly expanded to achieve a more uniform distribution of its intensity. A higher collection efficiency (~ 85%) was obtained with a 3D focusing flow combined with a relatively lower flow rate (5.25 μL/min), compared to the previous < 40% collection with 2D focusing flow using a higher flow rate (10.5 μL/min). The improved μFACS demonstrated superior performance, evolving the sensor Y-GECO1f, even though it was operated at a moderate throughput (10 cells/s). The directed evolution on the basis of μFACS led to an optimized variant Y-GECO2f with higher brightness, larger fluorescence change and fast dissociation kinetics. In Chapter 4, rational design was conducted as three mutations were introduced at specific positions to modify the binding constant of Y-GECO2f and Y-GECO1m, resulting in a series of variants with different binding constant ranging from 25 nM to 2.5 μM. The variants were then expressed for characterization in various mammalian cells and tissues, where fluorescence change of the sensors induced by cellular Ca^{2+} change was monitored.

While the μFACS system has been greatly enhanced for directed evolution, there still remain challenges to be addressed in future work. Firstly, our study reveals that single cell expression is highly heterogeneous, which exerts a negative impact on the screening. Secondly, our μFACS is mainly designed for FP sensors which have been optimized to have moderate brightness. It might be difficult to screen FP sensors at the early stage of protein engineering when their brightness is too low to be detected. To solve these problems, droplet microfluidic techniques might be

employed so that single cells are first cultured to form micro-colonies before screening to amplify the fluorescence signals and minimize the heterogeneous expression in single cells.

Another limitation with the current μFACS with two-point detection system is the relatively low throughput, which is restricted by the pair-matching accuracy. Developing a new device with more precise cell flow rate would reduce the variation of the travel velocity. One possibility here is to fabricate devices with deeper channels, more closely matched to the channel width. This would allow a higher flow rate in the vertical direction, further narrowing the sheath flow for the cells and further reducing the velocity variation they experience due to laminar flow conditions. Alternatively, a device that can arrange cells with a more uniform distribution along the flow would improve pair-matching at high throughput. For instance, standing surface acoustic waves have been employed for 3D cell focusing in a microfluidic cell sorter, where cells were distributed with good uniformity[294]. Another approach to the enhanced pair-matching at high throughput is to match cell pairs based on not only the travel time but also another characteristic of the cells. A specific example is to express another FP together with the sensors for evolving in each cell and use the signal intensities of the first FP for matching. As a significant cellular heterogeneity of expression level exists, cells which enter the same time window for matching can be distinguished by the fluorescence of the FP. Notably, the FP used for matching should have a fluorescence signal that is constant during the screening and its spectrum cannot largely overlap with that of the sensors being evolved.

The versatility of microfluidic techniques enables researchers to build up novel μFACS systems to screen other characteristics of FP-based sensors. The Palmer group has demonstrated μFACS to measure photobleaching rate and fluorescence lifetime of FPs[65,68,69], but we can only collect a

limited number of types of data from the current systems. Inventing new platforms is desirable to measure and improve other parameters of FPs and FP-based sensor, e.g association/dissociation kinetics, binding constant, and two-photon excitation cross section.

6.2 Centrifugal microfluidic sample preparation platform

In Chapter 5, a centrifugal microfluidic sample preparation device was demonstrated for metabolomic analysis. Human serum sample was successfully cleaned of interfering biochemical on-chip by utilizing methanol precipitation and solid phase extraction to remove proteins and lipids. Specific designs were generated to realize on-chip filtration, sample drying and mixing. The protein and lipid free sample obtained from sample preparation was then transferred to a SMALDI-chip to segregate salts from the background electrolytes by crystallization during sample drying. SMALDI-MS was conducted on the sample spots and a number of signals of metabolites could be obtained. Reproducibility of the established on-chip preparation was studied by evaluating six metabolites which were previously identified. Two of them showed poor reproducibility, whereas signals of the other four analytes were more reproducible. Compared to ultrafiltration, the on-chip preparation demonstrated lower signal peaks under the same laser intensity for desorption and ionization, which is attributed to the dilution of analytes in the process of preparation. The signal change for spiked analytes, aspartic acid and glutamic acid, determined by mass spectrometry after on-chip preparation, was comparable with that from the ultrafiltered samples. Those two amino acids were quantitatively analyzed by standard addition methods and the results were consistent with those from ultrafiltered serum samples.

Our on-chip platform has not achieved fully automated processing on chip, as manual sample mixing was conducted for effective protein precipitation and the disc was manually removed from the motor for sample drying in a vacuum chamber. In order to realize full automation, new microfluidic designs with units for fast on-chip mixing and drying may be explored in future work. Additionally, the centrifugal microfluidic disc is devised to prepare human serum sample not whole blood. Since serum cannot be directly collected from patients, an additional processing step is required. That is, whole blood sample is first allowed to clot, followed by centrifuge to separate blood cells and the clot. Therefore, on-chip whole blood preparation is desired to accomplish a sample cleanup device which can directly collect blood sample from patient and output clean sample ready for analysis. Moreover, the centrifugal disc is designed mainly for metabolomic analysis by SMALDI-MS, but the prepared sample may not satisfy the requirement for other detection techniques. For example, compared to other types of mass spectrometry such as ESI-MS, SMALDI-MS offers the unique function of salt segregation from analytes on SMALDI-chip so that on-chip salt removal is not needed in our current disc. SMALDI-MS has been demonstrated for putative identification of 32 metabolites in human serum[185], the number of which is still very limited. Other analytical instrumentations like ESI-MS and NMR can provide alternative options for profiling and analyzing large numbers of metabolites, but may differ in sample preparation requirement. It is worthwhile to generate microfluidic sample preparation device for various instrumentation which could facilitate the development of metabolomics research and clinical diagnosis.

References

1. Hulett, H. R., Bonner, W. A., Barrett, J. & Herzenberg, L. A. Cell sorting: automated separation of mammalian cells as a function of intracellular fluorescence. *Science* **166,** 747–749 (1969).
2. Ashcroft, R. G. & Lopez, P. A. Commercial high speed machines open new opportunities in high throughput flow cytometry (HTFC). *J. Immunol. Methods* **243,** 13–24 (2000).
3. Kuckuck, F. W., Edwards, B. S. & Sklar, L. A. High throughput flow cytometry. *Cytometry* **44,** 83–90 (2001).
4. Nebe-von-Caron, G., Stephens, P. J., Hewitt, C. J., Powell, J. R. & Badley, R. A. Analysis of bacterial function by multi-colour fluorescence flow cytometry and single cell sorting. *J. Microbiol. Methods* **42,** 97–114 (2000).
5. De Rosa, S. C., Brenchley, J. M. & Roederer, M. Beyond six colors: a new era in flow cytometry. *Nat. Med.* **9,** 112–117 (2003).
6. Kerker, M. Elastic and inelastic light scattering in flow cytometry. *Cytometry A* **4,** 1–10 (1983).
7. De Grooth, B. G., Terstappen, L., Pupples, G. J. & Greve, J. Light-scattering polarization measurements as a new parameter in flow cytometry. *Cytometry A* **8,** 539–544 (1987).
8. Klein, A. M. *et al.* Droplet barcoding for single-cell transcriptomics applied to embryonic stem cells. *Cell* **161,** 1187–1201 (2015).
9. Mazutis, L. *et al.* Single-cell analysis and sorting using droplet-based microfluidics. *Nat. Protoc.* **8,** 870–891 (2013).
10. Zinchenko, A. *et al.* One in a million: flow cytometric sorting of single cell-lysate assays in monodisperse picolitre double emulsion droplets for directed evolution. *Anal. Chem.* **86,** 2526–2533 (2014).

11. Barbulovic-Nad, I., Au, S. H. & Wheeler, A. R. A microfluidic platform for complete mammalian cell culture. *Lab Chip* **10,** 1536–1542 (2010).

12. Brouzes, E. *et al.* Droplet microfluidic technology for single-cell high-throughput screening. *Proc. Natl. Acad. Sci.* **106,** 14195–14200 (2009).

13. Clausell-Tormos, J. *et al.* Droplet-based microfluidic platforms for the encapsulation and screening of mammalian cells and multicellular organisms. *Chem. Biol.* **15,** 427–437 (2008).

14. Pan, J. *et al.* Quantitative tracking of the growth of individual algal cells in microdroplet compartments. *Integr. Biol.* **3,** 1043–1051 (2011).

15. Kintses, B. *et al.* Picoliter cell lysate assays in microfluidic droplet compartments for directed enzyme evolution. *Chem. Biol.* **19,** 1001–1009 (2012).

16. Sanchez-Freire, V., Ebert, A. D., Kalisky, T., Quake, S. R. & Wu, J. C. Microfluidic single-cell real-time PCR for comparative analysis of gene expression patterns. *Nat. Protoc.* **7,** 829–838 (2012).

17. Ottesen, E. A., Hong, J. W., Quake, S. R. & Leadbetter, J. R. Microfluidic digital PCR enables multigene analysis of individual environmental bacteria. *Science* **314,** 1464–1467 (2006).

18. Fu, A. Y., Spence, C., Scherer, A., Arnold, F. H. & Quake, S. R. A microfabricated fluorescence-activated cell sorter. *Nat. Biotechnol.* **17,** 1109–1111 (1999).

19. Schrum, D. P., Culbertson, C. T., Jacobson, S. C. & Ramsey, J. M. Microchip flow cytometry using electrokinetic focusing. *Anal. Chem.* **71,** 4173–4177 (1999).

20. Fiedler, S., Shirley, S. G., Schnelle, T. & Fuhr, G. Dielectrophoretic sorting of particles and cells in a microsystem. *Anal. Chem.* **70,** 1909–1915 (1998).

21. Fu, A. Y., Chou, H.-P., Spence, C., Arnold, F. H. & Quake, S. R. An integrated microfabricated cell sorter. *Anal. Chem.* **74,** 2451–2457 (2002).

22. Wolff, A. *et al.* Integrating advanced functionality in a microfabricated high-throughput fluorescent-activated cell sorter. *Lab Chip* **3,** 22–27 (2003).

23. Yao, B. *et al.* A microfluidic device based on gravity and electric force driving for flow cytometry and fluorescence activated cell sorting. *Lab Chip* **4,** 603–607 (2004).

24. Guo, F. *et al.* Droplet electric separator microfluidic device for cell sorting. *Appl. Phys. Lett.* **96,** 193701 (2010).

25. Wang, L., Flanagan, L. A., Jeon, N. L., Monuki, E. & Lee, A. P. Dielectrophoresis switching with vertical sidewall electrodes for microfluidic flow cytometry. *Lab Chip* **7,** 1114–1120 (2007).

26. Dittrich, P. S. & Schwille, P. An integrated microfluidic system for reaction, high-sensitivity detection, and sorting of fluorescent cells and particles. *Anal. Chem.* **75,** 5767–5774 (2003).

27. Sun, Y., Lim, C. S., Liu, A. Q., Ayi, T. C. & Yap, P. H. Design, simulation and experiment of electroosmotic microfluidic chip for cell sorting. *Sens. Actuators A Phys.* **133,** 340–348 (2007).

28. Puttaswamy, S. V., Sivashankar, S., Yeh, C.-H., Chen, R.-J. & Liu, C. H. Electrodynamically actuated on-chip flow cytometry with low shear stress for electro-osmosis based sorting using low conductive medium. *Microelectron. Eng.* **87,** 2582–2591 (2010).

29. Krüger, J. *et al.* Development of a microfluidic device for fluorescence activated cell sorting. *J. Micromech. Microeng.* **12,** 486 (2002).

30. Chen, P. *et al.* Hydrodynamic gating valve for microfluidic fluorescence-activated cell sorting. *Anal. Chim. Acta* **663,** 1–6 (2010).

31. Ho, C.-T., Lin, R.-Z., Chang, H.-Y. & Liu, C.-H. Micromachined electrochemical T-switches for cell sorting applications. *Lab Chip* **5,** 1248–1258 (2005).

32. Shirasaki, Y. *et al.* On-chip cell sorting system using laser-induced heating of a thermoreversible gelation polymer to control flow. *Anal. Chem.* **78,** 695–701 (2006).

33. Wang, M. M. *et al.* Microfluidic sorting of mammalian cells by optical force switching. *Nat. Biotechnol.* **23,** 83–87 (2005).

34. Wu, T.-H. *et al.* Pulsed laser triggered high speed microfluidic fluorescence activated cell sorter. *Lab Chip* **12,** 1378–1383 (2012).

35. Franke, T., Braunmüller, S., Schmid, L., Wixforth, A. & Weitz, D. A. Surface acoustic wave actuated cell sorting (SAWACS). *Lab Chip* **10,** 789–794 (2010).

36. Cho, S. H., Chen, C. H., Tsai, F. S., Godin, J. M. & Lo, Y.-H. Human mammalian cell sorting using a highly integrated micro-fabricated fluorescence-activated cell sorter (μFACS). *Lab Chip* **10,** 1567–1573 (2010).

37. Ding, X. *et al.* On-chip manipulation of single microparticles, cells, and organisms using surface acoustic waves. *Proc. Natl. Acad. Sci.* **109,** 11105–11109 (2012).

38. Petersson, F., Åberg, L., Swärd-Nilsson, A.-M. & Laurell, T. Free flow acoustophoresis: microfluidic-based mode of particle and cell separation. *Anal. Chem.* **79,** 5117–5123 (2007).

39. Mazutis, L. *et al.* Droplet-based microfluidic systems for high-throughput single DNA molecule isothermal amplification and analysis. *Anal. Chem.* **81,** 4813–4821 (2009).

40. Pekin, D. *et al.* Quantitative and sensitive detection of rare mutations using droplet-based microfluidics. *Lab Chip* **11,** 2156–2166 (2011).

41. Hindson, B. J. *et al.* High-throughput droplet digital PCR system for absolute quantitation of DNA copy number. *Anal. Chem.* **83,** 8604–8610 (2011).

42. Fischlechner, M. *et al.* Evolution of enzyme catalysts caged in biomimetic gel-shell beads. *Nat. Chem.* **6,** 791–796 (2014).

43. Sjostrom, S. L. *et al.* High-throughput screening for industrial enzyme production hosts by droplet microfluidics. *Lab Chip* **14,** 806–813 (2014).

44. Stapleton, J. A. & Swartz, J. R. Development of an in vitro compartmentalization screen for high-throughput directed evolution of [FeFe] hydrogenases. *PLoS One* **5,** e15275 (2010).

45. Miller, O. J. *et al.* High-resolution dose–response screening using droplet-based microfluidics. *Proc. Natl. Acad. Sci.* **109,** 378–383 (2012).

46. Lombardi, D. & Dittrich, P. S. Droplet microfluidics with magnetic beads: a new tool to investigate drug–protein interactions. *Anal. Bioanal. Chem.* **399,** 347–352 (2011).

47. Agresti, J. J. *et al.* Ultrahigh-throughput screening in drop-based microfluidics for directed evolution. *Proc. Natl. Acad. Sci.* **107,** 4004–4009 (2010).

48. Wang, Y. *et al.* Benchtop micromolding of polystyrene by soft lithography. *Lab Chip* **11,** 3089–3097 (2011).

49. Wang, Y. *et al.* Capture and 3D culture of colonic crypts and colonoids in a microarray platform. *Lab Chip* **13,** 4625–4634 (2013).

50. Kim, M., Kim, S. H., Lee, S. K. & Kim, T. Microfluidic device for analyzing preferential chemotaxis and chemoreceptor sensitivity of bacterial cells toward carbon sources. *Analyst* **136,** 3238–3243 (2011).

51. Lim, J. W., Shin, K. S., Moon, J., Lee, S. K. & Kim, T. A Microfluidic Platform for High-Throughput Screening of Small Mutant Libraries. *Anal. Chem.* **88,** 5234–5242 (2016).

52. Chen, B. *et al.* High-throughput analysis and protein engineering using microcapillary arrays. *Nat. Chem. Biol.* (2015).

53. Bessette, P. H., Rice, J. J. & Daugherty, P. S. Rapid isolation of high-affinity protein binding peptides using bacterial display. *Protein Eng. Des. Sel.* **17,** 731–739 (2004).

54. Liu, Y. *et al.* Controlling the selection stringency of phage display using a microfluidic device. *Lab Chip* **9,** 1033–1036 (2009).

55. McCafferty, J., Griffiths, A. D., Winter, G. & Chiswell, D. J. Phage antibodies: filamentous phage displaying antibody variable domains. *Nature* **348,** 552 (1990).

56. Clackson, T. & Hoogenboom, H. R. Making antibody fragments using phage display libraries. *Nature* **352,** 624 (1991).

57. Shamah, S. M., Healy, J. M. & Cload, S. T. Complex target SELEX. *Acc. Chem. Res.* **41,** 130–138 (2008).

58. Daniels, D. A., Chen, H., Hicke, B. J., Swiderek, K. M. & Gold, L. A tenascin-C aptamer identified by tumor cell SELEX: systematic evolution of ligands by exponential enrichment. *Proc. Natl. Acad. Sci.* **100,** 15416–15421 (2003).

59. Stoltenburg, R., Reinemann, C. & Strehlitz, B. SELEX—a (r) evolutionary method to generate high-affinity nucleic acid ligands. *Biomol. Eng.* **24,** 381–403 (2007).

60. Granieri, L., Baret, J.-C., Griffiths, A. D. & Merten, C. A. High-throughput screening of enzymes by retroviral display using droplet-based microfluidics. *Chem. Biol.* **17,** 229–235 (2010).

61. Baret, J.-C. *et al.* Fluorescence-activated droplet sorting (FADS): efficient microfluidic cell sorting based on enzymatic activity. *Lab Chip* **9,** 1850–1858 (2009).

62. Gielen, F. *et al.* Ultrahigh-throughput–directed enzyme evolution by absorbance-activated droplet sorting (AADS). *Proc. Natl. Acad. Sci.* **113,** E7383–E7389 (2016).

63. Fallah-Araghi, A., Baret, J.-C., Ryckelynck, M. & Griffiths, A. D. A completely in vitro ultrahigh-throughput droplet-based microfluidic screening system for protein engineering and directed evolution. *Lab Chip* **12,** 882–891 (2012).

64. Miller, O. J. *et al.* Directed evolution by in vitro compartmentalization. *Nat. Methods* **3,** 561–570 (2006).

65. Lubbeck, J. L., Dean, K. M., Ma, H., Palmer, A. E. & Jimenez, R. Microfluidic Flow Cytometer for Quantifying Photobleaching of Fluorescent Proteins in Cells. *Anal. Chem.* **84,** 3929–3937 (2012).

66. Ma, H., Gibson, E. A., Dittmer, P. J., Jimenez, R. & Palmer, A. E. High-throughput Examination of FRET-detected Metal-Ion Response in Mammalian Cells. *J. Am. Chem. Soc.* **134,** 2488 (2012).

67. Davis, L. M., Lubbeck, J. L., Dean, K. M., Palmer, A. E. & Jimenez, R. Microfluidic cell sorter for use in developing red fluorescent proteins with improved photostability. *Lab Chip* **13,** 2320–2327 (2013).

68. Dean, K. M. *et al.* Microfluidics-based selection of red-fluorescent proteins with decreased rates of photobleaching. *Integr. Biol.* **7,** 263–273 (2015).

69. Dean, K. M. *et al.* High-speed multiparameter photophysical analyses of fluorophore libraries. *Anal. Chem.* **87,** 5026–5030 (2015).

70. Fiedler, B. L. *et al.* Droplet Microfluidic Flow Cytometer for Sorting on Transient Cellular Responses of Genetically-Encoded Sensors. *Anal. Chem.* (2016).

71. Zhao, Y. *et al.* Microfluidic cell sorter-aided directed evolution of a protein-based calcium ion indicator with an inverted fluorescent response. *Integr. Biol.* **6,** 714–725 (2014).

72. Ormo, M., Cubitt, A. B., Kallio, K. & Gross, L. A. Crystal structure of the Aequorea victoria green fluorescent protein. *Science* **273,** 1392 (1996).

73. Tsien, R. Y. The green fluorescent protein. *Annu. Rev. Biochem.* **67,** 509–544 (1998).

74. Shimomura, O., Johnson, F. H. & Saiga, Y. Extraction, purification and properties of aequorin, a bioluminescent protein from the luminous hydromedusan, Aequorea. *J. Cell. Comp. Physiol.* **59,** 223–239 (1962).

75. Lemay, N. P. *et al.* The role of the tight-turn, broken hydrogen bonding, Glu222 and Arg96 in the post-translational green fluorescent protein chromophore formation. *Chem. Phys.* **348,** 152–160 (2008).

76. Heim, R., Prasher, D. C. & Tsien, R. Y. Wavelength mutations and posttranslational autoxidation of green fluorescent protein. *Proc. Natl. Acad. Sci.* **91,** 12501–12504 (1994).

77. Cubitt, A. B. *et al.* Understanding, improving and using green fluorescent proteins. *Trends Biochem. Sci.* **20,** 448–455 (1995).

78. Reid, B. G. & Flynn, G. C. Chromophore formation in green fluorescent protein. *Biochemistry* **36,** 6786–6791 (1997).

79. Barondeau, D. P., Putnam, C. D., Kassmann, C. J., Tainer, J. A. & Getzoff, E. D. Mechanism and energetics of green fluorescent protein chromophore synthesis revealed by trapped intermediate structures. *Proc. Natl. Acad. Sci.* **100,** 12111–12116 (2003).

80. Rosenow, M. A., Huffman, H. A., Phail, M. E. & Wachter, R. M. The Crystal Structure of the Y66L Variant of Green Fluorescent Protein Supports a Cyclization− Oxidation− Dehydration Mechanism for Chromophore Maturation†. *Biochemistry* **43,** 4464–4472 (2004).

81. Olenych, S. G., Claxton, N. S., Ottenberg, G. K. & Davidson, M. W. The fluorescent protein color palette. *Curr. Protoc. Cell Biol.* (2007).

82. Chudakov, D. M. *et al.* Photoswitchable cyan fluorescent protein for protein tracking. *Nat. Biotechnol.* **22,** 1435–1439 (2004).

83. Shaner, N. C. *et al.* Improved monomeric red, orange and yellow fluorescent proteins derived from Discosoma sp. red fluorescent protein. *Nat. Biotechnol.* **22,** 1567–1572 (2004).

84. Matz, M. V. *et al.* Fluorescent proteins from nonbioluminescent Anthozoa species. *Nat. Biotechnol.* **17,** 969–973 (1999).

85. Wiedenmann, J. *et al.* A far-red fluorescent protein with fast maturation and reduced oligomerization tendency from Entacmaea quadricolor (Anthozoa, Actinaria). *Proc. Natl. Acad. Sci.* **99,** 11646–11651 (2002).

86. Deliolanis, N. C. *et al.* Performance of the red-shifted fluorescent proteins in deep-tissue molecular imaging applications. *J. Biomed. Opt.* **13,** 044008–044008–9 (2008).

87. Miesenböck, G., De Angelis, D. A. & Rothman, J. E. Visualizing secretion and synaptic transmission with pH-sensitive green fluorescent proteins. *Nature* **394,** 192–195 (1998).

88. Eli, P. & Chakrabartty, A. Variants of DsRed fluorescent protein: development of a copper sensor. *Protein Sci.* **15,** 2442–2447 (2006).

89. Kuner, T. & Augustine, G. J. A genetically encoded ratiometric indicator for chloride: capturing chloride transients in cultured hippocampal neurons. *Neuron* **27,** 447–459 (2000).

90. Nakai, J., Ohkura, M. & Imoto, K. A high signal-to-noise Ca^{2+} probe composed of a single green fluorescent protein. *Nat. Biotechnol.* **19,** 137–141 (2001).

91. Nagai, T., Sawano, A., Park, E. S. & Miyawaki, A. Circularly permuted green fluorescent proteins engineered to sense Ca^{2+}. *Proc. Natl. Acad. Sci.* **98,** 3197–3202 (2001).

92. Wang, Q., Shui, B., Kotlikoff, M. I. & Sondermann, H. Structural basis for calcium sensing by GCaMP2. *Structure* **16,** 1817–1827 (2008).

93. Akerboom, J. *et al.* Crystal structures of the GCaMP calcium sensor reveal the mechanism of fluorescence signal change and aid rational design. *J. Biol. Chem.* **284,** 6455–6464 (2009).

94. Alford, S. C., Wu, J., Zhao, Y., Campbell, R. E. & Knöpfel, T. Optogenetic reporters. *Biol. Cell* **105,** 14–29 (2013).

95. Kerppola, T. K. Bimolecular fluorescence complementation (BiFC) analysis as a probe of protein interactions in living cells. *Annu. Rev. Biophys.* **37,** 465–487 (2008).

96. Hu, C.-D., Chinenov, Y. & Kerppola, T. K. Visualization of interactions among bZIP and Rel family proteins in living cells using bimolecular fluorescence complementation. *Mol. Cell* **9,** 789–798 (2002).

97. Alford, S. C., Ding, Y., Simmen, T. & Campbell, R. E. Dimerization-dependent green and yellow fluorescent proteins. *ACS Synth. Biol.* **1,** 569 (2012).

98. Ding, Y. *et al.* Ratiometric biosensors based on dimerization-dependent fluorescent protein exchange. *Nat. Methods* **12,** 195–198 (2015).

99. Berridge, M. J. Neuronal calcium signaling. *Neuron* **21,** 13–26 (1998).

100. Berridge, M. J., Lipp, P. & Bootman, M. D. The versatility and universality of calcium signalling. *Nat. Rev. Mol. Cell Biol.* **1,** 11–21 (2000).

101. Clapham, D. E. Calcium signaling. *Cell* **131,** 1047–1058 (2007).

102. Grynkiewicz, G., Poenie, M. & Tsien, R. Y. A new generation of Ca^{2+} indicators with greatly improved fluorescence properties. *J. Biol. Chem.* **260,** 3440–3450 (1985).

103. Göbel, W. & Helmchen, F. In vivo calcium imaging of neural network function. *Physiology* **22,** 358–365 (2007).

104. Garaschuk, O. *et al.* Optical monitoring of brain function in vivo: from neurons to networks. *Pflügers Archiv* **453,** 385–396 (2006).

105. Miyawaki, A. *et al.* Fluorescent indicators for Ca^{2+} based on green fluorescent proteins and calmodulin. *Nature* **388,** 882–887 (1997).

106. Romoser, V. A., Hinkle, P. M. & Persechini, A. Detection in living cells of Ca^{2+}-dependent changes in the fluorescence emission of an indicator composed of two green fluorescent

protein variants linked by a calmodulin-binding sequence A new class of fluorescent indicators. *J. Biol. Chem.* **272,** 13270–13274 (1997).

107. Miyawaki, A., Griesbeck, O., Heim, R. & Tsien, R. Y. Dynamic and quantitative Ca^{2+} measurements using improved cameleons. *Proc. Natl. Acad. Sci.* **96,** 2135–2140 (1999).
108. Nagai, T., Yamada, S., Tominaga, T., Ichikawa, M. & Miyawaki, A. Expanded dynamic range of fluorescent indicators for Ca^{2+} by circularly permuted yellow fluorescent proteins. *Proc. Natl. Acad. Sci. U. S. A.* **101,** 10554–10559 (2004).
109. Horikawa, K. *et al.* Spontaneous network activity visualized by ultrasensitive Ca2+ indicators, yellow Cameleon-Nano. *Nat. Methods* **7,** 729–732 (2010).
110. Mank, M. *et al.* A genetically encoded calcium indicator for chronic *in vivo* two-photon imaging. *Nat. Methods* **5,** 805–811 (2008).
111. Thestrup, T. *et al.* Optimized ratiometric calcium sensors for functional *in vivo* imaging of neurons and T lymphocytes. *Nat. Methods* **11,** 175–182 (2014).
112. Heim, N. & Griesbeck, O. Genetically encoded indicators of cellular calcium dynamics based on troponin C and green fluorescent protein. *J. Biol. Chem.* **279,** 14280–14286 (2004).
113. Mank, M. *et al.* A FRET-based calcium biosensor with fast signal kinetics and high fluorescence change. *Biophys. J.* **90,** 1790–1796 (2006).
114. Baird, G. S., Zacharias, D. A. & Tsien, R. Y. Circular permutation and receptor insertion within green fluorescent proteins. *Proc. Natl. Acad. Sci.* **96,** 11241–11246 (1999).
115. Reiff, D. F. *et al.* In vivo performance of genetically encoded indicators of neural activity in flies. *Journal of Neuroscience* **25,** 4766–4778 (2005).
116. Díez-García, J. *et al.* Activation of cerebellar parallel fibers monitored in transgenic mice expressing a fluorescent Ca2+ indicator protein. *Eur. J. Neurosci.* **22,** 627–635 (2005).

117. Tian, L. *et al.* Imaging neural activity in worms, flies and mice with improved GCaMP calcium indicators. *Nat. Methods* **6,** 875–881 (2009).

118. Sun, X. R. *et al.* Fast GCaMPs for improved tracking of neuronal activity. *Nat. Commun.* **4,** (2013).

119. Chen, T.-W. *et al.* Ultrasensitive fluorescent proteins for imaging neuronal activity. *Nature* **499,** 295–300 (2013).

120. Zhao, Y. *et al.* An expanded palette of genetically encoded Ca^{2+} indicators. *Science* **333,** 1888–1891 (2011).

121. Wu, J. *et al.* A long Stokes shift red fluorescent Ca^{2+} indicator protein for two-photon and ratiometric imaging. *Nat. Commun.* **5,** (2014).

122. Wu, J. *et al.* Improved orange and red Ca^{2+} indicators and photophysical considerations for optogenetic applications. *ACS Chem. Neurosci.* **4,** 963–972 (2013).

123. Wu, J. *et al.* Red fluorescent genetically encoded Ca^{2+} indicators for use in mitochondria and endoplasmic reticulum. *Biochem. J* **464,** 13–22 (2014).

124. Inoue, M. *et al.* Rational design of a high-affinity, fast, red calcium indicator R-CaMP2. *Nat. Methods* **12,** 64–70 (2015).

125. Lindenburg, L. & Merkx, M. Engineering genetically encoded FRET sensors. *Sensors* **14,** 11691–11713 (2014).

126. Jiang, L. *et al.* De novo computational design of retro-aldol enzymes. *Science* **319,** 1387–1391 (2008).

127. Siegel, J. B. *et al.* Computational design of an enzyme catalyst for a stereoselective bimolecular Diels-Alder reaction. *Science* **329,** 309–313 (2010).

128. Dahiyat, B. I. & Mayo, S. L. De novo protein design: fully automated sequence selection. *Science* **278,** 82–87 (1997).

129. Reina, J. *et al.* Computer-aided design of a PDZ domain to recognize new target sequences. *Nat. Struct. Mol. Biol.* **9,** 621–627 (2002).

130. Röthlisberger, D. *et al.* Kemp elimination catalysts by computational enzyme design. *Nature* **453,** 190–195 (2008).

131. Yuan, L., Kurek, I., English, J. & Keenan, R. Laboratory-directed protein evolution. *Microbiol. Mol. Biol. Rev.* **69,** 373–392 (2005).

132. Bloom, J. D. & Arnold, F. H. In the light of directed evolution: pathways of adaptive protein evolution. *Proc. Natl. Acad. Sci.* **106,** 9995–10000 (2009).

133. García-Ruiz, E., Maté, D., Ballesteros, A., Martinez, A. T. & Alcalde, M. Evolving thermostability in mutant libraries of ligninolytic oxidoreductases expressed in yeast. *Microb. Cell Fact.* **9,** 17 (2010).

134. Yang, G. & Withers, S. G. Ultrahigh-throughput FACS-based screening for directed enzyme evolution. *Chembiochem* **10,** 2704–2715 (2009).

135. Aharoni, A. *et al.* High-throughput screening methodology for the directed evolution of glycosyltransferases. *Nat. Methods* **3,** 609–614 (2006).

136. Chen, I., Dorr, B. M. & Liu, D. R. A general strategy for the evolution of bond-forming enzymes using yeast display. *Proc. Natl. Acad. Sci.* **108,** 11399–11404 (2011).

137. Gorkin, R. *et al.* Centrifugal microfluidics for biomedical applications. *Lab Chip* **10,** 1758–1773 (2010).

138. Strohmeier, O. *et al.* Centrifugal microfluidic platforms: advanced unit operations and applications. *Chem. Soc. Rev.* **44,** 6187–6229 (2015).

139. Burtis, C. A. *et al.* Development of a miniature fast analyzer. *Clin. Chem.* **18,** 753–761 (1972).

140. Burtis, C. A. & Johnson, W. F. Device and method for automated separation of a sample of whole blood into aliquots. (1989).

141. Schembri, C. T., Burd, T. L., Kopf-Sill, A. R., Shea, L. R. & Braynin, B. Centrifugation and capillarity integrated into a multiple analyte whole blood analyser. *J. Anal. Methods Chem.* **17,** 99–104 (1995).

142. Madou, M. J. & Kellogg, G. J. *LabCD: a centrifuge-based microfluidic platform for diagnostics*. (International Society for Optics and Photonics, 1998).

143. Hoffmann, J., Mark, D., Lutz, S., Zengerle, R. & von Stetten, F. Pre-storage of liquid reagents in glass ampoules for DNA extraction on a fully integrated lab-on-a-chip cartridge. *Lab Chip* **10,** 1480–1484 (2010).

144. Mårtensson, G. *et al.* Rapid PCR amplification of DNA utilizing Coriolis effects. *Eur. Biophys. J.* **35,** 453–458 (2006).

145. Sundberg, S. O., Wittwer, C. T., Gao, C. & Gale, B. K. Spinning disk platform for microfluidic digital polymerase chain reaction. *Anal. Chem.* **82,** 1546–1550 (2010).

146. Focke, M. *et al.* Microstructuring of polymer films for sensitive genotyping by real-time PCR on a centrifugal microfluidic platform. *Lab Chip* **10,** 2519–2526 (2010).

147. Focke, M., Stumpf, F., Roth, G., Zengerle, R. & von Stetten, F. Centrifugal microfluidic system for primary amplification and secondary real-time PCR. *Lab Chip* **10,** 3210–3212 (2010).

148. Jung, J. H., Choi, S. J., Park, B. H., Choi, Y. K. & Seo, T. S. Ultrafast rotary PCR system for multiple influenza viral RNA detection. *Lab Chip* **12,** 1598–1600 (2012).

149. Lai, S. *et al.* Design of a compact disk-like microfluidic platform for enzyme-linked immunosorbent assay. *Anal. Chem.* **76,** 1832–1837 (2004).

150. Lee, B. S. *et al.* A fully automated immunoassay from whole blood on a disc. *Lab Chip* **9,** 1548–1555 (2009).

151. Grumann, M. *et al.* Sensitivity enhancement for colorimetric glucose assays on whole blood by on-chip beam-guidance. *Biomed. Microdevices* **8,** 209–214 (2006).

152. Steigert, J. *et al.* Fully integrated whole blood testing by real-time absorption measurement on a centrifugal platform. *Lab Chip* **6,** 1040–1044 (2006).

153. Li, T., Fan, Y., Cheng, Y. & Yang, J. An electrochemical Lab-on-a-CD system for parallel whole blood analysis. *Lab Chip* **13,** 2634–2640 (2013).

154. Xia, Y. & Whitesides, G. M. Soft lithography. *Annu. Rev. Mater. Sci.* **28,** 153–184 (1998).

155. Whitesides, G. M., Ostuni, E., Takayama, S., Jiang, X. & Ingber, D. E. Soft lithography in biology and biochemistry. *Annu. Rev. Biomed. Eng.* **3,** 335–373 (2001).

156. Duffy, D. C., Gillis, H. L., Lin, J., Sheppard, N. F. & Kellogg, G. J. Microfabricated centrifugal microfluidic systems: characterization and multiple enzymatic assays. *Anal. Chem.* **71,** 4669–4678 (1999).

157. Chen, X., Li, T. & Shen, J. CO2 laser ablation of microchannel on PMMA substrate for effective fabrication of microfluidic chips. *Int. Polym. Process.* **31,** 233–238 (2016).

158. Garcia-Cordero, J. L., Benito-Lopez, F., Diamond, D., Ducrée, J. & Ricco, A. J. *Low-cost microfluidic single-use valves and on-board reagent storage using laser-printer technology*. (IEEE, 2009).

159. Fiorini, G. S. & Chiu, D. T. Disposable microfluidic devices: fabrication, function, and application. *Biotechniques* **38,** 429–446 (2005).

160. Steigert, J. *et al.* Rapid prototyping of microfluidic chips in COC. *J. Micromech. Microeng.* **17,** 333 (2007).

161. Thompson, B. L. *et al.* Inexpensive, rapid prototyping of microfluidic devices using overhead transparencies and a laser print, cut and laminate fabrication method. *Nat. Protoc.* **10,** 875–886 (2015).

162. Thompson, B. L. *et al.* Microfluidic enzymatic DNA extraction on a hybrid polyester-toner-PMMA device. *Analyst* **141,** 4667–4675 (2016).

163. DuVall, J. A. *et al.* A rotationally-driven polyethylene terephthalate microdevice with integrated reagent mixing for multiplexed PCR amplification of DNA. *Anal. Methods* **8,** 7331–7340 (2016).

164. Ouyang, Y. *et al.* A disposable laser print-cut-laminate polyester microchip for multiplexed PCR via infra-red-mediated thermal control. *Anal. Chim. Acta* **901,** 59–67 (2015).

165. Ouyang, Y., Li, J., Haverstick, D. M. & Landers, J. P. Rotation-Driven Microfluidic Disc for White Blood Cell Enumeration Using Magnetic Bead Aggregation. *Anal. Chem.* **88,** 11046–11054 (2016).

166. Krauss, S. T. *et al.* Objective method for presumptive field-testing of illicit drug possession using centrifugal microdevices and smartphone analysis. *Anal. Chem.* **88,** 8689–8697 (2016).

167. Nwankire, C. E. *et al.* At-line bioprocess monitoring by immunoassay with rotationally controlled serial siphoning and integrated supercritical angle fluorescence optics. *Anal. Chim. Acta* **781,** 54–62 (2013).

168. Riegger, L. *et al.* Read-out concepts for multiplexed bead-based fluorescence immunoassays on centrifugal microfluidic platforms. *Sens. Actuators A Phys.* **126,** 455–462 (2006).

169. Strohmeier, O. *et al.* Multiplex genotyping of KRAS point mutations in tumor cell DNA by allele-specific real-time PCR on a centrifugal microfluidic disk segment. *Microchim. Acta* **181,** 1681–1688 (2014).

170. Strohmeier, O. *et al.* Real-time PCR based detection of a panel of food-borne pathogens on a centrifugal microfluidic 'LabDisk' with on-disk quality controls and standards for quantification. *Anal. Methods* **6,** 2038–2046 (2014).

171. Hoehl, M. M. *et al.* Centrifugal LabTube platform for fully automated DNA purification and LAMP amplification based on an integrated, low-cost heating system. *Biomed. Microdevices* **16,** 375–385 (2014).

172. Kim, T.-H., Park, J., Kim, C.-J. & Cho, Y.-K. Fully integrated lab-on-a-disc for nucleic acid analysis of food-borne pathogens. *Anal. Chem.* **86,** 3841–3848 (2014).

173. Thompson, B. L. *et al.* Hematocrit analysis through the use of an inexpensive centrifugal polyester-toner device with finger-to-chip blood loading capability. *Anal. Chim. Acta* **924,** 1–8 (2016).

174. Morais, S., Tortajada-Genaro, L. A., Arnandis-Chover, T., Puchades, R. & Maquieira, A. Multiplexed microimmunoassays on a digital versatile disk. *Anal. Chem.* **81,** 5646–5654 (2009).

175. Li, Y., Ou, L. M. L. & Yu, H.-Z. Digitized molecular diagnostics: reading disk-based bioassays with standard computer drives. *Anal. Chem.* **80,** 8216–8223 (2008).

176. Lange, S. A. *et al.* Measuring biomolecular binding events with a compact disc player device. *Angew. Chem. Int. Ed.* **45,** 270–273 (2006).

177. Bosco, F. G. *et al.* High throughput label-free platform for statistical bio-molecular sensing. *Lab Chip* **11,** 2411–2416 (2011).

178. Kim, T.-H. *et al.* Flow-enhanced electrochemical immunosensors on centrifugal microfluidic platforms. *Lab Chip* **13,** 3747–3754 (2013).

179. Abi-Samra, K. *et al.* Electrochemical velocimetry on centrifugal microfluidic platforms. *Lab Chip* **13,** 3253–3260 (2013).

180. Nwankire, C. E. *et al.* Label-free impedance detection of cancer cells from whole blood on an integrated centrifugal microfluidic platform. *Biosensors and Bioelectronics* **68,** 382–389 (2015).

181. Gustafsson, M., Hirschberg, D., Palmberg, C., Jörnvall, H. & Bergman, T. Integrated sample preparation and MALDI mass spectrometry on a microfluidic compact disk. *Anal. Chem.* **76,** 345–350 (2004).

182. Lafleur, J. P. & Salin, E. D. Pre-concentration of trace metals on centrifugal microfluidic discs with direct determination by laser ablation inductively coupled plasma mass spectrometry. *J. Anal. At. Spectrom.* **24,** 1511–1516 (2009).

183. Dettmer, K., Aronov, P. A. & Hammock, B. D. Mass spectrometry-based metabolomics. *Mass Spectrom. Rev.* **26,** 51–78 (2007).

184. Beckonert, O. *et al.* Metabolic profiling, metabolomic and metabonomic procedures for NMR spectroscopy of urine, plasma, serum and tissue extracts. *Nat. Protoc.* **2,** 2692–2703 (2007).

185. Zhou, Y., Peng, C., Harris, K. D., Mandal, R. & Harrison, D. J. Salt Segregation and Sample Cleanup on Perfluoro-Coated Nanostructured Surfaces for Laser Desorption Ionization Mass Spectrometry of Biofluid Samples. *Anal. Chem.* **89,** 3362–3369 (2017).

186. El-Aneed, A., Cohen, A. & Banoub, J. Mass spectrometry, review of the basics: electrospray, MALDI, and commonly used mass analyzers. *Appl. Spectrosc. Rev.* **44,** 210–230 (2009).

187. Herbert, C. G. & Johnstone, R. A. W. *Mass spectrometry basics*. (CRC press, 2002).

188. Tanaka, K. *et al.* Protein and polymer analyses up to m/z 100 000 by laser ionization time-of-flight mass spectrometry. *Rapid Commun. Mass Spectrom.* **2,** 151–153 (1988).

189. Karas, M. & Hillenkamp, F. Laser desorption ionization of proteins with molecular masses exceeding 10000 daltons. *Anal. Chem.* **60,** 2299–2301 (1988).

190. Yamashita, M. & Fenn, J. B. Electrospray ion source: another variation on the free-jet theme. *J. Phys. Chem.* **88,** (1984).

191. Yamashita, M. & Fenn, J. B. Negative ion production with the electrospray ion source. *J. Phys. Chem.* **88,** (1984).

192. Albrethsen, J. The first decade of MALDI protein profiling: a lesson in translational biomarker research. *J. Proteomics* **74,** 765–773 (2011).

193. Balazy, M. Eicosanomics: targeted lipidomics of eicosanoids in biological systems. *Prostaglandins Other Lipid Mediat.* **73,** 173–180 (2004).

194. Schiller, J. *et al.* Matrix-assisted laser desorption and ionization time-of-flight (MALDI-TOF) mass spectrometry in lipid and phospholipid research. *Prog. Lipid Res.* **43,** 449–488 (2004).

195. Fuchs, B., Süß, R. & Schiller, J. An update of MALDI-TOF mass spectrometry in lipid research. *Prog. Lipid Res.* **49,** 450–475 (2010).

196. Gut, I. G. DNA analysis by MALDI-TOF mass spectrometry. *Hum. Mutat.* **23,** 437–441 (2004).

197. Kirpekar, F. *et al.* DNA sequence analysis by MALDI mass spectrometry. *Nucleic Acids Res.* **26,** 2554–2559 (1998).

198. Lecchi, P. & Pannell, L. K. The detection of intact double-stranded DNA by MALDI. *J. Am. Soc. Mass Spectrom.* **6,** 972–975 (1995).

199. Peterson, D. S. Matrix-free methods for laser desorption/ionization mass spectrometry. *Mass Spectrom. Rev.* **26,** 19–34 (2007).

200. Banoub, J. H., Newton, R. P., Esmans, E., Ewing, D. F. & Mackenzie, G. Recent developments in mass spectrometry for the characterization of nucleosides, nucleotides, oligonucleotides, and nucleic acids. *Chem. Rev.* **105,** 1869–1916 (2005).

201. Wei, J., Buriak, J. M. & Siuzdak, G. Desorption–ionization mass spectrometry on porous silicon. *Nature* **399,** 243–246 (1999).

202. Northen, T. R. *et al.* Clathrate nanostructures for mass spectrometry. *Nature* **449,** 1033–1036 (2007).

203. Patti, G. J. *et al.* Detection of carbohydrates and steroids by cation-enhanced nanostructure-initiator mass spectrometry (NIMS) for biofluid analysis and tissue imaging. *Anal. Chem.* **82,** 121 (2010).

204. Greving, M. *et al.* Acoustic deposition with NIMS as a high-throughput enzyme activity assay. *Anal. Bioanal. Chem.* **403,** 707–711 (2012).

205. Northen, T. R. *et al.* A nanostructure-initiator mass spectrometry-based enzyme activity assay. *Proc. Natl. Acad. Sci.* **105,** 3678–3683 (2008).

206. Yanes, O. *et al.* Nanostructure initiator mass spectrometry: tissue imaging and direct biofluid analysis. *Anal. Chem.* **81,** 2969 (2009).

207. Greving, M. P., Patti, G. J. & Siuzdak, G. Nanostructure-initiator mass spectrometry metabolite analysis and imaging. *Anal. Chem.* **83,** 2 (2011).

208. Patti, G. J. *et al.* Nanostructure-initiator mass spectrometry (NIMS) imaging of brain cholesterol metabolites in Smith-Lemli-Opitz syndrome. *Neuroscience* **170,** 858–864 (2010).

209. Ramizy, A., Aziz, W. J., Hassan, Z., Omar, K. & Ibrahim, K. The effect of porosity on the properties of silicon solar cell. *Microelectronics International* **27,** 117–120 (2010).

210. Law, K. P. & Larkin, J. R. Recent advances in SALDI-MS techniques and their chemical and bioanalytical applications. *Anal. Bioanal. Chem.* **399,** 2597–2622 (2011).

211. Ronkel, F. & Schultze, J. W. Electrochemical aspects of porous silicon formation. *J. Porous Mater.* **7,** 11–16 (2000).

212. Robbie, K. & Brett, M. J. Sculptured thin films and glancing angle deposition: Growth mechanics and applications. *J. Vac. Sci. Technol. A* **15,** 1460–1465 (1997).

213. Gish, D. A., Summers, M. A., Jensen, M. O. & Brett, M. J. *Enhanced Control of Morphology in Thin Film Nanostructure Arrays*. (IEEE, 2006).

214. Hawkeye, M. M. & Brett, M. J. Glancing angle deposition: fabrication, properties, and applications of micro-and nanostructured thin films. *J. Vac. Sci. Technol. A* **25,** 1317–1335 (2007).

215. Krause, K. M., Taschuk, M. T. & Brett, M. J. Glancing angle deposition on a roll: towards high-throughput nanostructured thin films. *J. Vac. Sci. Technol. A* **31,** 031507 (2013).

216. Taschuk, M. T., Harris, K. D., Smetaniuk, D. P. & Brett, M. J. Decoupling sensor morphology and material: Atomic layer deposition onto nanocolumn scaffolds. *Sens. Actuators B Chem.* **162,** 1–6 (2012).

217. Jensen, M. O. & Brett, M. J. Periodically structured glancing angle deposition thin films. *IEEE Trans. Nanotechnol.* **4,** 269–277 (2005).

218. Schubert, E., Höche, T., Frost, F. & Rauschenbach, B. Nanostructure fabrication by glancing angle ion beam assisted deposition of silicon. *Appl. Phys. A: Mater. Sci. Process.* **81,** 481–486 (2005).

219. Kennedy, S. R., Brett, M. J., Miguez, H., Toader, O. & John, S. Optical properties of a three-dimensional silicon square spiral photonic crystal. *Photonics and Nanostructures-Fundamentals and Applications* **1,** 37–42 (2003).

220. Chu, H., Liu, Y., Huang, Y. & Zhao, Y. A high sensitive fiber SERS probe based on silver nanorod arrays. *Opt. Express* **15,** 12230–12239 (2007).

221. Gish, D. A., Nsiah, F., McDermott, M. T. & Brett, M. J. Localized surface plasmon resonance biosensor using silver nanostructures fabricated by glancing angle deposition. *Anal. Chem.* **79,** 4228–4232 (2007).

222. Liu, F., Yu, C., Shen, L., Barnard, J. & Mankey, G. J. The magnetic properties of cobalt films produced by glancing angle deposition. *IEEE Trans. Magn.* **36,** 2939–2941 (2000).

223. Steele, J. J., Taschuk, M. T. & Brett, M. J. Nanostructured metal oxide thin films for humidity sensors. *IEEE Sens. J.* **8,** 1422–1429 (2008).

224. Zhang, W., Ganesh, N., Block, I. D. & Cunningham, B. T. High sensitivity photonic crystal biosensor incorporating nanorod structures for enhanced surface area. *Sens. Actuators B Chem.* **131,** 279–284 (2008).

225. Rider, D. A. *et al.* Indium tin oxide nanopillar electrodes in polymer/fullerene solar cells. *Nanotechnology* **22,** 085706 (2011).

226. Jemere, A. B., Bezuidenhout, L. W., Brett, M. J. & Harrison, D. J. Matrix-free laser desorption/ionization mass spectrometry using silicon glancing angle deposition (GLAD) films. *Rapid Commun. Mass Spectrom.* **24,** 2305–2311 (2010).

227. Broughton, J. N. & Brett, M. J. Electrochemical capacitance in manganese thin films with chevron microstructure. *Electrochem. Solid State Letters* **5,** A279–A282 (2002).

228. Harris, K. D., McBride, J. R., Nietering, K. E. & Brett, M. J. Fabrication of porous platinum thin films for hydrocarbon sensor applications. *Sens. Mater.* **13,** 225–234 (2001).

229. Suzuki, M., Ito, T. & Taga, Y. Photocatalysis of sculptured thin films of TiO_2. *Appl. Phys. Lett.* **78,** 3968–3970 (2001).

230. Steele, J. J., van Popta, A. C., Hawkeye, M. M., Sit, J. C. & Brett, M. J. Nanostructured gradient index optical filter for high-speed humidity sensing. *Sens. Actuators B Chem.* **120,** 213–219 (2006).

231. Jim, S. R. *et al.* Engineered anisotropic microstructures for ultrathin-layer chromatography. *Anal. Chem.* **82,** 5349–5356 (2010).

232. Jim, S. R., Oko, A. J., Taschuk, M. T. & Brett, M. J. Morphological modification of nanostructured ultrathin-layer chromatography stationary phases. *J. Chromatogr. A* **1218,** 7203–7210 (2011).

233. Kirchert, S. *et al.* Inkjet application, chromatography, and mass spectrometry of sugars on nanostructured thin films. *Anal. Bioanal. Chem.* **405,** 7195–7203 (2013).

234. Wannenmacher, J., Jim, S. R., Taschuk, M. T., Brett, M. J. & Morlock, G. E. Ultrathin-layer chromatography on SiO_2, Al_2O_3, TiO_2, and ZrO_2 nanostructured thin films. *J. Chromatogr. A* **1318,** 234–243 (2013).

235. Oko, A. J., Jim, S. R., Taschuk, M. T. & Brett, M. J. Analyte migration in anisotropic nanostructured ultrathin-layer chromatography media. *J. Chromatogr. A* **1218,** 2661–2667 (2011).

236. Bezuidenhout, L. W., Nazemifard, N., Jemere, A. B., Harrison, D. J. & Brett, M. J. Microchannels filled with diverse micro-and nanostructures fabricated by glancing angle deposition. *Lab Chip* **11,** 1671–1678 (2011).

237. Packer, M. S. & Liu, D. R. Methods for the directed evolution of proteins. *Nat. Rev. Genet.* **16,** 379–394 (2015).

238. Yin, H. & Marshall, D. Microfluidics for single cell analysis. *Curr. Opin. Biotechnol.* **23,** 110–119 (2012).

239. Lecault, V., White, A. K., Singhal, A. & Hansen, C. L. Microfluidic single cell analysis: from promise to practice. *Curr. Opin. Chem. Biol.* **16,** 381–390 (2012).

240. Wheeler, A. R. *et al.* Microfluidic device for single-cell analysis. *Anal. Chem.* **75,** 3581–3586 (2003).

241. Chen, C. H., Cho, S. H., Tsai, F., Erten, A. & Lo, Y.-H. Microfluidic cell sorter with integrated piezoelectric actuator. *Biomed. Microdevices* **11,** 1223–1231 (2009).

242. Hoi, H. *et al.* An Engineered Monomeric Zoanthus sp. Yellow Fluorescent Protein. *Chem. Biol.* **20,** 1296–1304 (2013).

243. Dana, H. *et al.* Sensitive red protein calcium indicators for imaging neural activity. *Elife* **5,** (2016).

244. Behnia, R., Clark, D. A., Carter, A. G., Clandinin, T. R. & Desplan, C. Processing properties of ON and OFF pathways for Drosophila motion detection. *Nature* **512,** 427–430 (2014).

245. Strother, J. A., Nern, A. & Reiser, M. B. Direct observation of ON and OFF pathways in the Drosophila visual system. *Curr. Biol.* **24,** 976–983 (2014).

246. Yang, H. H. *et al.* Subcellular Imaging of Voltage and Calcium Signals Reveals Neural Processing In\udotVivo. *Cell* **166,** 245–257 (2016).

247. Klapoetke, N. C. *et al.* Independent optical excitation of distinct neural populations. *Nat. Methods* **11,** 338–346 (2014).

248. Pologruto, T. A., Sabatini, B. L. & Svoboda, K. ScanImage: flexible software for operating laser scanning microscopes. *Biomed. Eng. Online* **2,** 13 (2003).

249. Schlotterbeck, G., Ross, A., Dieterle, F. & Senn, H. Metabolic profiling technologies for biomarker discovery in biomedicine and drug development. *Pharmacogenomics* **7,** 1055–1075 (2006).

250. Wang, X. *et al.* Urine metabolomics analysis for biomarker discovery and detection of jaundice syndrome in patients with liver disease. *Mol. Cell. Proteomics* **11,** 370–380 (2012).

251. Kim, K. *et al.* Urine metabolomics analysis for kidney cancer detection and biomarker discovery. *Mol. Cell. Proteomics* **8,** 558–570 (2009).

252. Griffiths, W. J. *et al.* Targeted metabolomics for biomarker discovery. *Angew. Chem. Int. Ed Engl.* **49,** 5426–5445 (2010).

253. Emwas, A.-H. M., Salek, R. M., Griffin, J. L. & Merzaban, J. NMR-based metabolomics in human disease diagnosis: applications, limitations, and recommendations. *Metabolomics* **9,** 1048–1072 (2013).

254. Mickiewicz, B., Vogel, H. J., Wong, H. R. & Winston, B. W. Metabolomics as a novel approach for early diagnosis of pediatric septic shock and its mortality. *Am. J. Respir. Crit. Care Med.* **187,** 967–976 (2013).

255. Tiziani, S., Lopes, V. & Günther, U. L. Early Stage Diagnosis of Oral Cancer Using ^{1}H NMR–Based Metabolomics. *Neoplasia* **11,** 269–IN10 (2009).

256. Wen, H. *et al.* A new NMR-based metabolomics approach for the diagnosis of biliary tract cancer. *J. Hepatol.* **52,** 228–233 (2010).

257. Miyagi, Y. *et al.* Plasma free amino acid profiling of five types of cancer patients and its application for early detection. *PLoS One* **6,** e24143 (2011).

258. Dong, H. *et al.* Ingenuity pathways analysis of urine metabolomics phenotypes toxicity of Chuanwu in Wistar rats by UPLC-Q-TOF-HDMS coupled with pattern recognition methods. *Mol. Biosyst.* **8,** 1206–1221 (2012).

259. Jones, O. A. H., Spurgeon, D. J., Svendsen, C. & Griffin, J. L. A metabolomics based approach to assessing the toxicity of the polyaromatic hydrocarbon pyrene to the earthworm Lumbricus rubellus. *Chemosphere* **71,** 601–609 (2008).

260. Wang, X. *et al.* Metabolomics study on the toxicity of aconite root and its processed products using ultraperformance liquid-chromatography/electrospray-ionization synapt high-definition mass spectrometry coupled with pattern recognition approach and ingenuity pathways analysis. *J. Proteome Res.* **11,** 1284–1301 (2011).

261. Roessner, U. *et al.* An investigation of boron toxicity in barley using metabolomics. *Plant Physiol.* **142,** 1087–1101 (2006).

262. West, P. R., Weir, A. M., Smith, A. M., Donley, E. L. R. & Cezar, G. G. Predicting human developmental toxicity of pharmaceuticals using human embryonic stem cells and metabolomics. *Toxicol. Appl. Pharmacol.* **247,** 18–27 (2010).

263. Lindsay, K. L. *et al.* Longitudinal Metabolomic Profiling of Amino Acids and Lipids across Healthy Pregnancy. *PLoS One* **10,** e0145794 (2015).

264. Mihalik, S. J. *et al.* Metabolomic profiling of fatty acid and amino acid metabolism in youth with obesity and type 2 diabetes: evidence for enhanced mitochondrial oxidation. *Diabetes Care* **35,** 605–611 (2012).

265. Michaliszyn, S. F. *et al.* Metabolomic profiling of amino acids and β-cell function relative to insulin sensitivity in youth. *J. Clin. Endocrinol. Metab.* **97,** E2119–24 (2012).

266. Oliveira, A. R., Silva, I., LoTurco, E., Martins, H. & Chauffaille, M. L. Initial Analysis of Lipid Metabolomic Profile Reveals Differential Expression Features in Myeloid Malignancies. *Blood* **124,** 5958–5958 (2014).

267. Cai, X. & Li, R. Concurrent profiling of polar metabolites and lipids in human plasma using HILIC-FTMS. *Sci. Rep.* **6,** 36490 (2016).

268. Paapstel, K. *et al.* Metabolomic profiles of lipid metabolism, arterial stiffness and hemodynamics in male coronary artery disease patients. *IJC Metabolic & Endocrine* **11,** 13–18 (2016).

269. Sampey, B. P. *et al.* Metabolomic profiling reveals mitochondrial-derived lipid biomarkers that drive obesity-associated inflammation. *PLoS One* **7,** e38812 (2012).

270. Yi, L.-Z., He, J., Liang, Y.-Z., Yuan, D.-L. & Chau, F.-T. Plasma fatty acid metabolic profiling and biomarkers of type 2 diabetes mellitus based on GC/MS and PLS-LDA. *FEBS Lett.* **580,** 6837–6845 (2006).

271. Lam, C.-W. & Law, C.-Y. Untargeted mass spectrometry-based metabolomic profiling of pleural effusions: fatty acids as novel cancer biomarkers for malignant pleural effusions. *J. Proteome Res.* **13,** 4040–4046 (2014).

272. Zhang, A., Sun, H. & Wang, X. Serum metabolomics as a novel diagnostic approach for disease: a systematic review. *Anal. Bioanal. Chem.* **404,** 1239–1245 (2012).

273. Bruce, S. J. *et al.* Evaluation of a protocol for metabolic profiling studies on human blood plasma by combined ultra-performance liquid chromatography/mass spectrometry: From extraction to data analysis. *Anal. Biochem.* **372,** 237–249 (2008).

274. Michopoulos, F., Lai, L., Gika, H., Theodoridis, G. & Wilson, I. UPLC-MS-based analysis of human plasma for metabonomics using solvent precipitation or solid phase extraction. *J. Proteome Res.* **8,** 2114–2121 (2009).

275. Zelena, E. *et al.* Development of a robust and repeatable UPLC- MS method for the long-term metabolomic study of human serum. *Anal. Chem.* **81,** 1357–1364 (2009).

276. Pereira, H., Martin, J.-F., Joly, C., Sébédio, J.-L. & Pujos-Guillot, E. Development and validation of a UPLC/MS method for a nutritional metabolomic study of human plasma. *Metabolomics* **6,** 207–218 (2010).

277. Psychogios, N. *et al.* The human serum metabolome. *PLoS One* **6,** e16957 (2011).

278. Mercier, P., Lewis, M. J., Chang, D., Baker, D. & Wishart, D. S. Towards automatic metabolomic profiling of high-resolution one-dimensional proton NMR spectra. *J. Biomol. NMR* **49,** 307–323 (2011).

279. Luk, V. N. & Wheeler, A. R. A digital microfluidic approach to proteomic sample processing. *Anal. Chem.* **81,** 4524–4530 (2009).

280. Moon, H., Wheeler, A. R., Garrell, R. L., Loo, J. A. & Kim, C.-J. C. An integrated digital microfluidic chip for multiplexed proteomic sample preparation and analysis by MALDI-MS. *Lab Chip* **6,** 1213–1219 (2006).

281. Wheeler, A. R. *et al.* Digital microfluidics with in-line sample purification for proteomics analyses with MALDI-MS. *Anal. Chem.* **77,** 534–540 (2005).

282. Jebrail, M. J. & Wheeler, A. R. Digital microfluidic method for protein extraction by precipitation. *Anal. Chem.* **81,** 330–335 (2009).

283. Luk, V. N., Fiddes, L. K., Luk, V. M., Kumacheva, E. & Wheeler, A. R. Digital microfluidic hydrogel microreactors for proteomics. *Proteomics* **12,** 1310–1318 (2012).

284. Jebrail, M. J. *et al.* A digital microfluidic method for dried blood spot analysis. *Lab Chip* **11,** 3218–3224 (2011).

285. Abdelgawad, M., Watson, M. W. L. & Wheeler, A. R. Hybrid microfluidics: a digital-to-channel interface for in-line sample processing and chemical separations. *Lab Chip* **9,** 1046–1051 (2009).

286. Nagana Gowda, G. A. & Raftery, D. Quantitating metabolites in protein precipitated serum using NMR spectroscopy. *Anal. Chem.* **86,** 5433–5440 (2014).

287. Bruce, S. J. *et al.* Investigation of human blood plasma sample preparation for performing metabolomics using ultrahigh performance liquid chromatography/mass spectrometry. *Anal. Chem.* **81,** 3285–3296 (2009).

288. Crowe, K. M. Optimizing protein precipitation efficiency for assessing the contribution of low molecular weight compounds to serum antioxidant capacity. *Clin. Biochem.* **47,** 116–118 (2014).

289. Hata, K. *et al.* Evaluation of silica nanoparticle binding to major human blood proteins. *Nanoscale Res. Lett.* **9,** 2493 (2014).

290. Zhang, B., Xie, M., Bruschweiler-Li, L. & Brüschweiler, R. Nanoparticle-Assisted Removal of Protein in Human Serum for Metabolomics Studies. *Anal. Chem.* **88,** 1003–1007 (2016).

291. Lynch, I. & Dawson, K. A. Protein-nanoparticle interactions. *Nano Today* **3,** 40–47 (2008).

292. Treuel, L. & Nienhaus, G. U. Toward a molecular understanding of nanoparticle-protein interactions. *Biophys. Rev.* **4,** 137–147 (2012).

293. Zhang, B., Xie, M., Bruschweiler-Li, L., Bingol, K. & Brüschweiler, R. Use of Charged Nanoparticles in NMR-Based Metabolomics for Spectral Simplification and Improved Metabolite Identification. *Anal. Chem.* **87,** 7211–7217 (2015).

294. Chen, Y. *et al.* Standing surface acoustic wave (SSAW)-based microfluidic cytometer. *Lab Chip* **14,** 916–923 (2014).